Computational design of usual Magnetic Tunnel Junctions

Gokaran Nath Shukla

A thesis submitted for the degree of

Doctor of Philosophy

School of Physics

Trinity College Dublin

January 18, 2018

Declaration

I, Gokaran Nath Shukla, hereby declare that this thesis has not been submitted as an exercise for a degree at this or any other University. It comprises work performed entirely by myself during the course of my Ph.D. studies at Trinity College Dublin. I was involved in a number of collaborations, and where it is appropriate my collaborators are acknowledged for their contributions. I agree that the Library may lend or copy this thesis upon request.

Gokaran Nath Shukla

Abstract

Controlling the properties of materials is one of the great quests for scientists and engineers. In the past few decades more research has been devoted to control the electronic properties of materials. It has now becomes almost impossible to imagine a life without consumer electronics, which are based on the electronic properties of materials. At the same time scientists and engineers have been searching for new materials with properties that can be controlled and manipulated in order to obtain higher performances from these devices. Spintronics is one such area where we aim to control and manipulate the spin of electrons. One way to achieve this goal is, for instant, through the tunnelling magneto-resistance (TMR) effect, where one tries to control the resistance of a magnetic tunnel junction (MTJ) by changing the direction of the magnetic moment of the electrodes. When we change the direction of the magnetic moment of one electrode to make it parallel to that of the other electrode the device displays a large conductance compared to the case where the magnetization vectors of the electrodes are anti-parallel to each other. So, when the conductance is large the device is in its "0" state and when it is small then it is in the "1" state. In this way binary data can be stored in the resistance state of TMR based MTJs devices.

In this work we have investigated HfO_2, SiO_2, ZnO, AlN, and GaN semiconductors as future potential tunnel barriers for magnetic tunnel junctions. We have used the density functional theory (DFT) formalism to compute the ground state electronic properties of these materials. Since the local density approximation (LDA) functional underestimates

the band-gap of the semiconductor we have used the LDA self-interaction correction functional (LDA+ASIC) to correct the band-gap of these materials. Tunnelling magnetoresistance does not only depend upon the insulating barrier height and thickness of the barrier but also upon the symmetry and curvature of the Bloch wave-function. We have used the complex-band analysis and $k_x - k_y$ wave-function decay plots to visualize the contribution of each k state to the tunnel current. After analysis we have concluded that HfO_2 filters Bloch state with Δ_1 symmetry, whereas SiO_2 filters the $\Delta_2^{'}$ symmetry at the Γ-point. ZnO filters the Δ_1 symmetry at the Γ-point. In contrast AlN and GaN have contribution from the Γ, K and M-points to the tunnelling current. In the case of HfO_2, we have used *bcc* iron as the ferromagnetic electrode as this is able to supply Bloch state with a Δ_1 symmetry in the transport direction. In the case of SiO_2 we have used *hcp* cobalt as the ferromagnetic electrode since it is easier to design a MTJs. In ZnO, GaN, and AlN we have used both *bcc* iron and *bcc* cobalt as the ferromagnetic electrode since with a [111] face they supply a Δ_1 symmetry of the Bloch state at the Γ-point, and a Δ_2 symmetry of the Bloch state at the K and M-points when transport is in [001] direction. It may be possible that these semiconductor material may not be able to replace the currently used tunnelling barrier of MgO or Al_2O_3 for read-head applications but these semiconductors could be used as a source for spin-polarized light and can be used in optoelectronic applications using spin. This analysis may open the gateway to direct spin injection in semiconductors and to obtain spin-polarized light for the display industry.

Acknowledgements

During my post-graduate study, I have received various support and encouragement from many people. Without their help and support this thesis would not have been possible.

First of all, I would like to express my gratitude to my supervisor Prof. Stefano Sanvito for giving me the opportunity to work with his prestigious quantum-transport group. I have greatly benefited from him throughout my Ph.D. tenure.

I would like to give special thanks to Dr. Thomas Archer who co-guided this Ph.D. work. Besides, I would like to thank to all my group members (including past and present): Thomas Archer, Maria Tsoneva, Emmanuele Bosoni, Mario Zic, Matthew Ellis, Mario Galante, James Nelson, Carlo Motta, Rajarshi Tiwari, Radu Isai, Anais Colibaba, Yanhui Zhang, Ashwinee Kumar, Glenn Moynihan, Gabriele Slach, Nuala Caffrey, Urvesh Patil, Filliberto Biolcatti Rinaldi, Subhayan Roychoudhary, Clotilde Cucinotta, Ivan Rungger, Sandip Bhattacharya, Akinlolu Akande, Nadjib Baadji, Kapildeb Douli, Aaron Hurley, Durga Sankar Kesanakurthi, Thomas Cathcart, Linda Angela Zotti, Jacopo Simoni, Sri Chaitanya Das Pemmaraju, Melin Bai, Awadhesh Narayan, Anna Pertsova, Andrea Droghetti, Mauro Mantega, Amaury Souza, Rui Dong, Igor Popov. Thank you all for all your kind support and helps.

I am thankful to my examiner Prof. Charles Patterson and Prof. David O'Regan for their time and fruitful discussion during viva exam in March 2014.

I would like to special thank to Stefania who is taking all care of administrative and financial issues. You are very helpful and supportive. Thank you very much.

I would like to thank to Trinity centre for high performance computing (TCHPC) and

Irish centre for high end computing (ICHEC) and its administration for providing computational facility and resolving computer related issues.

I am grateful to the Science Foundation of Ireland (SFI) for their financial support during my Ph.D. which made this work possible.

Finally, I would like to deeply thank to my parents and past-present family members. My mother is always supportive to my decision. This work is dedicated to her.

Contents

List of Figures

List of Tables

Chapter 1

Introduction

1.1 Introduction

TMR stands for tunneling-magneto-resistance, and it is a new field in the spintronics arena. In 1988 Albert Fert [6] and Peter Grunberg [7] independently discovered the giant magneto-resistance (GMR) effect. The first GMR device was made from a Fe/Cr/Fe stack and it was structured in the current in plane (CIP) geometry. The working principle of GMR is such that when the magnetic moments of the ferromagnet are parallel to each other and a current is passed through the device, then the measured electrical resistance is smaller in comparison to the case when the magnetic moments are anti-parallel. In the parallel configuration the resistance is defined as R_P, whereas in the anti-parallel configuration it is defined as R_{AP}. The difference between the two resistances ($R_{AP} - R_P$) divided by R_P, provides a measure of the magnitude of the GMR effect. Mathematically, the GMR ratio is written as $\left(\frac{R_{AP}-R_P}{R_P}\right) \times 100$. When the current is passed parallel to the layers along the lateral direction this geometry is known as current in plane, or CIP. The change in resistance between the parallel and anti-parallel magnetic-moment configurations has been explained in terms of the scattering of the electrons spin with the local magnetic moments at the interfaces. In particular, the scattering mechanism leading to GMR can be explained with the two-fluid model due to Mott [8]. In this model the electrons current is assumed to be carried in parallel by the electrons with the two possible spin orientations. In the parallel configuration the current is mostly passed in the Cr layer, then the spin channel whose positive spin current direction is parallel (if spin orientation is down, then magnetic moment generated after spin rotation about z-axis will be up, because electron has negative charge and when it rotates clockwise about it axis (say z-direction), then the current flow in anticlockwise and thus magnetic moments generated in the positive z-direction) to the magnetic moment of the ferromagnet layer undergoes minimum scattering (see in Figure 1.1). In contrast the other spin channel faces higher scattering from both ferromagnet layers (see in Figure 1.2). In this scenario, the up spin in the parallel configuration behaves like a short circuit and has low resistance during the transport process. In the anti-parallel configuration both-spin channel get strongly scatter from both magnetic layers and thus they face the highest resistance. GMR has drawn the attention of scientists and engineers quickly and the interest has grown at a fast pace. The reason for the fast growth of this technology can be attributed to many aspects but one reason that attracts most attention is the simple device geometry. It requires only two ferromagnetic metals and one non-magnetic metal layer sandwiched between them. The fabrication of this device is not a multi-step process (multi step lithographic process). The second reason is related to the ability to measure the current-voltage characteristics. Current-voltage characteristics measurement for this geometry is easy because the current is in-plane and flows along the lateral direction. This means that the device resistance is that of a metallic thin film which is usually easy to measure. As the lateral dimensions approach the meso-scopic scale the typical device-resistance can be controlled and the noise can be kept low.

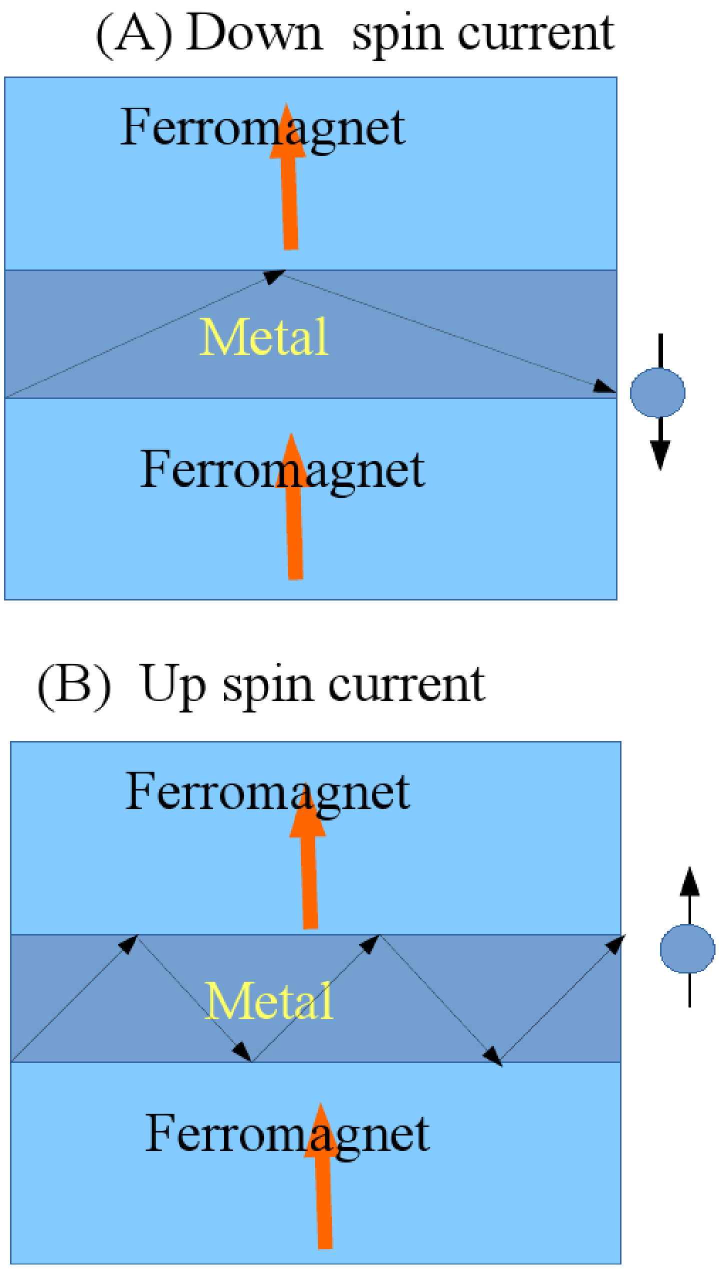

Figure 1.1: (A) Current in-plane (CIP) giant magneto-resistance (GMR) device structure with magnetic moments in both ferromagnets are parallel to each other. The current mostly passes is in the metal (Cr) layer. The down spin (up magnetic moment) electrons face a smaller number of scattering events from the ferromagnet magnetic moments during the transport. (B) CIP-GMR with ferromagnetic magnetic moments aligned parallel to each other. The up spin (down magnetic moment) electrons face a higher number of scatterings events from the ferromagnetic moments during the transport.

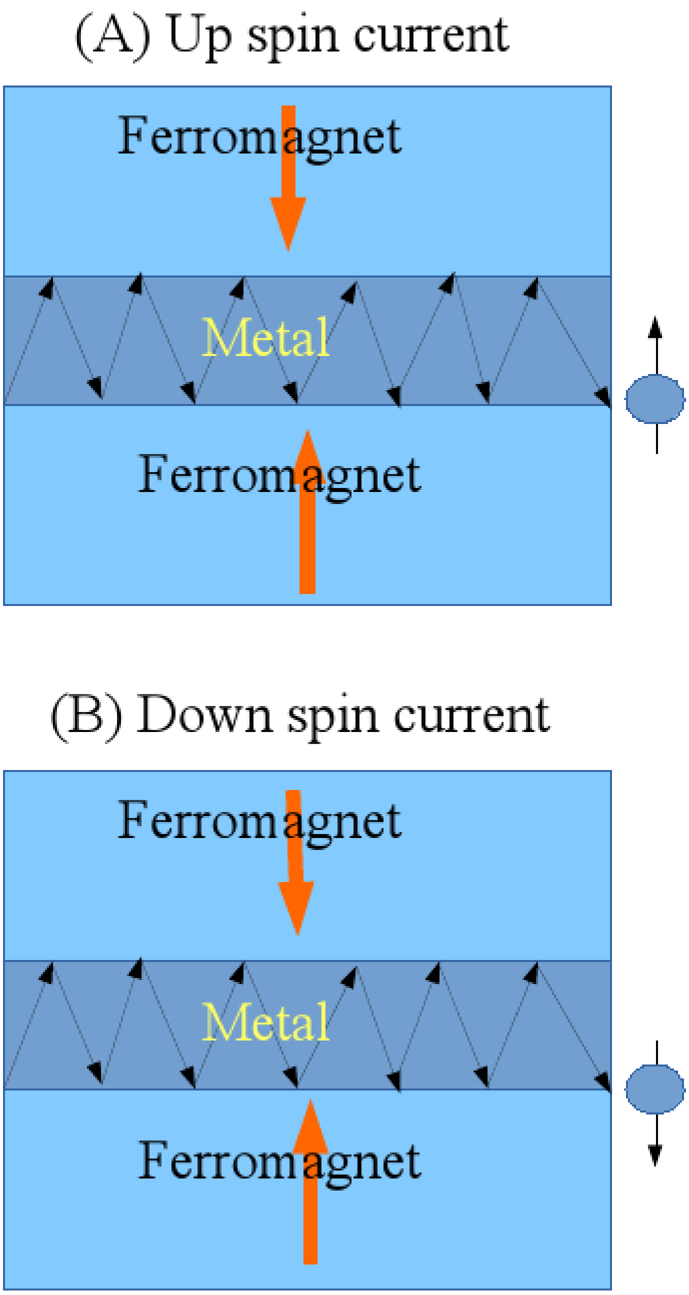

Figure 1.2: (A) Current in plane (CIP) giant magneto-resistance (GMR) device structure with ferromagnetic magnetic moments being aligned anti-parallel to each other. The current mostly passes in the metal (generally Cr) layer. The up spin (down magnetic moment) electrons face a high number of scattering events from the ferromagnet magnetic moments during the transport. (B) CIP-GMR with both the ferromagnet magnetic moments aligned anti-parallel to each other. The down spin (up magnetic moment) electron also face a large number of scattering events identical to the up spin (down magnetic moment) electrons [shown in part (A)].

1.2 CPP GMR

After the implementation of CIP GMR scientists also tried to pass the current perpendicular to layer planes (CPP geometry). The experiments did not succeed at first because the CPP GMR resistance of thin films is difficult to measure in situations where the thickness of the film is in the nanometer range and the cross section area is micrometer square. In order to measure CPP GMR the thickness of the non-ferromagnetic metal layer should be less than the spin diffusion length. Generally the spin diffusion length in magnetic metals is between $1 - 20$nm nano-meters [9]. For this reason, the first CPP GMR experiments were performed using superconducting leads [10]. After that, various efforts have been made to measure CPP GMR at room temperature with more conventional laboratory equipment. Although this has been done successfully, there are still greater challenges to quantify the resistance in the parallel and anti-parallel configurations due to the small thickness (nm) and large cross-section areas (micrometer square). Therefore, in the CPP GMR case the signal to noise ratio is not as high as in the case of CIP GMR. The working principle of the CPP GMR devices is very much the same as in CIP except that the current now is passed in the direction perpendicular to the device interfaces. A schematic diagram of a CPP GMR device is shown in figure 1.3. When the magnetic moments of both ferromagnets are parallel to each other and the current is passed perpendicular to the interfaces, the device resistance is small. In contrast, when the ferromagnetic moments are anti-parallel to each other the resistance is high. In the parallel magnetic moments configuration one spin species (say the spin down electrons) faces almost no scattering events (short circuit), whereas the other faces multiple scatterings events in both ferromagnetic electrodes [see in Figure 1.3 (A)]. In the anti-parallel configuration both spin electrons face multiple scattering in both electrodes, thus the over-all device resistance is higher than that of the parallel configuration [see in Figure 1.3 (B)]. The spin diffusion length in the parallel configuration is thus larger than that in the anti-parallel for one of the two spin channels. It is then assumed that the currents in the parallel configuration are mostly spin ballistic. Whereas in the case of the anti-parallel configuration they are mostly spin diffusive due to multiple scattering of both the spin up and spin down electrons. The transport in a meso-scopic system can be broadly classified within 3 categories, (1) diffusive transport, (2) intermediate transport, and (3) ballistic transport. In the diffusive transport regime the total energy of the electrons is not conserved. The electrons collide with scattering centres and lose their momentum, spin orientation and energy. After that the electrons accelerate again in the electric field and gain momentum and kinetic energy. Then they collide again with some other scattering centres. This process repeats multiple times during the transport [see in Figure 1.4 (A)]. In spintronics this generally happens when the spin diffusion length of the electrons is smaller than the thickness of the devices. In this case the over-all spin polarization of the current is zero. In the intermediate transport regime the electrons collide with a fewer number of scattering centres [see in Figure 1.4 (B)]. The number of collisions is much smaller than in the case of the diffusive transport. This process happens when the spin diffusion length of the electron is comparable to the thickness of the device. In the ballistic transport regime the electrons do not collide with any scattering centres [see in Figure 1.4 (C)]. This transport regime is fully elastic and in spintronics it only happens when the spin diffusion length of the electrons is greater than the thickness of the device. Generally the spin diffusion length is greater than the electron mean free path [9].

(A) Parallel configuration

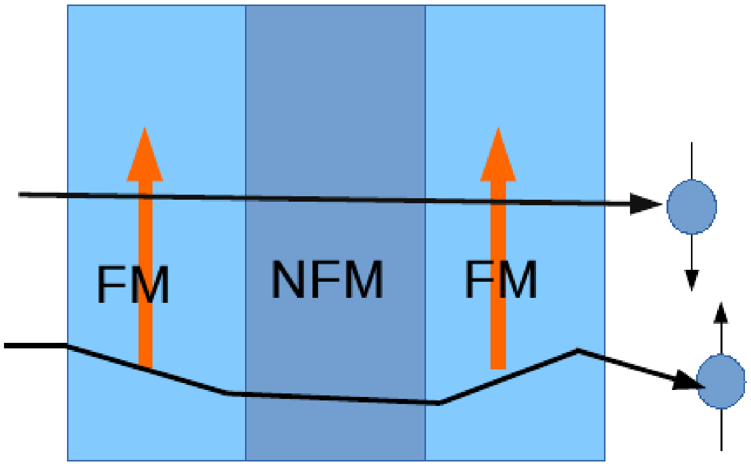

(B) Anti-parallel configuration

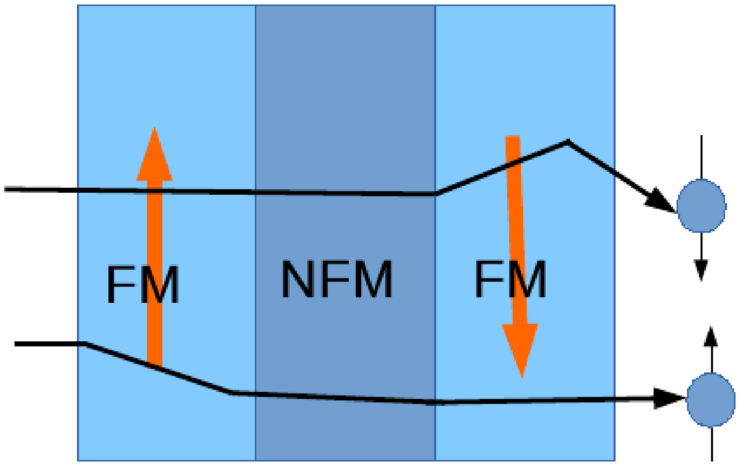

Figure 1.3: (A) Current perpendicular-to- plane (CPP) giant magneto-resistance (GMR) device structure with both ferromagnet magnetic moments aligned parallel to each other. The down spin (up magnetic moment) electrons face weaker scattering than the spin up (down magnetic moment) electrons. (B) CPP-GMR with the ferromagnet magnetic moments aligned anti-parallel to each other. In this case both spin up (down magnetic moment) and spin down (up magnetic moment) electrons face the same numbers of scattering events during the transport. FM and NFM stand for ferromagnetic and non-ferromagnetic metal respectively.

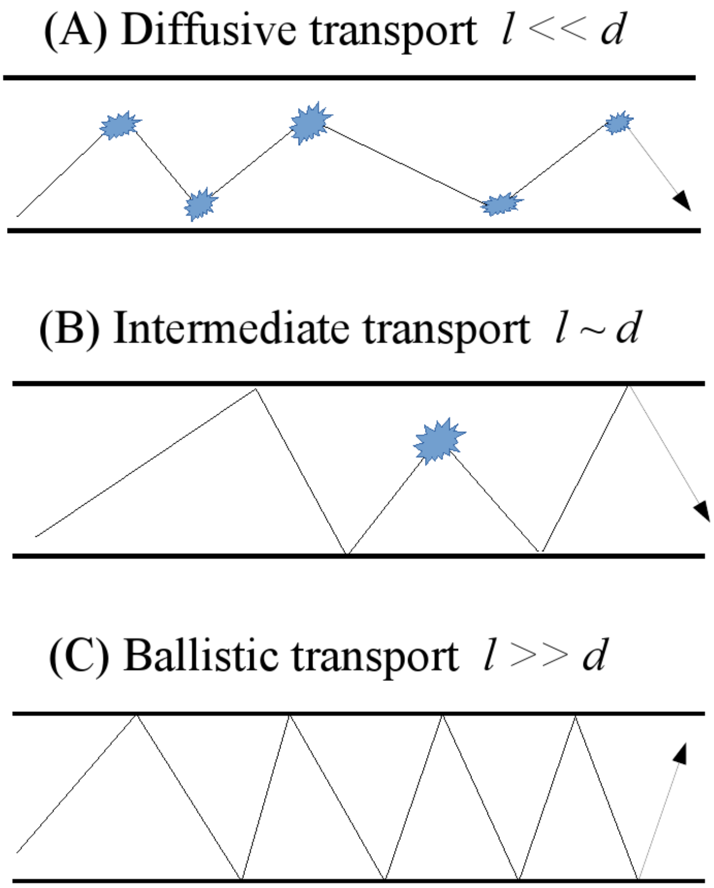

Figure 1.4: (A) Diffusive transport when the electron diffusion length, l, is very small compared to the thickness of the device d. The scattering centres are shown with stars. (B) The intermediate transport regime is when the spin diffusion length, l, is comparable to the thickness of the device d. In the intermediate transport regime there are only few scattering centres compared to the diffusive transport. (C) Ballistic transport is when the electron diffusion length, l, is large compared to the thickness of the device d. In the ballistic transport regime there is no scattering centre and the transport is fully elastic.

1.3 TMR

After CIP GMR and CPP GMR a new technology emerged, known as tunnelling magnetoresistance (TMR). The geometrical structure of a TMR junction is very much the same as that of CPP GMR except that the spacer (non-ferromagnetic metal) is now replaced by a wide band-gap insulator. For this reason the working principle of the two devices is very different. CPP GMR devices work on the two-spin channel model for metals, whereas in TMR-based devices the two-spin model has to be combined with a tunnelling model. There are two way to describe the working principle of TMR-based devices. The first is called *Julliere's* model [11] and the second is called the *band-picture* model. Julliere fabricated Fe|Ge|Co amorphous magnetic tunnel junctions (MTJ) and measured the current in both the parallel and anti-parallel configuration of the magnetic moments of the iron and cobalt electrodes (see in Figure 1.5). He observed that the MTJs have a higher resistance in the anti-parallel configuration when compared to the parallel configuration. He proposed a simple explanation for his observation, which is further known as Julliere's model. Julliere's model [11] is based on the product of the polarized density of states of both electrodes. He [11] established a simple formula for the TMR ratio, namely TMR $= \frac{2P_1P_2}{1-P_1P_2}$, where P_1 and P_2 are the spin polarization of the left and right ferromagnetic electrodes. The spin polarization is simply defined as $P = \frac{D_\uparrow - D_\downarrow}{D_\uparrow + D_\downarrow}$, with D_σ being the density of states of the majority ($\sigma =\uparrow$) and minority ($\sigma =\downarrow$) electrons. Generally, however, the spin polarization of the current is not directly proportional to the polarization of the density of states [12]. This very much depends on the experiments at hand. The spin polarization of transition metals is of the order of 50%. Julliere's model thus suggests a small TMR, $\sim 60-70\%$, in transition metal ferromagnet based magnetic tunnel junctions. In the nineties such predictions have been confirmed in many experiments mostly using amorphous Al_2O_3 as the insulating spacer [13] [14]. Julliere's model [11] has nothing to say about the effect of insulating barriers on TMR, meaning that its electronic structure

(A) Parallel configuration

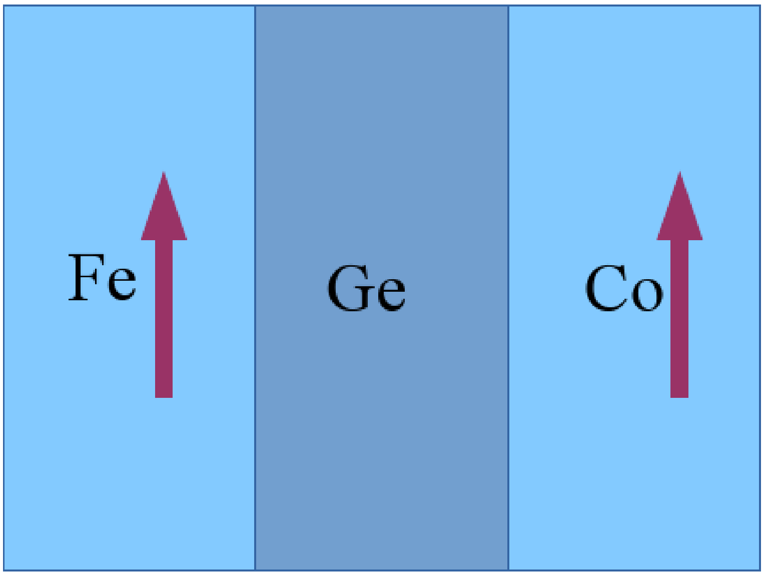

(B) Anti-parallel configuration

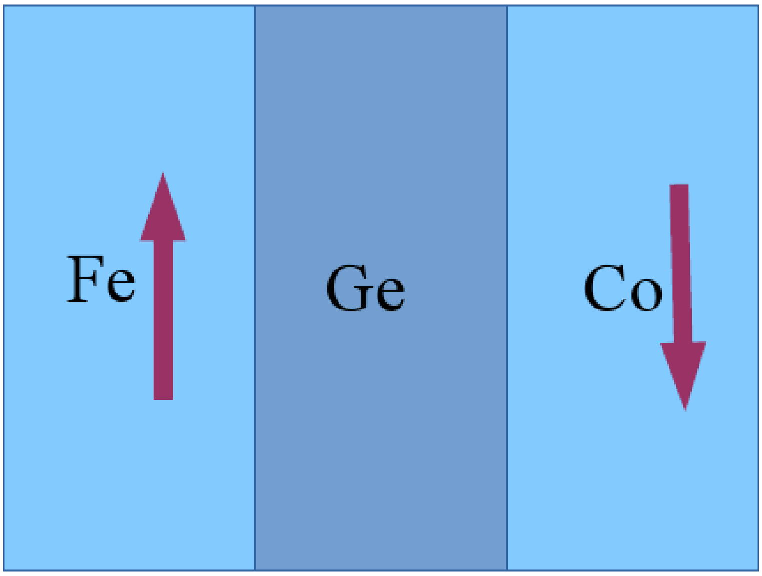

Figure 1.5: Schematic diagram of the germanium (Ge) based Julliere device, Fe|Ge|Co. This is an amorphous magnetic tunnel junction (MTJ) and it is here pictured in the parallel (A) and anti-parallel (B) configuration of the ferromagnet electrodes magnetic moments.

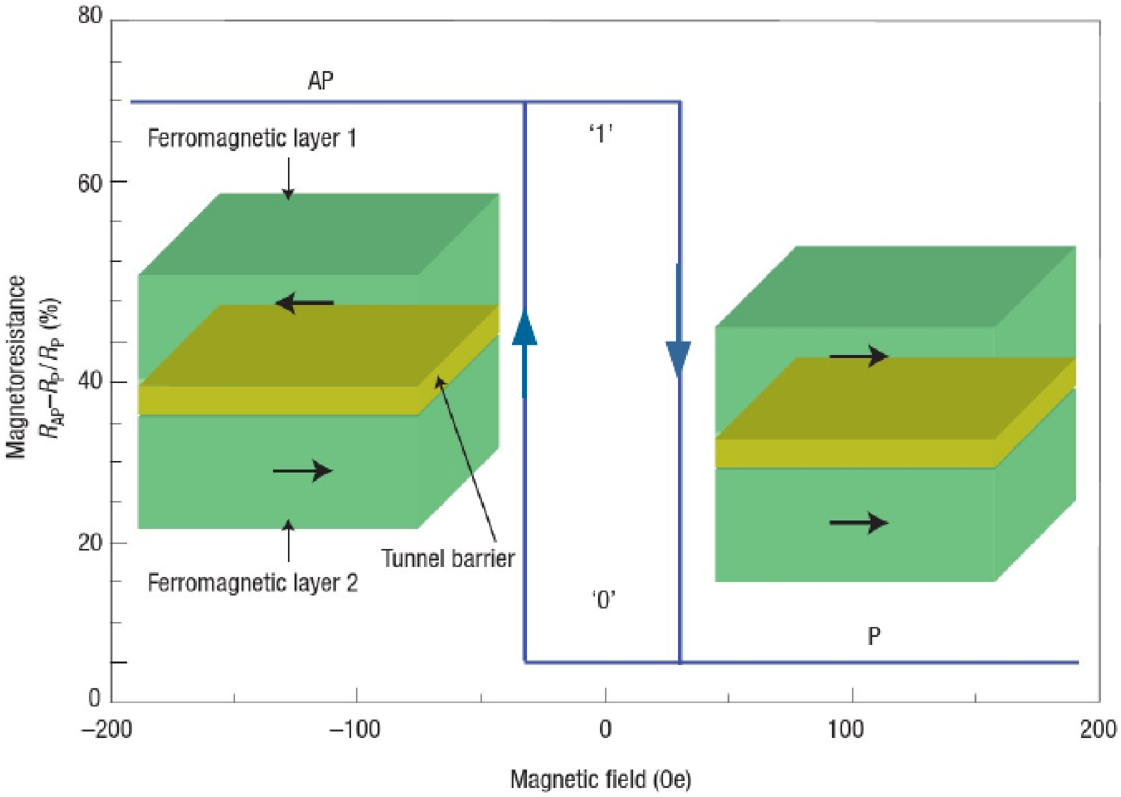

Figure 1.6: Schematic of a tunnelling magneto-resistance magnetic tunnel junction device structure. The blue lines describe the magnetic response (hysteresis) of the junction. The arrow in the hysterias curve shows the swapping direction of magnetic field [1].

does not enter into the definition of the TMR.

The other model, known as the *band-picture* model, is based on the symmetry filtering of the Bloch state by the insulating material. In this model the role of the insulating barrier material has been incorporated. In this, the symmetry of the Bloch states that are filtered solely depends upon the insulating barrier material (for more details see chapter 4, subsection 4.2.3). The insulating barrier material allows only certain symmetry of the Bloch state (for classification of Bloch state see chapter 4, section 4.3) to tunnel easily, while other symmetries have lower tunnel probability. This is a characteristic property of the insulating material. The working principle of the TMR based MTJs is as follows: A TMR device is made of two ferromagnet electrodes and an insulating barrier sandwiches between them (see in Figure 1.6). The magnetic moment of one ferromagnetic layer is fixed in one direction and this is called the fixed layer (denoted by ferromagnetic layer 2 in the figure 1.6). The magnetic moment of the other ferromagnetic layer is free to rotate and is called the free layer (denoted by ferromagnetic layer 1 in the figure 1.6). When the magnetic moments of the ferromagnetic electrodes are parallel and the current is perpendicular to the interfaces plane, then the resistance of the device is usually at a minimum, whereas when the magnetic moments of the ferromagnetic electrodes are anti-parallel to each other then the resistance of the device is a maximum (see in Figure 1.6). These two very stable states (minimum and maximum) in binary terms can be labelled as "zero" and "one" (see in Figure 1.6). The minimum resistance of the device is R_P, whereas maximum resistance of the device is R_{AP}. The TMR of the MTJs device is then defined as $\left(\frac{R_{AP}-R_P}{R_P}\right) \times 100$ (see in Figure 1.6). The major break-through in TMR MTJs came in early 2000s when Butler [3] and Mathon [15] independently demonstrated that epitaxial MTJs could in practice sustain an arbitrarily large TMR. In epitaxial MTJs the transverse components of wave-vector ($k_{||}$) remains conserved during the tunnelling across the insulator and it coupled strongly with certain symmetry of the Bloch states. In other words, the insulator favours one Bloch state symmetry to tunnel easier than the others. By doing this the insulator filters one symmetry of the Bloch state in the tunnelling process. For example in the case of Fe|MgO|Fe junction, Butler [3] and Mathon [15] demonstrated that it is the Δ_1 symmetry of the Bloch states (for symmetry classification of the Bloch states, see in figure 1.7), which is available at Fermi energy level in the iron ferromagnet along the [001] direction that is filtered by the MgO insulator during tunnelling in [001] direction.

The remaining symmetries of the Bloch state, like Δ_2, $\Delta_{2'}$ and Δ_5 (for symmetry classification of the Bloch states, see in figure 1.7), decay at a faster rate than the Δ_1 during the tunnelling process when the transport is along the [001] direction (see in Figure 1.8). Since the Δ_1 symmetry is available at the Fermi level only for one spin direction (majority) the Fe/MgO structure behaves as a half metal and the TMR is very large. Soon

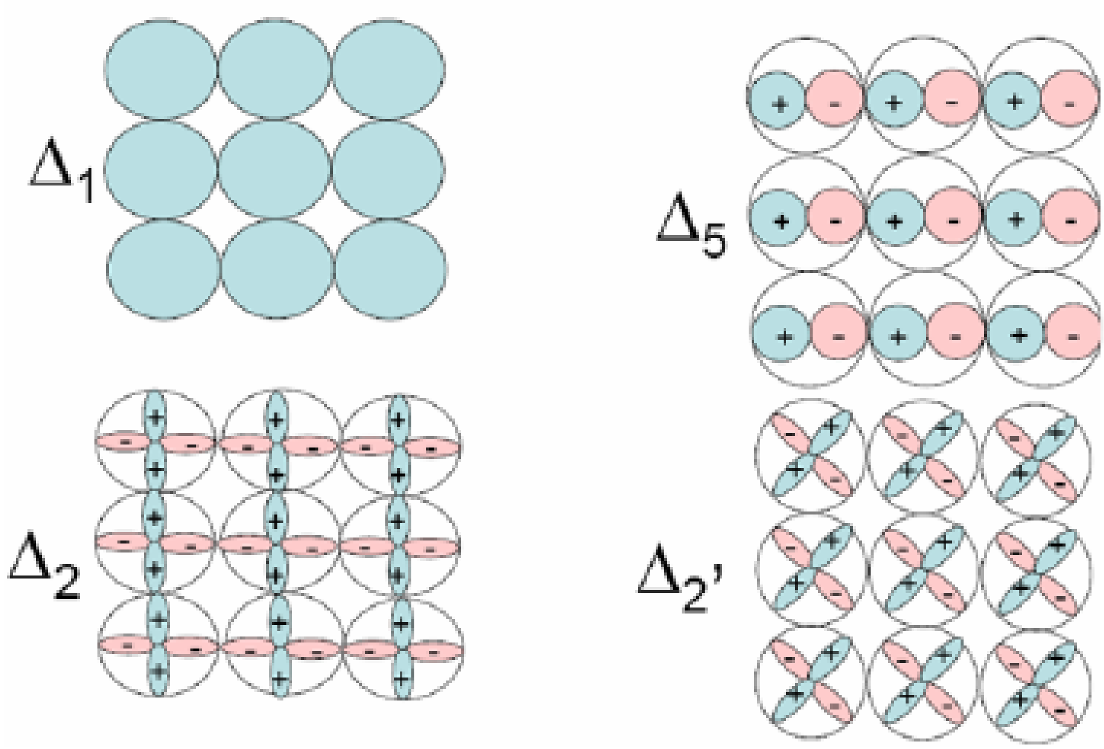

Figure 1.7: Classification of the Bloch states symmetry according to their projection on to the $x - y$ plane.Bloch states of s, p_z and d_{z^2} symmetry are called Δ_1-like states. Bloch states transforming as p_x, p_y, d_{xz} and d_{yz} symmetry are called Δ_5-state. The Bloch state with d_{xy} symmetry is called $\Delta_{2'}$. Bloch state of $d_{x^2-y^2}$ symmetry is called Δ_2. One has to consider their symmetry with respect to rotations about the z axis [2].

such predictions were confirmed experimentally with observed TMRs of around $\sim 200\%$ in Fe|MgO|Fe [4] and [001] oriented FeCoB|MgO|FeCoB [16] junctions. Both these MgO-based MTJs are the building block for magnetic data-storage and for the magnetic sensors used in various applications [17].

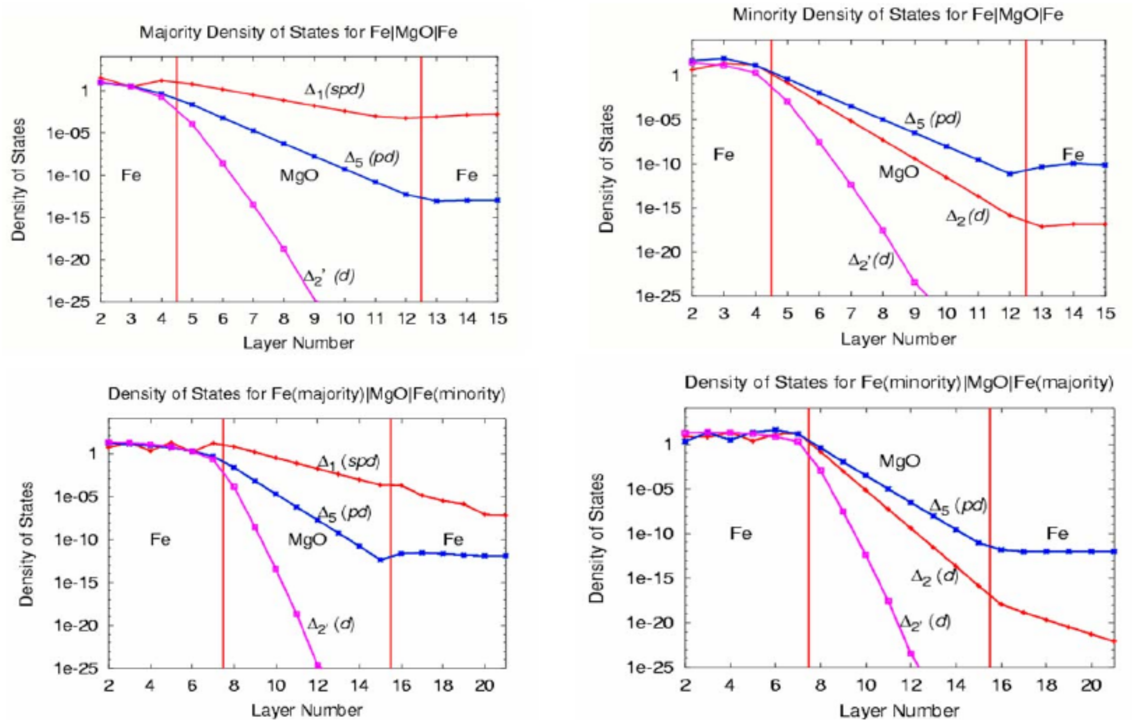

Figure 1.8: Schematic diagram of the probability of transmission of the different symmetries of the Bloch state in the Fe|MgO|Fe junctions. The top left for the majority (spin up) and the top right for the minority (spin down) electrons when the ferromagnetic moments are parallel to each other. In the bottom left and the bottom right panel are the case for the majority and minority electrons, when the ferromagnetic moments are anti-parallel to each other [3].

1.4 Need for alternative of Fe/MgO/Fe MTJ

The Fe|MgO|Fe tunnel junction has revolutionized the hard-disk industries, yet despite its success it remains the only commercially viable tunnel junction. In spintronics several interesting phenomenon have been discovered which if combined with a tunnel junction could make the next revolutionary device, for example optical switching, spin torque MRAM, spin torque oscillators. To observe these effects requires careful selection of materials. It is therefore necessary for future development of spintronics devices to consider alternative materials from which to make the most likely common component of any devices the spin valve. The design criteria for spintronics is not as stringent as for hard-disk-drive. We require room temperature magnetism but only a detectable magneto-resistance. In this thesis we have selected two sets of ferromagnetic junctions. One is based on very wide band-gaps insulators, namely HfO_2 and SiO_2, whereas the other based on medium band-gaps display materials such as ZnO, GaN, and AlN. HfO_2, and SiO_2, semiconductors materials are widely uses as an insulators in microelectronics industries and their fabrication rule are well known. Similarly ZnO, GaN, and AlN (also known as display materials) are widely uses in display industries and their fabrication rule is also well known. These materials were selected because these materials can be easily integrated in microelectronics industries.

Current practical MTJ structure consists of a free layer, tunnel barrier, pinned layer, ruthenium layer for Ruderman-Kittel-Kasuya-Yosida (RKKY) coupling, ferromagnetic layer and anti-ferromagnetic layer ($\mathrm{Pt-Mn}$ or $\mathrm{Ir-Mn}$) (see in Figure 1.9) [4]. This device stack has been grown on $\mathrm{Pt-Mn}$ or $\mathrm{Ir-Mn}$ fcc-(111) plane. Growing a full-junction requires atleast 12 stacks of different materials which requires expensive lithographic processing (see in Figure 1.10). Also $\mathrm{MgO}-[100]$ interface has a 4-fold symmetry, whereas $fcc-(111)$ plane has a 3-fold symmetry. The 4-fold symmetry plane can not grow on the 3-fold symmetry planes. We need an alternative insulator which can be grown eas-

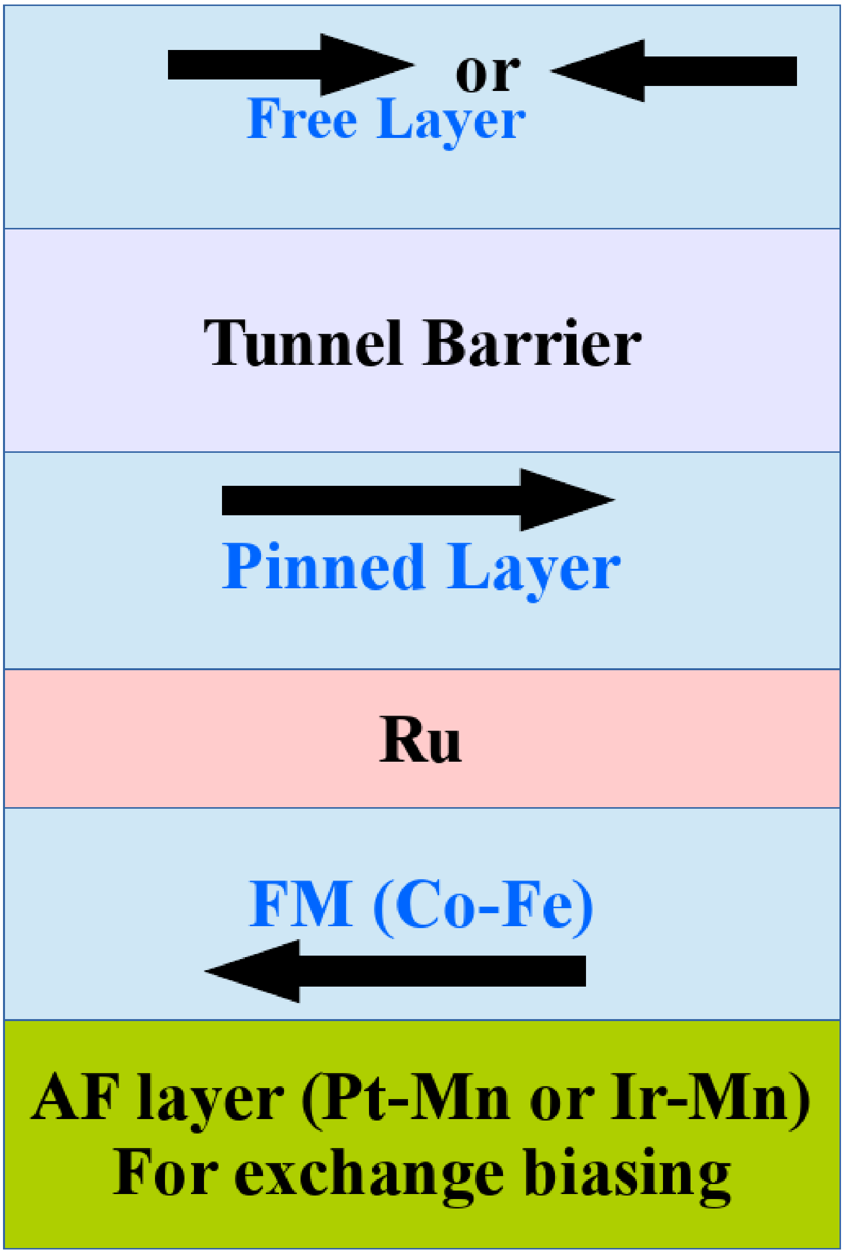

Figure 1.9: Schematic diagram of a typical magnetic tunnel junction. AF stand for anti-ferromagnet, FM stand for ferromagnetic (e.g Co-Fe), Ru stand fo ruthenium metal, pinned layer correspond to fixed ferromagnetic material moments in certain direction, and free layer correspond to free magnetic moment which free to follow any externally applied magnetic field [4].

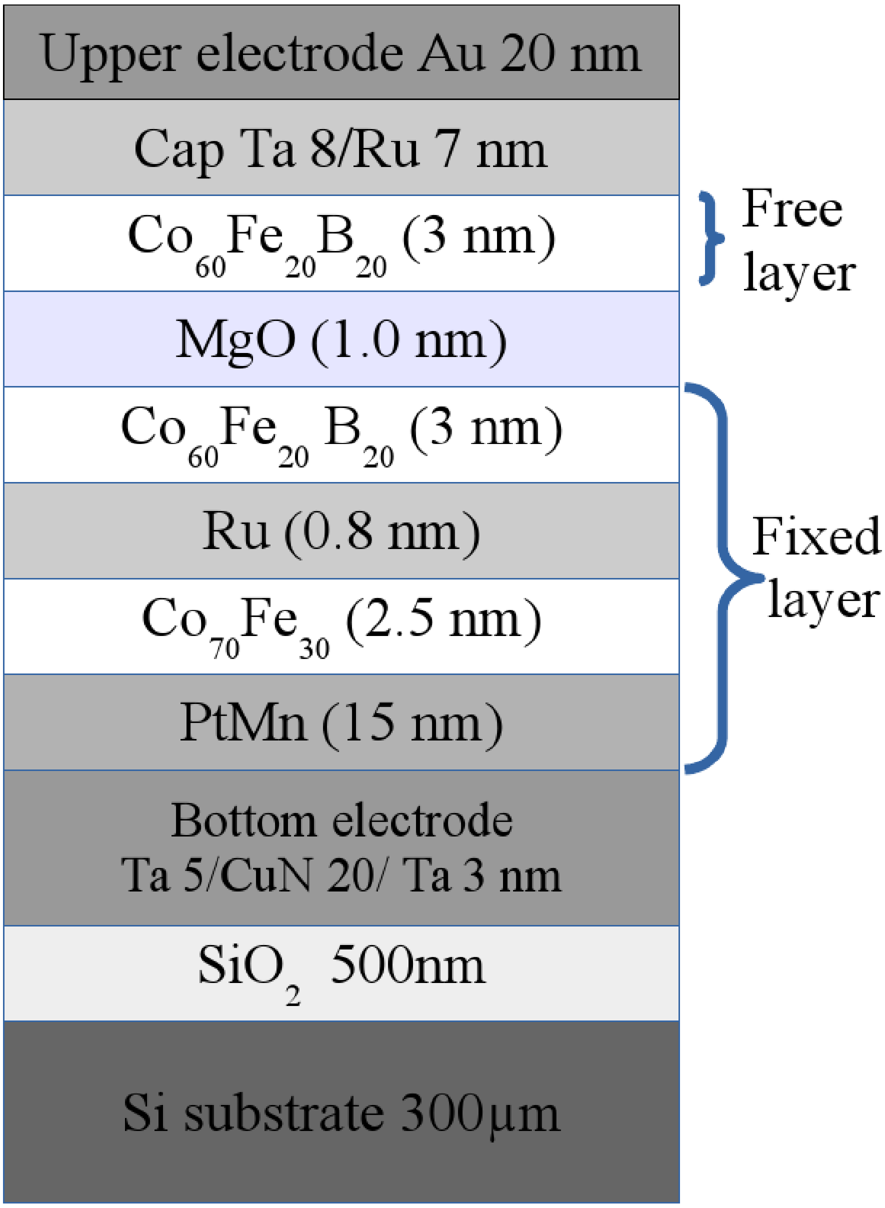

Figure 1.10: Schematic diagram of a typical Fe|MgO|Fe based magnetic tunnel junction consist of different stacks of materials with optimised thickness for better performance of MTJ. [4].

ily on the $fcc-(111)$ ferromagnet and perform similarly as MgO does in a Fe|MgO|Fe junction. Also the ferromagnet should have enough anisotropic energy so that the rotation of the magnetic moment is stable against thermal fluctuations and it can be fixed along one specific direction. Generally, iron is not a desirable candidate because of the thickness dependent anisotropic energy in which flipping of a domains magnetic moment energy $\sim \sum_i D_i$, where symbol D_i represents the anisotropic energy of every spins in the magnetic domains that present in the thin films. Some time this energy is very low, less than the thermal energy, therefore we need an alternative ferromagnet which has enough anisotropic energy and can be grown easily on different substrates as well as on insulators. Currently Fe|MgO|Fe junction used as a read-head in hard-disk drives [18] and in spin transfer torque magnetic random access memory (STT-RAM). The Gilbert damping parameter α, of Fe, Co, and Ni are large [19]. For spin-transfer torque we need low Gilbert damping and small (but sufficiently large anisotropic energy greater than the thermal energy to negate thermal effect during classification of device states) anisotropic energy so that a small current and voltage (small power) is enough for writing the single magnetic bit in data storage [18]. The scientific community also uses Fe|MgO|Fe junctions for generating microwave signals [20] [21]. For microwave signals we need low Gilbert damping ferromagnet so that the magnetic moments of the ferromagnet can precess with less dissipation. Currently uses ferromagnet such as Fe and Co have high Gilbert damping and thus large amount of power required to drive them for required frequency microwaves [21]. Still power in microwave signals remains quite low for any practical application [21]. So we need an alternative ferromagnetic materials as well as alternative insulators which can grows and commensurate at the interfaces of MTJ. In this thesis we will only focus on the insulators $(\mathrm{HfO_2}, \mathrm{SiO_2}, \mathrm{ZnO}, \mathrm{GaN}, \mathrm{AlN})$ and its symmetry filtering capabilities. We will not search for new ferromagnet, instead, we will use conventional ferromagnet $(\mathrm{Fe}, \mathrm{Co}, \mathrm{Ni})$ in our MTJs. Our MTJs analysis is very general, and any new ferromagnet (if discover in future) can be accommodated. The only condition is that the new ferromagnet lattice parameter must be commensurate at the interfaces in order for coherent tunnelling and symmetry filtering by the insulators. We will use the density functional theory (see in chapter 2, for detail discussions) for ground state electronic properties of the materials, and Smeagol software code which based on the non-equilibrium Green's functions for transport (see in chapter 3, for more detail derivations and discussions). MTJs transport set-up and TMR calculation procedures that have been used in this thesis have been discussed in great details in chapter 4.

In theory, we have designed a perfect junctions, which are well commensurate at interface, but in practice junctions generally are not commensurate, which leads to imperfections and various defects at the interface. Fe|MgO|Fe junction has a commensurate interfaces after rotating Fe[100] crystal planes by 45^0 (see in Figure 1.11). This is one of the reason why almost all the spintronics based devices are based on Fe|MgO|Fe crystalline stacks. In perfect crystalline MTJ (e.g. Fe|MgO|Fe)(see in Figure 1.11) the transport is mainly based on the perfect coherent tunnelling of the electrons across the insulator (see in Figure 1.12). However, if a junction is not perfect then the transport is mainly based on the incoherent tunnelling since if an electron tunnels across the imperfect junction then the phase information of the wave will be lost after multiple scattering with impurity/defects. This results in the discrepancy between the nearly infinite TMR calculated by considering the perfect coherent tunnelling and the real experimented values observed. The discrepancy need to be explained using Julliere's model which counts incoherent tunnelling effect. In real device both coherent and incoherent tunnelling currents will remain present. Also, for coherent tunnelling the potential energy barrier must be flat. If there is any slope in the potential energy barrier then it could be elastic tunnelling where energy still remains conserved but phase information of the wave will be lost after multiple scattering during the tunnelling across the barrier. Also, there will be a thermionic current

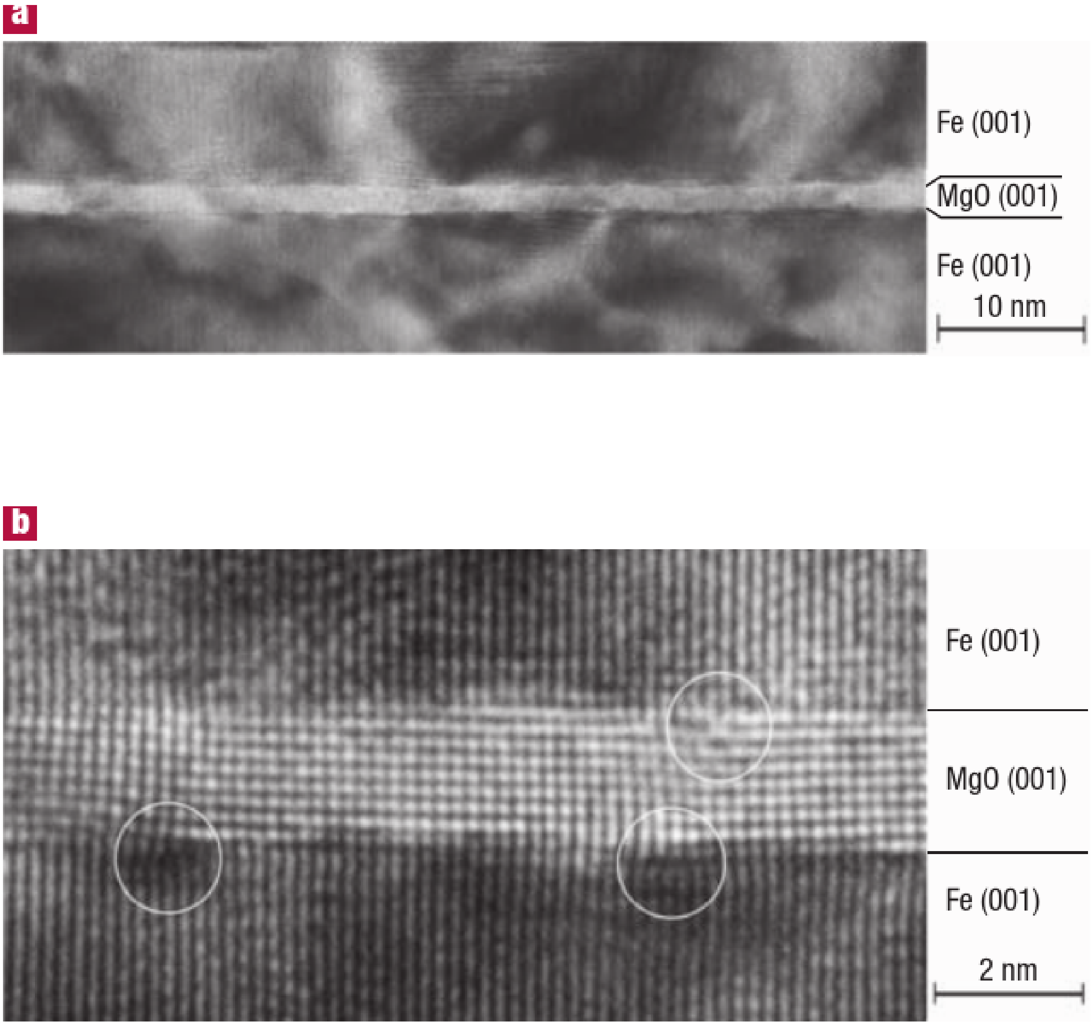

Figure 1.11: (a) Transmission electron microscopy (TEM) images of Fe[001]|MgO[001](1.8nm)|Fe[001] structure. The vertical and horizontal directions are correspond to MgO[001](Fe[001]) axis and MgO[001](Fe[001])axis respectively. The lattice spacing of MgO is 0.221nm along the [001] axis and 0.208nm along the [100] axis. (b) is the magnification of (a). The lattice of the top Fe electrode is slightly expanded along the [110] axis. The lattice dislocations are circled in fig. (b). Figure reproduced from ref. [4].

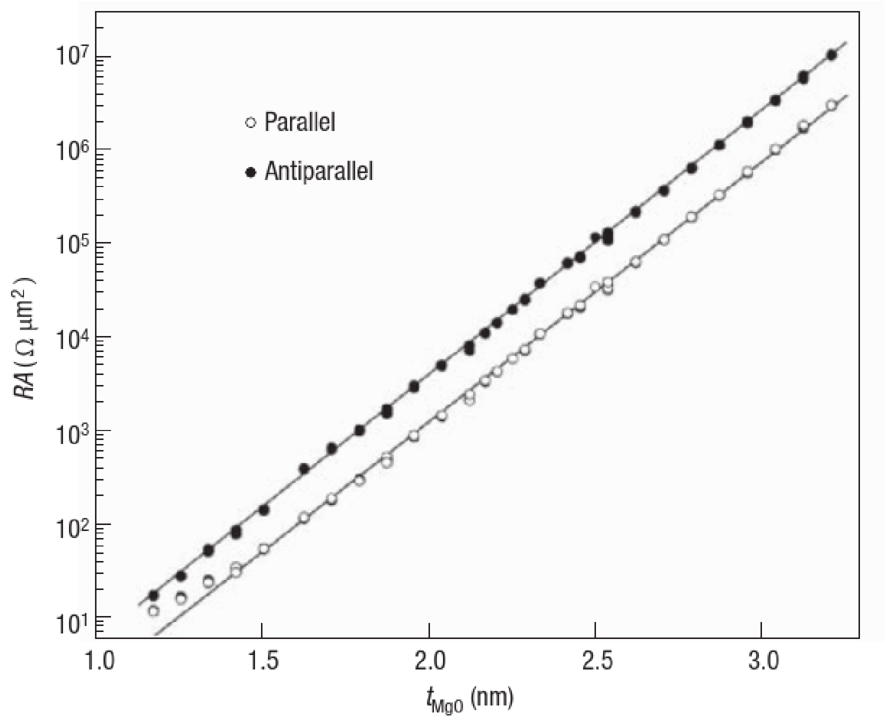

Figure 1.12: Resistance of the parallel and anti-parallel magnetic moments configuration of Fe|MgO|Fe junction as a function of MgO thickness. MgO cross section is $1\mu m \times 1\mu m$. The logarithmic plot on y-axis suggest that there is almost perfect tunnelling across the MgO junction. Figure reproduced from ref. [4].

(also called Richardson current) when device is in operation. These are not included in the non-equilibrium Green's function formalism (NEGF). So although these may be seen experimentally but they will not appear in our calculations. Also, which current dominates at any particular voltage is also difficult to answer straight forwardly. However, fitting the thermionic current equation and tunnelling current equation simultaneously to the experimental current can provide some information. Generally, real devices do have a certain degree of imperfection at the interfaces (see in Figure 1.11) [4]. Designing and analysing the imperfect junctions are quite difficult. A number of problems arise during the analysis of imperfect junction and can be written as follows: **(1)**, a full-junction generally contains many computational atoms. Relaxing a non-commensurate junction will take a much longer time than the relaxing commensurate junction. Also, we need to simulate many junctions with different defect concentrations as we are always in the coherent transport regimes. It is also known that the biggest killer of spin currents is the unpinned magnetic atoms at the interfaces. **(2)**, knowing electronic coupling between lead and device region are the prerequisite for quantum transport. In non-commensurate junction with defect/impurity at the interface we don't know how the device region couples with the left and right lead, and even if one manage it by self-consist calculation, still coupling strength and its physical reliability need to tested/investigated. **(3)**, if the junction is non-commensurate then whether a real device will still work in quantum transport regime needs to be investigated, because, once the device is in operation then the thermionic current will also contribute. **(4)**, impurities generally produce localized energy states in the band-gap. How localized energy states change the tunnelling current, and if the density of localized energy states increases by increasing the density of the impurity at the interface, then still can we call it tunnelling current needs to be investigated. In a real device the concentration and distribution of impurities are generally unknown, and to reach any conclusion for such devices, analysis after varying the impurity concentrations with energies are very imperative. Therefore, in this thesis we will analyse only perfect commensurate junctions. In our magnetic tunnel junctions ($\mathrm{HfO_2}, \mathrm{SiO_2}, \mathrm{ZnO}, \mathrm{GaN}, \mathrm{AlN}$), transport are mainly concentrated around the Γ-point in the first Brillouin zone. The important Bloch states have higher wavelength in the transverse plane ($x - y$-plane, because we have taken the transport direction in all our MTJs in along the z-axis). We expect that at the Γ-point mostly Bloch states have higher wavelength along the transverse directions, and any roughness that present at the interfaces will not be spatially resolved by the slowly varying wavelength along the transverse planes. We then can treat the transport across the real MTJs as a coherent tunnelling transport where symmetries of the wave-function will remain preserved.

1.5 Thesis Layout

The main focus of this dissertation is on the study of future potential tunnel barriers for MTJs, mostly to be used as read heads in the hard-disk drive industry. In our MTJs transport analysis we will follow the Butler et al. [3] symmetry filtering argument by the insulators using complex wave-vector analysis in the first Brillouin zone. We have briefly covered DFT and its formalism to obtain the ground-state electronic properties of materials. We have also briefly covered the scattering theory used in quantum transport in nano-structures. We have then selected the wide band-gap insulators like HfO_2 and SiO_2, which are widely used in the micro-electronics industry and analysed them as a potential tunnel barrier for future MTJs. We have also analysed display materials like ZnO, GaN and AlN as tunnel barriers for MTJs, which can be further integrated into the display industry for various applications.

The work in this thesis is arranged as follows:

Chapter 2

In this chapter we will discuss the density functional theory (DFT) formalism, the Hohenberg and Kohn theorems, the Kohn-Sham equations, the exchange-correlation functional, the Slater and Kohn-Sham exchange-potential, the derivation of the exchange-correlation functional in the slowly and highly varying density regime, the atomic self-interaction correction (ASIC) method, the pseudo-potentials and the pseudo-potential generation scheme.

Chapter 3

In this chapter we will discuss the non-equilibrium Green's function formalism and its implementation in the Smeagol software package. We will derive the non-equilibrium Green's functions using the Lippmann-Schwinger equation. We will divide the entire system into three parts, namely the left-lead, the scattering-region and the right-lead, and discuss the Green's function and Hamiltonian for each region. We will discus the Fourier transform of the Lippmann-Schwinger equation, the spectral representation of the Green's function, the energy re-normalization and the life time of the eigenstate, the density matrix, the current per channel, the transmission coefficients and the total current. Finally, we will show that the final transmission equation is similar to the Landauer-Büttiker equation for quantum transport.

Chapter 4

In this chapter we will discuss the general features of TMR and of magnetic tunnel junctions and their design. We will review the theory of TMR, including: Julliere's model, the Landauer-Büttiker theory, the simple barrier model, the classification of the Bloch states, the $k_x - k_y$ decay plot of the Bloch wave-function in the first Brillouin zone, the complex-band analysis, the selection of the ferromagnet electrode, the design of the magnetic tunnel junction, the band off-set calculation, the relaxation of MTJs interface and the Siesta-Smeagol calculation set up for the transport.

Chapter 5

In this chapter we will investigate HfO_2 and SiO_2 as future tunnel barriers for MTJs read-head applications. We will give details of symmetry filtering by HfO_2 and SiO_2, the selection of the ferromagnetic electrodes, the formation of Fe/HfO_2/Fe and Co/SiO_2/Co TMR junctions, the Siesta-Smeagol calculations and the transmission analysis. We will show that in-spite of cobalt supplying both spin up and spin down $\Delta_{2'}$ symmetry of the Bloch state in [001] transport direction, SiO_2 still has significant zero-bias TMR due to the different orbital character of $\Delta_{2'}$ bands. The HfO_2 has fairly good zero-bias TMR, however, operation voltage window is small $\sim 0.5V$. Finally we will conclude the chapter and discuss the future perspectives of MTJs.

Chapter 6

In this chapter we will investigate ZnO, GaN and AlN as potential tunnel barriers for read-head applications. ZnO is a wide direct band-gap semiconductor having an experimented band-gap of ~ 3.25eV [22]. GaN and AlN are also direct band-gap semiconductors with band-gap of ~ 3.15eV [23] and ~ 6.1eV [23], respectively. We will investigate ZnO, GaN and AlN symmetry filtering ability, the transport supporting-points in the first Brillouin zone, the band-offset with the ferromagnetic electrodes (iron and cobalt) and finally we will analyse the transmission in Fe(Co)/ZnO/Fe(Co), Fe(Co)/GaN/Fe(Co) and Fe(Co)/AlN/Fe(Co) junctions. We will show that although these display materials are very promising candidates for spintronics application, *bcc* iron and *bcc* cobalt ferromagnets supply both spin up and spin down Δ_1 symmetry of the Bloch state at the Γ-point in these display materials and thus the resultant TMR is low. At the K-point in the first Brillouin zone, *bcc* cobalt supplies only spin down and *bcc* iron supplies both spin up and spin down $\Delta_{2'}$ symmetry of the Bloch states. At the M-point in the first Brillouin zone, *bcc* cobalt supply both spin up and spin down Δ_1, whereas *bcc* iron supply both spin up and spin down $\Delta_{2'}$ symmetry of the Bloch state. Since iron and cobalt ferromagnets are unable to supply only one spin with Δ_1 symmetry at the supporting-points in the transport direction, the zero-bias TMR turned out to be low. At the end of the chapter we will conclude our work and discuss the future perspective of TMR.

Chapter 7

In this chapter we will conclude our work on HfO_2, SiO_2, ZnO, GaN and AlN as potential tunnel barriers and provide future perspectives on how to design MTJs.

Chapter 2

Density Functional Theory

2.1 Introduction

Hohenberg and Kohn in 1964 [24] and Kohn and Sham in 1965 [25] published two seminal papers on density functional theory (DFT), one of its main approximations and the recipe to solve the DFT fundamental equations. In 1964 Hohenberg and Kohn proposed that any measurable ground-state quantity of an interacting electronic system can be calculated and measured by knowing the ground-state electron density of that system. Before this discovery, there was a general belief in the scientific community that one must find the ground-state wave-function of the system first and then from this calculate any measurable quantity of the system. The procedure to obtain the ground-state wave-function requires solving the Schrödinger equation, which for a many-body system is extremely complicated and for more than 10 electrons it is almost impossible to solve it exactly. In the Schrödinger picture the total Hamiltonian (non-relativistic) of a system of M nuclei and N electrons can be written as

$$H = \frac{-\hbar^2}{2m_e}\sum_i^N \nabla_i^2 - \frac{\hbar^2}{2M_I}\sum_I^M \nabla_I^2 + \frac{1}{2}\sum_{i\neq j}\frac{e^2}{|r_i - r_j|} - \sum_{i,I}^{N,M}\frac{Z_I e^2}{|r_i - R_I|} + \frac{1}{2}\sum_{I\neq J}^{M}\frac{Z_I Z_J e^2}{|R_I - R_J|}. \quad (2.1)$$

In above equation, m_e represents the mass of the electron, ∇ is the Laplace operator, M_I represents the mass of I^{th} ion (nuclear mass), r_i is the coordinate of i^{th} electron, R_I

that of the I^{th} ion, Z_I is the nuclear charge of the I^{th} ion and e is the charge of electron ($1.6 \times 10^{-19} C$). Since the mass of the any typical nucleus is almost 1000 times larger than the electron mass the dynamic response of a nucleus will be much slower (longer in time scale) than that of the electrons. Thus, one can ignore the dynamics of the nucleus on the time scale of the electron response. This approximation is called the Born-Oppenheimer approximation. In this approximation, the total wave-function ψ of the system is the function of electronic and nuclear coordinates, but the nuclear coordinates can be treated as a parameter because one can calculate the dynamics of electrons with one particular configuration of nuclear system. In other words,

$$\psi(\{\mathbf{r}\}, \{\mathbf{R}\}, t) \cong \psi(\boldsymbol{\{r\}}, t; \boldsymbol{\{R\}}) \equiv \psi(\mathbf{r}, t; \boldsymbol{R}). \tag{2.2}$$

Therefore, the dynamics of the electrons will change as the configuration of the nuclear system changes. Thus, the wave function $\psi(\boldsymbol{r}, t; \boldsymbol{R})$ of the system depends on $\mathbf{r}$ and $\mathbf{R}$, where $\mathbf{r}$ is the position vector of the electrons and $\mathbf{R}$ is the position vectors of nuclei. Since most of the time we are only interested in time independent problems, we will ignore the time dependent part and will solve the time independent Schrödinger equation. In a time independent picture the wave-function can be factorized in terms of position and time dependent coordinates explicitly,

$$\psi(\mathbf{r}, \mathbf{R}, t) = \phi(\boldsymbol{r}, \boldsymbol{R}) \times f(t). \tag{2.3}$$

If we apply the Born-Oppenheimer approximation to the full Hamiltonian of the system, then we can drop the kinetic energy term of nuclear ions $[-\frac{\hbar^2}{2M_I}\sum_I \nabla_I^2]$. Since we are only interested in the dynamics of the electrons, we will treat electrons as our system of interest and the rest part (the nuclear configuration) as a static electric potential. In this scenario, the potential at the position $\mathbf{r}$ generated by the nuclear ions will act as a external potential for the electrons and thus the total potential energy of electronic system can be written as

$$V_{\text{ext}} = -\sum_{i,I} \frac{Z_I e^2}{|r_i - R_I|}. \tag{2.4}$$

Since nuclear ions are also interacting between themselves through coulomb field, therefore total ionic interaction energy can be written as

$$E_{\text{ion}} = \frac{1}{2} \sum_{I \neq J} \frac{Z_I Z_J e^2}{|R_I - R_J|}. \tag{2.5}$$

After having applied the Born-Oppenheimer approximation to the full Hamiltonian (2.1) of the system, the new electronic Hamiltonian becomes

$$H = \frac{-\hbar^2}{2m_e} \sum_i \nabla_i^2 + \frac{1}{2} \sum_{i \neq j} \frac{e^2}{|r_i - r_j|} + V_{ext}(r, R_I) + E_{ion}. \tag{2.6}$$

The first term in the above Hamiltonian is the kinetic energy of the electrons. The second term is the total Coulomb potential energy of the electrons. The third term is the total external potential energy due to the nuclei and the fourth one is the total ionic potential energy of the nuclei (this is a constant for a fixed nuclear configuration).

Due to the presence of the electron-electron interaction, this Hamiltonian is extremely difficult to solve analytically for a system comprising even a modest number of electrons. At this point, density functional theory steps in and tries to address this problem by using a density functional theory formalism rather than looking for the total wave-function of the system. Hohenberg and Kohn put forward two theorems, which founded DFT.

Theorem 1: The external potential $[v(\overrightarrow{r})]$ (up to a constant) is a unique functional of the ground-state electronic density $n(\overrightarrow{r})$. Alternatively $n(\overrightarrow{r})$ uniquely determines the external potential $v(\overrightarrow{r})$ (up to a constant) [24].

We shall prove only the second statement using contradiction.

Consider two potentials $v'(\overrightarrow{r})$ and $v(\overrightarrow{r})$, which give the same ground-state electronic density $n(\overrightarrow{r})$. As such the two potentials $v'(\overrightarrow{r})$ and $v(\overrightarrow{r})$ correspond to different Hamiltonians H' and H. H' and H will give different wave-functions ψ' and ψ. Assume that

ψ' and ψ are the ground-state wave-functions and E' and E are the ground-state total energies correspond to the Hamiltonians H' and H, respectively.

From the variation principle we have

$$E^{'} = \langle\psi'|H'|\psi'\rangle < \langle\psi|H'|\psi\rangle. \tag{2.7}$$

H' can also be written as

$$H' = H + V' - V. \tag{2.8}$$

Replacing H' from equation (2.8) into equation (2.7) we get

$$E^{'} = (\langle\psi'|H'|\psi'\rangle) < (\langle\psi|H'|\psi\rangle) = (\langle\psi|H + V' - V|\psi\rangle). \tag{2.9}$$

After expansion,

$$E' < E + \int [v'(\overrightarrow{r}) - v(\overrightarrow{r})]n(\overrightarrow{r})d\overrightarrow{r}. \tag{2.10}$$

After interchanging the primed and un-primed quantity we obtain

$$E < E' + \int [v(\overrightarrow{r}) - v'(\overrightarrow{r})]n(\overrightarrow{r})d\overrightarrow{r}. \tag{2.11}$$

By adding the above two equations we finally derive

$$E + E' < E + E', \tag{2.12}$$

which is inconsistent. This negates the initial assumption that two the external potentials can give the same ground-state electronic density.

Theorem 2: There exists a universal energy functional of the electronic density $E[n(\overrightarrow{r})]$. There exists a universal energy functional $(F[n(\overrightarrow{r})]$ for $E[n(\overrightarrow{r})]$. $F[n(\overrightarrow{r})]$ consists of the kinetic and interaction energies of the electronic system. The density $n(\overrightarrow{r})$, which minimizes the energy functional $E[n(\overrightarrow{r})]$ will also minimize $F[n(\overrightarrow{r})]$. This same $n(\overrightarrow{r})$ is a exact ground-state density of the system [24].

Proof: Since ψ is a functional of $n(\overrightarrow{r})$, so is kinetic and interaction energy. In mathematical form this statement can be written as

$$F[n] = \frac{-\hbar^2}{2m_e}\sum_i \langle\psi[n]|\nabla_i^2|\psi[n]\rangle + \frac{e^2}{2}\sum_{i\neq j}\langle\psi[n]|\frac{1}{|\overrightarrow{r'}_i - \overrightarrow{r'}_j|}|\psi[n]\rangle. \tag{2.13}$$

The total energy of the system can thus be written as the sum of the universal functional $F[n]$ plus the external potential energy, where the external potential energy can be written as $\int v(\overrightarrow{r'})n(\overrightarrow{r'})d\overrightarrow{r'} + E_{\text{ion}}$.

Mathematically the total energy of the system can be written as

$$E[n] = F[n] + \int v(\overrightarrow{r'})n(\overrightarrow{r'})d\overrightarrow{r'} + E_{\text{ion}}. \tag{2.14}$$

By using the variational principle one can conclude that the total energy $E[n]$ will have a minimum at the ground-state electronic density. Since an analytic form of $F(n)$ is unknown, an approximation to the total energy is required to solve practical problems. Since $F[n(\overrightarrow{r'})]$ is the sum of the kinetic energy and the electron-electron interaction energy of the system, the kinetic energy can be approximated as a sum of the non-interacting single particle kinetic energy, whereas the electron-electron interaction energy is the two particle classical Coulomb energy. Now, $F[n]$ can be written as

$$F[n] = \frac{1}{2}\int n(\overrightarrow{r'})[n(\overrightarrow{r'})]\frac{1}{|\overrightarrow{r'} - \overrightarrow{r'}|}d\overrightarrow{r'}d\overrightarrow{r'} + G[n], \tag{2.15}$$

where $G[n]$ is also a universal functional like $F[n]$. $G[n]$ can be written then as

$$G[n] = \frac{1}{2}\int \nabla_{\overrightarrow{r'}}\nabla_{\overrightarrow{r'}}n_1(\overrightarrow{r'},\overrightarrow{r'})|_{\overrightarrow{r'}=\overrightarrow{r'}}d\overrightarrow{r'} + \frac{1}{2}\int\frac{C_2(\overrightarrow{r'},\overrightarrow{r'})}{|\overrightarrow{r'} - \overrightarrow{r'}|}d\overrightarrow{r'}d\overrightarrow{r'}. \tag{2.16}$$

Here $n_1(\overrightarrow{r'},\overrightarrow{r'})$ is the one particle density matrix, whereas $C_2(\overrightarrow{r'},\overrightarrow{r'})$ is a two particle correlation function defined in term of one and two-particle density matrix.

$$C_2(\overrightarrow{r'},\overrightarrow{r'}) = n_2(\overrightarrow{r'},\overrightarrow{r'};\overrightarrow{r'},\overrightarrow{r'}) - n_1(\overrightarrow{r'},\overrightarrow{r'})n_1(\overrightarrow{r'},\overrightarrow{r'}), \tag{2.17}$$

where $n_1(\overrightarrow{r'},\overrightarrow{r'}) = n(\overrightarrow{r'})$.

If we look at equation (2.16), then we can see that we can define the kinetic energy-density functional.

$$g_{\overrightarrow{r'}}[n] = \frac{1}{2}\nabla_{\overrightarrow{r'}}\nabla_{\overrightarrow{r'}}n(\overrightarrow{r'},\overrightarrow{r'})|_{\overrightarrow{r'}=\overrightarrow{r'}} + \frac{1}{2}\int\frac{C_2(\overrightarrow{r'} - \overrightarrow{r'}/2;\overrightarrow{r'} + \overrightarrow{r'}/2)}{|\overrightarrow{r'}|}d\overrightarrow{r'}, \tag{2.18}$$

where

$$G[n] = \int g_{\overrightarrow{r}}[n] d\overrightarrow{r}. \tag{2.19}$$

$G[n]$ is not a unique functional of n because $g_{\overrightarrow{r}}[n]$ is not unique. For example, if we take

$$\bar{g}_{\overrightarrow{r}}[n] = g_{\overrightarrow{r}}[n] + \sum_{i=1}^{3} \frac{\partial}{\partial x_i} h^{(i)}_{\overrightarrow{r}}[n] \tag{2.20}$$

in equation (2.19), we will get the same $G[n]$ for any arbitrary function h^i. This suggest that $g_{\overrightarrow{r}}[n]$ is not a unique function of n and thus $G[n]$ is not unique.

2.2 Kohn-Sham equations

In principle, density functional theory is exact if the exact functional can be implemented. However, even to this use the minimization of the explicit total energy functional is not easy. In the Kohn-Sham scheme the density of the many-body problem is replaced by that of a non-interacting single-body one. By doing this the Kohn-Sham scheme transforms the complicated many-body Schrödinger equation into solvable single particle Schrödinger equations. The Schrödinger equation of this auxiliary system can be written as

$$\left[-\frac{\hbar^2}{2m} \nabla^2 + v_s(\overrightarrow{r}) \right] \phi_i(\overrightarrow{r}) = \epsilon_i \, \phi_i(\overrightarrow{r}), \tag{2.21}$$

where $v_s(\overrightarrow{r}) = v(\overrightarrow{r}) + v_H(\overrightarrow{r}) + v_{xc}(\overrightarrow{r})$ is the effective single-particle potential of the auxiliary system. The term $v(\overrightarrow{r})$ is an external potential with subscript 's' standing for single-body problem. The term $v_H(\overrightarrow{r})$ is the Hartree potential $\left(v_H(\overrightarrow{r}) = \int \frac{n(\overrightarrow{r'})}{|\overrightarrow{r} - \overrightarrow{r'}|} d\overrightarrow{r'} \right)$, whereas the term $v_{xc}(\overrightarrow{r})$ is the exchange-correlation potential $\left(v_{xc}(\overrightarrow{r}) = \frac{\delta[n(\overrightarrow{r})\epsilon_{xc}(n)]}{\delta n} \right)$. Importantly, the Kohn-Sham auxiliary system is specifically constructed to have the same ground-state density and ground-state energy of the real system. The $\phi(\overrightarrow{r})$, generated from the auxiliary system, will define the ground-state density of interacting (many body) system

$$n(\overrightarrow{r}) = n_s(\overrightarrow{r}) = \sum_{i}^{N} f_i |\phi_i(\overrightarrow{r})|^2, \tag{2.22}$$

where f_i is the occupation number (Fermi-Dirac statistics) of ith Kohn-Sham orbital. The total energy of auxiliary system can be written as the sum of the Kohn-Sham kinetic energy, Hartree potential energy, ions potential energy, external potentials energy, and exchange-correlation energy.

In particular,

$$E[n] = T_{KS}[n] + E_H[n] + \int v(\overrightarrow{r})n(\overrightarrow{r})d\overrightarrow{r} + E_{ion} + E_{xc}[n]. \tag{2.23}$$

Comparing equation (2.14) and (2.23), we can write

$$E_{xc}[n] = F[n] - T_{KS}[n] - E_H[n]. \tag{2.24}$$

It can also be written as

$$G[n] \equiv T_{KS}[n] + E_{xc}[n], \tag{2.25}$$

where $G[n]$ is $\int g_{\overrightarrow{r}}[n]d\overrightarrow{r}$, and n is the ground-state electron density, which minimizes the total energy equation (2.23). $E_{xc}[n]$ is the exchange and correlation energy of an interacting system with density $n(\overrightarrow{r})$.

2.3 Exchange-correlation functional

The total energy $E[n]$ in equation (2.23) contains the $E_{xc}[n]$ term which is the exchange and correlation energy. Such energy is defined as the sum of the difference between the kinetic energy of the interacting system, $T[n]$, and the non-interacting single-particle kinetic energy $T_s[n]$ (correlation energy), plus the potential energy difference between that of the interacting system, $U[n]$, and the Hartree energy, $U_H[n]$ (exchange energy). Therefore, the exchange-correlation energy term can be written as $E_{xc}[n] = E_x[n] + E_c[n]$, where $E_x[n] = U[n(\overrightarrow{r})] - U_H[n(\overrightarrow{r})]$ is the exchange energy, and $E_c[n] = T[n(\overrightarrow{r})] - T_s[n(\overrightarrow{r})]$ is the correlation energy.

For an arbitrary varying electron density $n[\overrightarrow{r}]$ an expression for E_{xc} is unknown, but if the density varies slowly then E_{xc} can be approximated as

$$E_{xc}[n] = \int n(\overrightarrow{r})\epsilon_{xc}[n(\overrightarrow{r})]d\overrightarrow{r}, \tag{2.26}$$

where $\epsilon_{xc}[n(\overrightarrow{r})]$ is the exchange and correlation energy per electron of a uniform electron gas of density $n(\overrightarrow{r})$.

Since the total number of electrons in the system is conserved ($\int n(\overrightarrow{r})d\overrightarrow{r}$ =N), one has the condition

$$\int \delta n(\overrightarrow{r})d\overrightarrow{r} = 0. \tag{2.27}$$

We also know that the total energy of the system with external potential $v(\overrightarrow{r})$ can be written as

$$E[n(\overrightarrow{r})] = \int v(\overrightarrow{r})n(\overrightarrow{r})d\overrightarrow{r}d\overrightarrow{r'} + \frac{1}{2}\int\int \frac{n(\overrightarrow{r})n(\overrightarrow{r'})}{|\overrightarrow{r} - \overrightarrow{r'}|}d\overrightarrow{r}d\overrightarrow{r'} + T_s[n(\overrightarrow{r})] + E_{xc}[n(\overrightarrow{r})]. \tag{2.28}$$

Since the total energy of the system is a minimum and stationary in the ground-state, we have $\frac{\delta E}{\delta n(\overrightarrow{r})} = 0$.

Explicitly one writes

$$0 = \int \delta n(\overrightarrow{r})\left\{v(\overrightarrow{r}) + \int \frac{n(\overrightarrow{r'})}{|\overrightarrow{r} - \overrightarrow{r'}|}d\overrightarrow{r'} + \frac{\delta T_s[n]}{\delta n(\overrightarrow{r})} + \frac{\delta[E_{xc}(n)]}{\delta n(\overrightarrow{r})}\right\}d\overrightarrow{r}, \tag{2.29}$$

or in a compact form,

$$0 = \int \delta n(\overrightarrow{r})\left\{\varphi(\overrightarrow{r}) + \frac{\delta T_s[n]}{\delta n(\overrightarrow{r})} + \mu_{xc}[n(\overrightarrow{r})]\right\}d\overrightarrow{r}, \tag{2.30}$$

where

$$\varphi(\overrightarrow{r}) = v(\overrightarrow{r}) + \int \frac{n(\overrightarrow{r'})}{|\overrightarrow{r} - \overrightarrow{r'}|}d\overrightarrow{r'}, \tag{2.31}$$

and

$$\mu_{xc}(n) = \frac{\delta[n\epsilon_{xc}(n)]}{\delta n}. \tag{2.32}$$

The term $\frac{\delta[n\epsilon_{xc}(n)]}{\delta n}$ is the exchange and correlation contribution to the chemical potential of an uniform gas of density $n(\overrightarrow{r})$.

The equation(2.27) and (2.30) are exactly the same as the equation one can derive using [24] for non interacting electron system with effective potential
$v(\overrightarrow{r}) + \int \frac{n(\overrightarrow{r'})}{|\overrightarrow{r}-\overrightarrow{r'}|} d\overrightarrow{r'} + \mu_{xc}[n(\overrightarrow{r})]$.
Therefore, for a given $v(\overrightarrow{r})$ and $\mu_{xc}(\overrightarrow{r})$, one obtains $n(\overrightarrow{r})$ by solving a simple one-particle Schrödinger equation. Explicitly one writes

$$\left\{ \frac{-1}{2}\nabla^2 + v(\overrightarrow{r}) + \int \frac{n(\overrightarrow{r'})}{|\overrightarrow{r}-\overrightarrow{r'}|} d\overrightarrow{r'} + \mu_{xc}[n(\overrightarrow{r})] \right\} \psi_i(\overrightarrow{r}) = \epsilon_i \, \psi_i(\overrightarrow{r}), \tag{2.33}$$

where the electron density is defined as

$$n(r) = \sum_{i=1}^{N} |\psi_i(\overrightarrow{r})|^2, \tag{2.34}$$

where N is the total number of electrons.

The equation (2.33) to (2.34) needs to be solved self-consistently in order to find the ground-state density $n(\overrightarrow{r})$. One starts with an initial density n, and then calculates $\varphi(\overrightarrow{r}) = v(\overrightarrow{r}) + \int \frac{n(\overrightarrow{r'})}{|\overrightarrow{r}-\overrightarrow{r'}|} d\overrightarrow{r'}$. After that, $\mu_{xc}(n) = \frac{d[n\epsilon_{xc}(n)]}{dn}$ needs to be calculated. Now using $\varphi(\overrightarrow{r})$ and $\mu_{xc}(n)$ in equation (2.33) to obtain the single-particle wave-functions $\psi_i(\overrightarrow{r})$. Then the new density, $n(\overrightarrow{r}) = \sum_{i=1}^{N} |\psi_i(\overrightarrow{r})|^2$, can be calculated and used to obtain again $\varphi(\overrightarrow{r})$ and $\mu_{xc}(n)$. These new variables define the new Schrödinger equation, which in turn is used to find the new $\psi_i(\overrightarrow{r})$. The procedure is repeated until the changes in the density matrix between the consecutive iterations falls below a fixed tolerance limit. Now focus on the total energy of the system. This can be calculated by using the equation,

$$E = \sum_{1}^{N} \epsilon_i - \frac{1}{2} \int\int \frac{n(\overrightarrow{r})n(\overrightarrow{r'})}{|\overrightarrow{r}-\overrightarrow{r'}|} d\overrightarrow{r} d\overrightarrow{r'} + \int n(\overrightarrow{r}) \Big[\epsilon_{xc}[n(\overrightarrow{r})] - \mu_{xc}[n(\overrightarrow{r})] \Big] d\overrightarrow{r}. \tag{2.35}$$

The formula above is always exact but ϵ_{xc} is unknown.

2.3.1 Slow variation in density

The slow variation of density is characterized by the Wigner-Seitz radius r_s parameter. If the distance r over which the density changes is appreciable and the following condition

$\frac{r_s}{r} \ll 1$ holds, then we can assume that density is varying slowly. Then the exchange and correlation functional can be expanded locally, namely

$$E_{xc}[n] = \int \epsilon_{xc}(n)n(\overrightarrow{r})d\overrightarrow{r} + \int \epsilon_{xc}^{(2)}|\nabla n|^2 d\overrightarrow{r} + ..., \tag{2.36}$$

where $\epsilon_{xc}^{(2)}$ is the exchange and correlation portion of the second term in the energy expansion in powers of the gradient operator.

The single-particle kinetic energy in a slowly varying density regime can be written as

$$T_s[n] = \int \frac{3}{10}\left(3\pi^2 n\right)^{\frac{2}{3}} n \, d\overrightarrow{r} + \int t^{(2)}(n)|\nabla n|^2 d\overrightarrow{r} + ..., \tag{2.37}$$

where $t^{(2)}$ is the kinetic energy portion of the second term in the energy expansion in powers of the gradient operator. The total energy in the slowly varying density regime can be written as

$$E[n] = \int v(\overrightarrow{r})n(\overrightarrow{r})d\overrightarrow{r} + \frac{1}{2}\int \frac{n(\overrightarrow{r})n(\overrightarrow{r'})}{|\overrightarrow{r} - \overrightarrow{r'}|} d\overrightarrow{r} d\overrightarrow{r'} + \int g_0(n)d\overrightarrow{r} + \int g_2^{(2)}(n)|\nabla|^2 d\overrightarrow{r} + ..., \tag{2.38}$$

where

$$g_0(n) = \left[\frac{3}{10}\left(3\pi^2 n\right)^{\frac{2}{3}} + \epsilon_{xc}(n)\right]n, \tag{2.39}$$

and

$$g_2^{(2)}(n) = [\epsilon_x c^{(2)}(n) + t^{(2)}(n)]n. \tag{2.40}$$

In general, the exchange and correlation energy for the slowly varying density case should be calculated by using equation (2.36). The local density approximation of equation (2.26) does not consider the term in ∇^2, therefore the energy equation (2.38) has second order error.

2.3.2 Slater and Kohn-Sham exchange potential

The Slater exchange potential can be obtained through the Hartree-Fock exchange operator [25]. First one proceeds with the Hartree-Fock exchange operator in the form of an effective potential acting on k-th wave-function

$$v_{xk}(\overrightarrow{r}) = -\sum_{k'=1}^{N}\int \frac{\psi_k^*(\overrightarrow{r})\psi_{k'}^*(\overrightarrow{r'})\ \psi_{k'}(\overrightarrow{r})\psi_k(\overrightarrow{r'})}{|\overrightarrow{r}-\overrightarrow{r'}|\ \psi_k^*(\overrightarrow{r})\ \psi_k(\overrightarrow{r})}d\overrightarrow{r'}, \tag{2.41}$$

where $\overrightarrow{r}$ and $\overrightarrow{r'}$ include the spin coordinates and the summation runs over the spin coordinates as well. Next, one can assume that the wave-functions written above can be expanded by using plane waves, which results in

$$v_{xk} = -\frac{k_F(\overrightarrow{r})}{\pi}\left[1 + \frac{k_F^2(\overrightarrow{r}) - k^2}{2kk_F(\overrightarrow{r})}\log|\frac{k+k_F}{k-k_F}|\right], \tag{2.42}$$

where $k_F = \left[3\pi^2 n(\overrightarrow{r})\right]^{\frac{1}{3}}$. Finally by averaging v_{xk} on the occupied states k will result into a expression for the exchange potential, which results

$$v_x(\overrightarrow{r}) = -\frac{3}{2\pi}\left[3\pi^2 n(\overrightarrow{r})\right]^{\frac{1}{3}}. \tag{2.43}$$

In the Kohn-Sham procedure (neglecting correlation) the equivalent Slater's v_x is

$$\mu_x(\overrightarrow{r}) = -\frac{1}{\pi}\left[3\pi^2 n(\overrightarrow{r})\right]^{\frac{1}{3}}. \tag{2.44}$$

So, Slater's exchange $v_x(\overrightarrow{r})$ is $\frac{3}{2}$ times the Kohn-Sham $\mu_x(\overrightarrow{r})$ exchange.

If one evaluates Slater's exchange (equation 2.42) at $k = k_F$, i.e, if one computes effective exchange potential at the Fermi level, then it will be same as the Kohn-Sham exchange potential. This is physically understandable because density adjustment comes about by redistribution of electrons near the Fermi level.

2.3.3 High density regime

The high density regime is defined by the condition $\frac{r_s}{a_0} \ll 1$, where r_s is the Wigner-Seitz radius and a_0 is the Bohr radius. In this case, the entire exchange and correlation energy is very small compared to the kinetic energy by a order of $\frac{r_s}{a_0}$, and thus error in representing exchange and correlation in the Kohn-Sham scheme (exchange-correlation potential) is negligible. This is the case near the nuclear region of an atom. The Kohn-Sham scheme (exchange-correlation potential) is also very satisfactory in the low variation density regime where density varies very slowly. This is the case for the body of the atom and for continuous solids as well. The Kohn-Sham scheme (exchange-correlation potential) fails where the density variation is abrupt, such as surfaces and in the molecular bonding regime. These two cases, namely surface and molecular bonding, are situations where one can perform calculations by using non-local exchange and correlation functionals.

2.4 Atomic self-interaction correction (ASIC) method

Thomas and Fermi used the free-electron gas model and wrote the total energy of the system in-terms of the electron density [24]. In 1934, Fermi and Amaldi observed that in the one electron limit this model contains the self-interaction error [26]. The same error is not found in Hartree-Fock theory since the Coulomb interaction is cancelled by the exchange energy in each energy eigenstate. In Hartree-Fock theory the exchange energy is known completely. In the one-electron case this exchange term cancels the self-interaction Coulomb Hartree term making Hartree-Fock (H-F) theory self-interaction free. Although H-F theory is self-interaction free it does not account for correlation. However, in DFT, when one uses local or semi-local exchange and correlation functionals the self-interaction error does not get cancelled completely. A consequence of the self-interaction error is that the Kohn-Sham potential becomes too repulsive and leads to failures in predicting many fundamental properties of the system. For instance, negative charged ions, such as F^-, O^-, and H^-, are unstable within the LDA approximation. Furthermore, the LDA band-gap of transition metal oxides (such as MnO and NiO) is small compared to the measured band-gap. In 1981, Perdew and Zunger [27] proposed to remove the self-Hartree, self-exchange and correlation energy from each occupied orbital directly. Their self-interaction correction scheme leads to the functional (this is applied to the LDA):

$$E_{xc}^{SIC}[n^{\uparrow}, n^{\downarrow}] = E_{xc}^{LDA}[n^{\uparrow}, n^{\downarrow}] - \sum_{\alpha\sigma}^{occupied} \delta_{\alpha,\sigma}, \tag{2.45}$$

where

$$\delta_{\alpha,\sigma} = U[n_\alpha^\sigma] + E_{xc}^{LDA}[n_\alpha^\sigma, 0]. \tag{2.46}$$

In the above equation $U[n_\alpha^\sigma]$ is the self-Hartree potential energy for a one electron system of density n_α^σ and σ is the spin index. Similarly $E_{xc}^{LDA}[n_\alpha^\sigma, 0]$ is the self-XC (exchange and correlation) potential energy for all occupied Kohn-Sham (KS) orbitals from the LDA XC functional (the same argument is valid for other semi-local functionals). The Perdew and Zunger self-interaction correction (PZ-SIC) scheme is orbital dependent and thus one cannot define the kinetic energy functional independently from the XC one. As a consequence the KS orbitals no longer remain orthogonal and the KS equations are no longer invariant under unitary transformations of the occupied KS orbitals. This is a condition for the total energy to be a fundamental of the density. Various schemes have been developed to circumvent this problem. In order to make SIC more scalable many approximations have been introduced. One such approximation is to introduce SIC in the definition of pseudo-potentials [28]. In this approximation, atomic SIC has been removed from the free atom and the resulting electronic structure transferred into the norm-conserving pseudo-potential. This approximation holds because the transformation M, which relates canonical and localized orbital does not mix core and valence states [29]. Then the SIC contribution to the total energy can be separated into the core and valence states and to a first approximation the valence contribution can be neglected [29]. The benefit of this method is that translational invariance is regained and the complicated procedure to minimize M has been replaced by a pseudo-potential calculation. Further improvements to the pseudo-potential method has been done by Vogel and co-workers [30] and later by Filippetti and Spaldin [31]. This method still assume that SIC can be separated into core and valence contribution and valence SIC can be approximated using atomic-like contribution, also called atomic self-interaction correction (ASIC). This is an over-approximation because it implicitly assumes that the transformation M, which minimizes the SIC functional are atomic-like orbitals [32]. Vogel and co-workers [30] did not evaluate the valence SIC self-consistently while Filippetti and Spaldin [31] [33] assume a linear dependence of SIC over occupation. Further, Premmaraju $et al.$ [32] evaluated the valence SIC self-consistently by assuming that M transforming the localized orbital into canonical orbitals does not mix the core and valence states [29]. Also they assume that the core electrons are well localized into atomic-like wave-functions and can be efficiently described by norm-conserving pseudo-potentials. The two main approximations that have been taken into the ASIC approach are, first, localized states ϕ_m^σ are assumed to be atomic-like orbitals Φ_m^σ (ASIC orbital) and then SIC potential is approximated as

$$\sum_{\mathrm{m}} \mathrm{v}_{\mathrm{m}}^{\mathrm{SIC}}(\overrightarrow{r})\hat{\mathrm{P}}_{\mathrm{m}}^{\phi} \rightarrow \alpha \sum_{\mathrm{m}} \tilde{\mathrm{v}}_{\mathrm{m}}^{\sigma\mathrm{SIC}}(\overrightarrow{r})\hat{\mathrm{P}}_{\mathrm{m}}^{\Phi}, \tag{2.47}$$

where $\mathrm{v}_{\mathrm{m}}^{\mathrm{SIC}}(\overrightarrow{r}) = \mathrm{u}([\rho_{\mathrm{m}}]; \overrightarrow{r}) + \mathrm{v}_{\mathrm{xc}}^{\sigma\mathrm{LDA}}([\rho_{\mathrm{m}}^{\uparrow}, 0]; \overrightarrow{r})$, $\rho_{\mathrm{m}}^\sigma = |\Phi|^2$. $\hat{\mathrm{P}}_{\mathrm{m}}^{\Phi}$ is the projector

$$\hat{\mathrm{P}}_{\mathrm{m}}^{\phi}\psi_{\mathrm{n}}^{\sigma}(\overrightarrow{r}) = \phi_{\mathrm{m}}^{\sigma}(\overrightarrow{r}) \int \mathrm{d}^3\overrightarrow{r'}\,\psi_{\mathrm{n}}^{\sigma}(\overrightarrow{r'})\phi_{\mathrm{m}}^{\dagger\sigma}(\overrightarrow{r'}) = \phi_{\mathrm{m}}^{\sigma}(\overrightarrow{r})\langle\phi_{\mathrm{m}}^{\sigma}|\psi_{\mathrm{n}}^{\sigma}\rangle, \tag{2.48}$$

and is obtained by replacing ϕ_m with the ASIC orbital Φ_m, and α is a scaling parameter. The second approximation is to replace $\hat{\mathrm{P}}_{\mathrm{m}}^{\Phi}$ by its expectation value using

$$\hat{\mathrm{P}}_{\mathrm{m}}^{\Phi} \rightarrow \langle\hat{\mathrm{P}}_{\mathrm{m}}^{\Phi}\rangle = \sum_{\mathrm{m}} \mathrm{f}_{\mathrm{n}}^{\sigma}\langle\psi_{\mathrm{n}}^{\sigma}|\hat{\mathrm{P}}_{\mathrm{m}}^{\Phi}|\psi_{\mathrm{n}}^{\sigma}\rangle, \tag{2.49}$$

where $\mathrm{f}_{\mathrm{n}}^{\sigma}$ is the occupation number of the Kohn-Sham orbital ψ_n^σ. The final form of the ASIC potential then can be written as

$$v_{\mathrm{ASIC}}^{\sigma}(\overrightarrow{r}) = \alpha \sum_{m} \tilde{v}_{m}^{\sigma\mathrm{SIC}}(\overrightarrow{r})\mathrm{p}_{\mathrm{m}}^{\sigma}, \tag{2.50}$$

where α reflects the deviation of the actual ASIC projectors $|\Phi\rangle|\langle\Phi|$ from the localized orbitals defining the self-interaction (SI) corrected ground-state. One then expects $\alpha \sim 1$ for atomic-like charge density and $\alpha \sim 0$ for metals whose valence charge density resembles that of free-electron gas. The intermediate valence $\alpha \sim \frac{1}{2}$ is suitable for many mid-gap insulators. During implementation of ASIC the original formalism of Perdew-Zunger (PZ SIC) [27] scheme has been used, and the small non-orthogonality of KS orbitals has been ignored. A set of SI corrected atomic orbitals Φ_m has been obtained, which exactly solve the atomic SIC-LSDA problem. The atomic orbital Φ_m describing the valence electrons are then used to define the ASIC potential

$$\hat{v}_m^{\sigma\mathrm{SIC}} = u([\rho_m];\overrightarrow{r}) + v_{xc}^{\sigma\mathrm{LDA}}([\rho_m^{\uparrow},0];\overrightarrow{r}), \tag{2.51}$$

where $\rho_m^{\sigma} = |\Phi_m|^2$. ASIC is active only over occupied states and the gap only opens if occupied and unoccupied bands have a large difference in their projected atomic orbital content. Thus, ASIC is not effective for covalent materials where valence and conduction bands are made of the same atomic orbital content. However, ASIC is extremely effective for ionic compounds whose valence and conduction bands have very different atomic orbitals composition [32]. ASIC is variant under the unitary transformation of the orbitals used in construction the SIC potential. Thus, the SIC correction is likely to change as orbitals are rotated or transformed [32]. Also, in ASIC, there can be no variational principle over all possible unitary transformation of the atomic orbitals. The consequence of this is that the systems whose material properties are well described under LSDA (e.g. metal and small gap insulators) are now prone to be affected by ASIC correction [32]. In other words, ASIC correction does not necessarily vanish in these system. However, the ASIC scheme has significantly improved the band-gap of insulators and transition metals oxides [33].

2.5 Pseudo-potentials

The electronic structure of atoms can be divided into contributions coming from core and valence electrons. Most of the mechanical properties are driven by the chemical bonding between the atoms. In bonding, only the outermost electrons called valence electrons participate. The core electron energy state remains almost unperturbed during the bonding process. Since the core electrons are essentially unaffected by the chemical bonding they can be ignored. Therefore, in electronic calculations of materials we can use pseudo-potentials, which provide an exact potential on the valence electrons but do not describe the core region. The core electrons and the nucleus produce together an effective potential for the valence states and thus their effect can be replaced by an effective potential. This produces the exact potential in the valence region and it is non singular at the nuclear site. This pseudo-potential is not uniquely defined. There can be many types of pseudo-potentials, which can be used for the the same problem. The selection of one type of pseudo-potential over another is highly depend on the problem at hand. In order to make pseudo-potentials transferable (free from the effect of the surrounding environment of an atom in solids), one such form of pseudo-potentials is known as norm-conserving pseudo-potentials. Since the spherical coordinates system is orthogonal and the total wave-function $\psi(r)$ can be factorized into a radial, $\phi_l(r)$, and an angular part, $Y_{lm}(\theta, \phi)$, the Schrödinger equation can be treated efficiently in this coordinate system. The radial part of the Schrödinger equation for an atom in spherical coordinates can be written as

$$\left[\frac{-1}{2}\frac{d^2}{dr^2} + \frac{l(l+1)}{2r^2} + V(r)\right]\phi_l(r) = \epsilon\, \phi_l(r). \tag{2.52}$$

The most modern pseudo-potentials are norm-conserving pseudo-potentials. Norm-conserving pseudo-potentials are transferable from one environment (created in atomic environment) to another one (ions and solids). During this transformation, it is imperative that the transformation should be “exact, accurate and transferable” so that valence electron properties in ions, molecule and solids can be represent on a same footing as in an atom. There are certain requirements from a norm-conserving pseudo-potential as given by Hamann, Schluter and Chiang [34]:

(1)- The all-electron and pseudo-valence-eigenvalues should agree for the atoms under investigation.

(2)- The all-electron and pseudo-valence-wave-functions should agree beyond a certain chosen core radius, $\mathrm{R_c}$.

(3)-The logarithmic derivatives of the all-electron and pseudo-wave-function should be identical at R$_\mathrm{c}$.

(4)-Inside the core region of radius R$_\mathrm{c}$, the total integrated charge should be the same for the all-electron and the pseudo-wave-functions case (norm-conserving).

(5)- The first energy derivatives of the spatial derivatives of logarithmic wave-function of all-electron and pseudo-wave-function should agree at R$_\mathrm{c}$ for every eigenstate. This property of the pseudo-potential (PP) is also called transferability. The condition on the logarithmic derivatives of the pseudo-wave-function ensures that the pseudo-potential has the ability to reproduce the scattering properties of the true potential for a wide range of energies.

In particular the following condition should hold

$$-2\pi\left[\left(r\phi_i(r)\right)^2\frac{d}{d\epsilon}\left(\frac{d}{dr}\log[\phi_i(r)]\right)\right]_{R_c}=4\pi\int_0^{R_c}|\phi_i(r)|^2r^2dr, \qquad (2.53)$$

where $\phi_i(r)$ is the radial part of the wave-function satisfying equation (2.52). In other words, the pseudo-potential has the same scattering phase shift as the all-electron atom to first order in energy around a chosen ϵ_l.

(6)- There is one pseudo-potential for each angular momentum, namely

$$V^{ps}(r)=\sum_l V_l(r)|l\rangle\langle l|. \qquad (2.54)$$

2.5.1 Generation of the pseudo-potential

The generation of the pseudo-potential starts from calculating the all-electron atomic states. The pseudo-potential is generated for each state independently. The total potential is calculated self-consistently for a given electronic configuration of the atom and with a given approximation for the exchange and correlation functional. The next step is to separate the valence states and to generate the pseudo-potential $V_l(r)$ and the pseudo-orbitals $\psi_l^{PS}(r)=r\phi_l^{PS}(r)$. Here $\psi_l^{PS}(r)$ is the pseudo-orbital wave-function and $\phi_l^{PS}(r)$ is the radial part of the pseudo-orbital wave-function. The procedure for generating V_l^{PS}

is as follows:

First generate the total "screened" pseudo-potential, which is working on the valence electron of the atom. Then "un-screens" it by subtracting the Hartree and exchange-correlation potential of the valence pseudo-orbitals. This means writing

$$V_l(r) = V_{l,total} - V^{PS}_{Hxc}[n^{PS}(r)], \tag{2.55}$$

where $V^{PS}_{H,xc}[n^{PS}(r)] = V^{PS}_{Hartree}[n^{PS}(r)] + V^{PS}_{xc}[n^{PS}(r)]$, and $n^{PS}(r)$ is the valence atomic charge density, assumed to be spherical, $n^{PS}(r) = \frac{1}{4\pi}\sum_l f_l|\phi^{PS}_l(r)|^2$. The f_l is the occupancy of the state with angular momentum l. This $V_l(r)$ is called the bare ion pseudo-potential. It is useful to separate the pseudo-potential into a local (independent of the angular momentum l) and non-local (semi-local) term (dependent on the angular momentum l),

$$\hat{V}^{ps} = \hat{V}_{loc} + \hat{V_{SL}}, \tag{2.56}$$

$$\hat{V}_{loc} \equiv V_{loc}(r). \tag{2.57}$$

The semi-local part can be written as

$$\hat{V}_{SL} \equiv \sum_{lm} V_l(r)\delta(r - r')Y_{lm}(r)Y^{*}_{lm}(r'). \tag{2.58}$$

The local part is long ranged and behaves like $\left(\frac{-Z_{ion}e^2}{r}\right)$. There is no best "pseudo-potential" for a given element; there could be many "best" optimized, depending on the problem at hand. There are two competing factors that characterize a pseudo-potential, namely "accuracy" and "transferability". These two play a crucial role in the pseudo-potential selection. A bare ion pseudo-potential should be transferable from atom to any surrounding environment, namely molecules, gases or solid. A more accurate bare ion pseudo-potential is needed for greater transferability. A small cut-off radius $\mathrm{R_c}$ leads to more accurate but "hard" pseudo-potential through which the very high oscillatory nature of the wave-function near the nuclear region can be reproduced. A large cut-off radius $\mathrm{R_c}$ leads to a smooth, "soft" pseudo-potential. A soft pseudo-potential is not very transferable because most of the core part of the wave-function kink features are wiped out after selecting the large cut-off radius. Bachelet, Hamann and Schluter (BHS) [35] have constructed pseudo-potentials for all elements from H to Po, by using Gaussian basis function and tabulated the coefficients. These potentials are derived from an assumed form of potential after varying the parameters with conditions that the resulting wave-function will be able to give the required properties. This same approach has also been used by Vanderbilt [36]. Christiansen et al. [37] and Kerker [38] proposed a the simpler procedure for generating the pseudo-potential. The procedure goes as follows:

For each l, generate a pseudo-wave-function $\phi_l^{PS}(r)$, which can produce the required properties. This $\phi_l^{PS}(r)$ has the energy ϵ. Now invert the Schrödinger equation for a node-less wave-function $\phi_l^{PS}(r)$,

$$V_{l,total}(r) = \epsilon - \frac{\hbar^2}{2m_e}\left[\frac{l(l+1)}{2r^2} - \frac{\frac{d^2}{dr^2}\phi_l^{PS}(r)}{\phi_l^{PS}(r)}\right]. \tag{2.59}$$

On and outside the cut-off radius $\mathrm{R_c}$, the wave-function $\phi_l^{PS}(r)$ matches the all-electron wave-function perfectly. Inside the cut-off radius, $\phi_l^{PS}(r)$ is an analytic function. There are different types of analytic function in literature. Kerker chose $\phi_l^{PS}(r) = e^{p(r)}$ for $\mathrm{r} < \mathrm{R_c}$, where p(r) is a fourth-order polynomial in which the coefficients can be evaluated using the continuity of this functions, and its first and second derivatives at R_c and the norm-conserving condition inside the domain. Troullier and Martins [39] use the Kerker method but for more smoother pseudo-potentials. They used higher-order polynomials and matched higher-order derivatives of the wave-functions at R_c.

Chapter 3

Mathematical formalism of Quantum Transport

3.1 Introduction

Due to the recent advancements in lithographic techniques the miniaturisation of electronic devices at the nano-scale is now possible. These advancements lead to an increase in the package density of electronic devices such as transistors, an increase in the leakage current and an enhancement of the power dissipation at the nano-scale in small areas resulting in high power densities. Controlling the leakage current and the power dissipation are now significant challenges for the electronic industries. At the nano-scale level the leakage current and power dissipation can be modelled using quantum transport theory for the electrons and phonons. This is a many-body non-equilibrium statistical problem, where conducting electrons and background ions are in non-equilibrium during the transport. To deal with such a problem certain assumptions and approximations are required. The first attempt for such an electronic transport system was made by Landauer [40] for a two-contact system and then extended further by Büttiker [[41], [42]] for n contacts. In this chapter we will discuss the non-equilibrium Green's function (NEGF) formalism for coherent quantum transport, which resembles the same Landauer-Büttiker type equations. The Landauer-Büttiker approach approximates the closed system comprising battery, external contact, and nano-structure with an open system in which the external contacts have been replaced by infinite metallic leads. It is further assumed that adding or extracting the electrons from the lead into the nano-structure will not change the leads' statistical electronic distribution. In other words the electronic properties of the leads will remain unperturbed during the operation of the nano-device. The second assumption consists of a mean-field approximation for the many-body interacting problem. Within this approximation, one can describe the electronic structure of the full system in terms of a single-particle band or channel. The Landauer-Büttiker transport is a coherent transport, where the phase of the wave-function remains preserved. The nano-structure electronic states couple with the left and right-lead and create channels for coherent electronic transport.

If the nano-structure has M channels at the energy E and each channel has transmittance $T(E)$ then the total current from the left-lead to the right-lead can be written as

$$I_L = e\int_{-\infty}^{\infty} M(E)\, T(E)\, f_L(E) dE, \tag{3.1}$$

similarly the total current from the right-lead to the left-lead can be written as

$$I_R = e\int_{-\infty}^{\infty} M(E)\, T(E)\, f_R(E) dE. \tag{3.2}$$

Here $f_L(E)$ and $f_R(E)$ are the Fermi-Dirac distribution function of the left and the right-lead, respectively, and e is the charge of electron. At the energy E, there are two Bloch waves with wave-vector $+k$ and $-k$, which travel in the right and left direction respectively. An effective quantum current ($I = I_L - I_R$) can be further written by using equations (3.1) and (3.2) as

$$I = e\int_{-\infty}^{\infty} M(E)\, T(E)\, [f_L(E) - f_R(E)] dE. \tag{3.3}$$

3.2 Green's functions

The Green's function associated to the operator $\hat{L}$ is defined as

$$\hat{L}G = \delta(\boldsymbol{r} - \boldsymbol{r'})\delta(t - t'),$$

where $\delta(\boldsymbol{r} - \boldsymbol{r'})\ \delta(t - t')$ is the spatial and time dependent delta input given at position $\boldsymbol{r'}$ and time t'. In quantum mechanics the time-dependent wave-function can be found via the Schrödinger equation

$$i\hbar\frac{\partial\psi}{\partial t} = H\psi,$$

or

$$\left(i\hbar\frac{\partial}{\partial t} - H\right)\psi = 0, \tag{3.4}$$

where $\left(i\hbar\frac{\partial}{\partial t} - H\right)$ is a linear operator. Define $H = H_0 + V$, where H_0 is the Hamiltonian and V is an external perturbation independent of time. If we ignore the external perturbation V, then the Green's function associated with the Hamiltonian H_0 will be $G_0(t)$, where $G_0(t)$ satisfies

$$\left(i\hbar\frac{\partial}{\partial t} - H_0\right)G_0(t) = \delta(t - t'). \tag{3.5}$$

Let us now assume that the potential V is turned on at the time $t = t_0$, then we can define two Green's functions,

$$G^+(t) \quad \text{for} \quad t > t_0, \tag{3.6}$$

and

$$G^-(t) \quad \text{for} \quad t < t_0. \tag{3.7}$$

The function $G^+(t)$ is called the retarded Green's function, while $G^-(t)$ is called the advanced Green's function. In general, the solution of the differential equation

$$\left(i\hbar\frac{\partial}{\partial t} - H\right)G(t) = \delta(t). \tag{3.8}$$

is given by

$$G^+(t) = \frac{-i}{\hbar} e^{\frac{-iHt}{\hbar}}, \tag{3.9}$$

and

$$G^-(t) = \frac{i}{\hbar} e^{\frac{-iHt}{\hbar}}. \tag{3.10}$$

$G^+(t)$ and $G^-(t)$ are called perturbed-retard and perturbed-advanced Green's function respectively. Similarly for the unperturbed situation we have

$$G_0^+(t) = \frac{-i}{\hbar} e^{\frac{-iH_0 t}{\hbar}}, \tag{3.11}$$

and

$$G_0^-(t) = \frac{i}{\hbar} e^{\frac{-iH_0 t}{\hbar}}. \tag{3.12}$$

The Green's function can also be written in terms of the evolution operator which is defined as

$$U(t - t_0) = e^{\frac{-iH_0(t-t_0)}{\hbar}}. \tag{3.13}$$

Now the wave-function $|\psi(t)\rangle$ for $t > t_0$ can be written as

$$|\psi(t)\rangle = i\hbar G^+(t - t_0)|\psi(t_0)\rangle. \tag{3.14}$$

Similarly for $t < t_0$,

$$|\psi(t)\rangle = -i\hbar G^-(t - t_0)|\psi(t_0)\rangle. \tag{3.15}$$

The relationship between the unperturbed and the perturbed Green's function can be established as follows:

$$\left(i\hbar\frac{\partial}{\partial t} - H_0\right) G_0(t) = \mathbb{I}\delta(t),$$
$$\left(i\hbar\frac{\partial}{\partial t} - H_0\right) = \mathbb{I}\delta(t) G_0^{-1}(t).$$

For the perturbed system we have

$$\left(i\hbar\frac{\partial}{\partial t} - H\right) G(t) = \mathbb{I}\delta(t),$$

$$\left(i\hbar\frac{\partial}{\partial t} - H_0 - V\right) G(t) = \mathbb{I}\delta(t),$$

$$(\mathbb{I}\delta(t)G_0^{-1}(t) - V)G(t) = \mathbb{I}\delta(t).$$

By multiplying $G_0(t)$ on both sides we obtain

$$\mathbb{I}\delta(t)G(t) - G_0(t)VG(t) = \mathbb{I}\delta(t)G_0(t),$$

or

$$\mathbb{I}\delta(t)G(t) = G_0(t)VG(t) + \mathbb{I}\delta(t)G_0(t).$$

By integrating on both sides one finally obtains

$$G(t) = G_0(t) + \int_{t_0}^{t} dt_1 G(t_1)VG_0(t_0), \tag{3.16}$$

which is known as the Lippmann-Schwinger equation.

By expanding the Lippmann-Schwinger over the perturbation V we obtain

$$G(t-t_0) = G_0(t-t_0)+\int_{t_0}^{t} dt^{'} G_0(t-t')VG_0(t'-t_0)+\int_{t_0}^{t} dt' \int_{t_0}^{t'} dt'' G(t-t')VG_0(t'-t'')VG_0(t''-t_0) \tag{3.17}$$

Assuming that this series converges, then the effects of all scattering events can be written by defining a single term called self-energy, $\Sigma(t)$,

$$G(t-t_0) = G_0(t-t_0) + \int_{t_0}^{t} dt' \int_{t_0}^{t'} dt'' G(t-t')\Sigma(t'-t'')G_0(t''-t_0). \tag{3.18}$$

This is known as the Dyson equation.

If the perturbation is local in time then we can write

$$\Sigma(t'-t'') = V\delta(t'-t''). \tag{3.19}$$

3.3 Fourier transform of the Lippmann-Schwinger equation

One can rewrite the time dependent Lippmann-Schwinger equation in the frequency domain by using the Fourier transform of the retarded and advanced Green's functions.

$$G^+(E) = \int_{-\infty}^{\infty} dt\ e^{\frac{iEt}{\hbar}} G^+(t). \tag{3.20}$$

In order to calculate this integral, multiply the integrand by $e^{\frac{-\delta t}{\hbar}}$, where δ is a small shift in the energy eigenvalue along the complex-axis in the complex-plane.

$$G^{+}(E) = \int_{0}^{\infty} e^{i(Et+i\delta t)} G^{+}(t),$$

$$G^{+}(E) = \int_{0}^{\infty} e^{i(Et+i\delta t)} \frac{-i}{\hbar} e^{\frac{-iHt}{\hbar}},$$

$$G^{+}(E) = \frac{1}{E + i\delta - H}. \tag{3.21}$$

Similarly

$$G^{-}(E) = \int_{-\infty}^{\infty} dt \; e^{\frac{-iEt}{\hbar}} G^{-}(t). \tag{3.22}$$

In order to calculate this integral, multiply the integrand by $e^{\frac{\delta t}{\hbar}}$,

$$G^{-}(E) = \int_{0}^{\infty} e^{i(Et-i\delta t)} G^{-}(t),$$

$$G^{-}(E) = \int_{0}^{\infty} e^{i(Et-\delta t)} \frac{i}{\hbar} e^{\frac{-iHt}{\hbar}},$$

$$G^{-}(E) = \frac{1}{E - i\delta - H}. \tag{3.23}$$

Similarly one obtains

$$G_0^{+}(E) = \frac{1}{E + i\delta - H_0}, \tag{3.24}$$

and

$$G_0^{-}(E) = \frac{1}{E - i\delta - H_0}. \tag{3.25}$$

Dyson's equation can also be Fourier transformed and can be written as

$$G^{+}(E) = G_0^{+}(E) + G^{+}(E)\Sigma^{+}(E)G_0^{+}(E), \tag{3.26}$$

where $\Sigma^{+}(E)$ is the self-energy Fourier transformed $\Sigma^{+}(t', t'')$. The transformed Green's functions equation can be inverted to obtain $G^{+}(E)$, namely we can write

$$G^{+}(E) = \frac{G_0^{+}(E)}{1 - \Sigma^{+}(E)G_0^{+}(E)},$$

$$G^{+}(E) = \frac{1}{\left(G_0^{+}(E)\right)^{-1} - \Sigma^{+}(E)}.$$

By substituting $\left(G_0^+(E)\right)^{-1}$ with its expression in term of the Hamiltonian we obtain

$$G^+(E) = \frac{1}{E + i\delta - H_0 - \Sigma^+(E)}. \tag{3.27}$$

Similarly $G^-(E)$ can be written as

$$G^-(E) = \frac{1}{E - i\delta - H_0 - \Sigma^+(E)}. \tag{3.28}$$

3.4 Spectral representation of Green's function

In the spectral representation the Schrödinger equation can be written as

$$H|\psi_n\rangle = E_n S|\psi_n\rangle \tag{3.29}$$

where $|\psi_n\rangle$ is the wave-function and S is the overlap matrix. For orthonormal functions S is the identity matrix or in general $\sum_{n=1}^{N} |\psi_n\rangle\langle\psi_n|S = I$.

If we define

$$H = \sum_{n=1}^{N} E_n S|\psi_n\rangle\langle\psi_n|, \tag{3.30}$$

then the retarded Green's function (3.21) can be written as

$$G^+(E) = \sum_{n=1}^{N} \frac{1}{E + i\delta - E_n}|\psi_n\rangle\langle\psi_n|. \tag{3.31}$$

Let us now define

$$A(E) = i[G^+(E) - G^-(E)], \tag{3.32}$$

or

$$A(E) = i\left(\sum_{n=1}^{N} \frac{1}{E + i\delta - E_n}|\psi_n\rangle\langle\psi_n| - \sum_{n=1}^{N} \frac{1}{E - i\delta - E_n}|\psi_n\rangle\langle\psi_n|\right),$$

or

$$A(E) = 2\sum_{n=1}^{N} \frac{\delta}{(E - E_n)^2 + \delta^2}|\psi_n\rangle\langle\psi_n|.$$

By taking limit $\delta \to 0^+$ we obtain

$$A(E) = 2\pi \sum_{n=1}^{N} \delta(E - E_n)|\psi_n\rangle\langle\psi_n|. \tag{3.33}$$

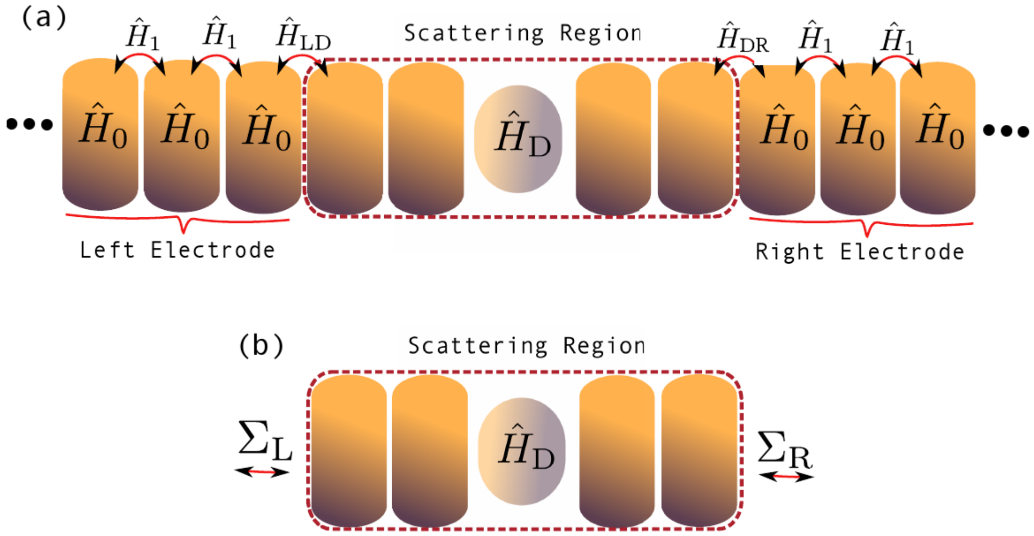

Figure 3.1: Schematic representation of the general quantum transport set-up used by the non-equilibrium Green's functions (NEGF) method. (a) The different regions of the device and its Hamiltonian are shown. (b) Left and right electrodes (leads) are replaced by their self energy matrix in transport set-up [5]

$A(E)$ is called the generalised density of states of the spectral function. The projected density of states (PDOS) can also be written by using the spectral function $A(E)$ as

$$\nu(E) = \frac{1}{2\pi}\mathrm{Tr}[A(E)S]. \tag{3.34}$$

In general, the density matrix is defined as

$$\rho = \sum_{n=1}^{N} f_n S|\psi_n\rangle\langle\psi_n|. \tag{3.35}$$

For bulk systems f_n is the Fermi-Dirac distribution function and then ρ can also be written as

$$\rho(r) = \frac{1}{2\pi}\int d(E)\, A(E)f(E). \tag{3.36}$$

Let us assume that we are allowed to partition a physical system into a left electrode, a scattering region and a right electrode (see in Figure 3.1). Let us also assume that the device can be defined by switching on the interaction between a scattering region and the left-hand side and right hand-side electrodes (leads) as depicted in figure 3.1. Let the Hamiltonian of the left-lead be H_L, the one of the right-lead be H_R, and the one of the device region be H_D. Then the Hamiltonians describing the coupling between the device and the leads are H_{LD} and H_{DR} respectively.

Now the Green's equation for the entire device $(ES - H)G = I$, can be written as

$$\begin{pmatrix} ES_L - H_L & ES_{LD} - H_{LD} & 0 \\ ES_{DL} - H_{DL} & ES_D - H_D & ES_{DR} - H_{DR} \\ 0 & ES_{RD} - H_{RD} & ES_R - H_R \end{pmatrix} \begin{pmatrix} G_L & G_{LD} & 0 \\ G_{DL} & G_D & G_{DR} \\ 0 & G_{RD} & G_R \end{pmatrix} = \begin{pmatrix} I & 0 & 0 \\ 0 & I & 0 \\ 0 & 0 & I \end{pmatrix}. \tag{3.37}$$

Note that the same notation is kept for the various blocks of the overlap matrix.

By expanding the matrix we obtain,

$$G_{LD}(E) = (ES_L - H_L)^{-1}(H_{LD} - ES_{LD})G_D(E), \tag{3.38}$$

and

$$G_{RD}(E) = (ES_R - H_R)^{-1}(H_{RD} - ES_{RD})G_D(E). \tag{3.39}$$

We can also write the surface Green's function of the left-lead and right-lead (electrode) as

$$g_l(E) = (ES_L - H_L)^{-1}, \tag{3.40}$$

and

$$g_r(E) = (ES_R - H_R)^{-1}. \tag{3.41}$$

By using $g_l(E)$ from equation (3.40) and $g_r(E)$ from equation (3.41) and by substituting in equations (3.38) and (3.39) we get

$$G_{LD}(E) = g_l(E)(H_{LD} - ES_{LD})G_D(E), \tag{3.42}$$

and

$$G_{RD}(E) = g_r(E)(H_{RD} - ES_{RD})G_D(E). \tag{3.43}$$

By using this definition we can introduce the two self-energies associated with the two leads

$$\Sigma_L(E) = (H_{LD} - ES_{LD})g_l(E)(H_{DL} - ES_{DL}), \tag{3.44}$$

and

$$\Sigma_R(E) = (H_{RD} - ES_{RD})g_r(E)(H_{DR} - ES_{DR}). \tag{3.45}$$

Finally the device Green's function can be written as

$$G_D = \frac{1}{ES_D - H_D - Re[\Sigma_L(E) + \Sigma_R(E)] - Im[\Sigma_L(E) + \Sigma_R(E)]}, \tag{3.46}$$

which satisfies the relation

$$\begin{aligned}[G_D^+(E)]^{-1} - [G_D^-(E)]^{-1} &= [\Sigma_L^+(E) - \Sigma_L^-(E)] + [\Sigma_R^+(E) - \Sigma_R^-(E)] \\ &= i[\Gamma_L(E) + \Gamma_R(E)] = i\Gamma(E). \end{aligned} \tag{3.47}$$

$\Gamma(E)$ in equation (3.47) is the electronic coupling between the leads (electrodes) and the scattering region. The imaginary part of the self-energy is associated with the decay of the solutions of Green's functions and can be interpreted as the rate at which the electrons are scattered in and out from the state of the isolated device. Thus, the electronic states of the device region get broadened due to the interaction with the electrodes, and usually their lifetime becomes finite.

3.5 Density matrix

When the system is out of equilibrium we can divide the contribution to the density matrix from those states which are in equilibrium with either the left and the right-lead (electrodes-reservoir),namely

$$\rho_D = \rho_{DL} + \rho_{DR}. \tag{3.48}$$

The individual parts of the density matrix ρ_{DL} and ρ_{DR} can be written as

$$\rho_{DL} = \int dE \sum_{n=1}^{N_L} p_{L,n}(E)\nu_{L,n}(E)|\psi_{L,n}^D\rangle\langle\psi_{L,n}^D|, \tag{3.49}$$

$$\rho_{DR} = \int dE \sum_{n=1}^{N_R} p_{R,n}(E)\nu_{R,n}(E)|\psi_{R,n}^D\rangle\langle\psi_{R,n}^D|, \tag{3.50}$$

where $p_{L,n}(E)$ and $p_{R,n}(E)$ are the left and right-lead occupation number for the channel $n(E)$, which lies between 0 and 1. N_L and N_R denote the total number of channels in the left and the right-lead, respectively. Finally, $\nu_{L,n}(E)$ and $\nu_{R,n}(E)$ are the projected density of states at the energy E of the left and right-lead, while $|\psi^D_{L,n}\rangle$ and $|\psi^D_{R,n}\rangle$ are the left and right-lead state vectors, which are extended over the device region. Let us assume that the left and right-lead are in local thermal equilibrium. Therefore $p_{L,n}(E)$ and $p_{R,n}(E)$ follow the Fermi-Dirac distribution, thus $p_{L,n}(E) = f_L(E)$ and $p_{R,n}(E) = f_R(E)$. A bias voltage eV_{sd} can be defined as the difference between the Fermi energy level of the left-lead and the right-lead. Generally, the equilibrium Fermi energy level, E_F, of the system is taken as the reference energy and defines the electrochemical potential of the left-lead $E_{F,L} = E_F + e\frac{V_{sd}}{2}$ and the electrochemical potential of the right-lead $E_{F,R} = E_F - e\frac{V_{sd}}{2}$. By using the spectral function, $A(E) = 2\pi \sum_{n=1}^{N} \delta(E - E_n)|\psi_n\rangle\langle\psi_n|$, and the Fermi-Dirac distribution for the left and right-lead we can write

$$\rho_{DL} = \frac{1}{2\pi} \int dE \, f_L A_{DL}, \tag{3.51}$$

and

$$\rho_{DR} = \frac{1}{2\pi} \int dE \, f_R A_{DR}. \tag{3.52}$$

We can now define the lesser Green's function for the scattering region $G^<_D$ [43] as

$$G^<_D = iG_D \Big[f_L(E)\Gamma_L + f_R(E)\Gamma_R \Big] G^\dagger_D. \tag{3.53}$$

Using equations (3.44), (3.45), (3.48), (3.49), (3.50) and (3.53) the density matrix ρ_D can be written as

$$\rho_D = \frac{1}{2\pi} \int dE \, G^<_D. \tag{3.54}$$

This is a central equation to the non-equilibrium Green's functions formalism, which allows one to obtain the charge density in the scattering region. The same procedure can be generalized for any number of leads (electrodes) attached to the scattering region. If we have N leads (electrodes) then $G_D^<$ can be written as

$$G_D^< = iG_D\left(\sum_{n=1}^{N} f_n\Gamma_n\right)G_D^\dagger, \tag{3.55}$$

where Γ_n is the self-energy of the n-th lead.

3.6 Wave-function of the partitioned system

The Schrödinger equation for a partitioned system in a matrix form can be written as

$$\begin{pmatrix} H_L & H_{LD} & 0 \\ H_{DL} & H_D & H_{DR} \\ 0 & H_{RD} & H_R \end{pmatrix}\begin{pmatrix} |\psi_L\rangle \\ |\psi_D\rangle \\ |\psi_R\rangle \end{pmatrix} = E\begin{pmatrix} S_L & S_{LD} & 0 \\ S_{DL} & S_D & S_{DR} \\ 0 & S_{RD} & S_R \end{pmatrix}\begin{pmatrix} |\psi_L\rangle \\ |\psi_D\rangle \\ |\psi_R\rangle \end{pmatrix}, \tag{3.56}$$

where

$$|\psi\rangle = \begin{pmatrix} |\psi_L\rangle \\ |\psi_D\rangle \\ |\psi_R\rangle \end{pmatrix} \tag{3.57}$$

is the partitioned state vector in the left-lead, device (scattering) region and right-lead. The isolated left-lead wave-function can be written as

$$|\phi_L\rangle = \begin{pmatrix} |\phi_L\rangle \\ 0 \\ 0 \end{pmatrix}. \tag{3.58}$$

Similarly for the isolated right-lead wave-function can be written as

$$|\phi_R\rangle = \begin{pmatrix} 0 \\ 0 \\ |\phi_R\rangle \end{pmatrix} \tag{3.59}$$

Scattering introduces an extra phase to the leads wave-functions and thus the new wave-function of the left and right-leads can be written as

$$|\psi_L\rangle = \begin{pmatrix} |\phi_L\rangle \\ 0 \\ 0 \end{pmatrix} + |\psi_L^\Delta\rangle, \tag{3.60}$$

and

$$|\psi_R\rangle = \begin{pmatrix} 0 \\ 0 \\ |\phi_R\rangle \end{pmatrix} + |\psi_R^{\Delta}\rangle. \tag{3.61}$$

Define now

$$K = H - (E + i\delta)S, \tag{3.62}$$

then $|\psi_L^{\Delta}\rangle$ satisfy the equation

$$(H - ES)|\psi_{L,n}^{\Delta}\rangle = \begin{pmatrix} 0 \\ -K_{DL}|\phi_{L,n}\rangle \\ 0 \end{pmatrix}. \tag{3.63}$$

From the definition of K it is clear that $K_D = K_D^{\dagger}$ and $K_{D\{L/R\}} = K_{\{L/R\}D}^{\dagger}$. Equation (3.63) has two sets of solutions. One is obtained after multiplication of the retarded Green's function from the left

$$|\psi_{L,n}^{\Delta+}\rangle = G^{+} \begin{pmatrix} 0 \\ -K_{DL}|\phi_{L,n}\rangle \\ 0 \end{pmatrix}, \tag{3.64}$$

whereas the other is obtained after the multiplication of the advanced Green's function from the left

$$|\psi_{L,n}^{\Delta-}\rangle = G^{-} \begin{pmatrix} 0 \\ K_{DL}|\phi_{L,n}\rangle \\ 0 \end{pmatrix}. \tag{3.65}$$

Equation (3.64) describes the electron flow from the left-lead into the scattering region, whereas equation (3.65) describes the electron flow from the scattering region into the left-lead at the energy level E_n. By using the matrix form of the Green's function, as mentioned in equation (3.37), the total wave-function originated in the left-lead can be written as

$$|\psi_{L,n}\rangle = \begin{pmatrix} I_L + g_l K_{LD} G_D K_{DL} \\ G_D K_{DL} \\ g_r K_{RD} G_D K_{DR} \end{pmatrix} |\phi_{L,n}\rangle. \tag{3.66}$$

Similarly the total wave-function originated in the right-lead can be written as

$$|\psi_{R,n}\rangle = \begin{pmatrix} g_r K_{LD} G_D K_{DR} \\ G_D K_{DR} \\ I_R + g_r K_{RD} G_D K_{DR} \end{pmatrix} |\phi_{R,n}\rangle. \tag{3.67}$$

3.7 Calculation of current per channel

The charge in the scattering region can be written by using the state vectors of the scattering region and the state vectors originating from the left and right-leads,

$$q_D = \langle\psi_L|S_{LD}|\psi_D\rangle + \langle\psi_D|S_D|\psi_D\rangle + \langle\psi_R|S_{RD}|\psi_D\rangle. \tag{3.68}$$

If we ignore the contribution coming from the overlap of the left-lead and the device regions $\langle\psi_L|S_{LD}|\psi_D\rangle$ and the right-lead and the device regions $\langle\psi_R|S_{RD}|\psi_D\rangle$, then the total charge in the device region can be written as

$$q_D = \langle\psi_D|S_D|\psi_D\rangle. \tag{3.69}$$

In the steady state the charge in the scattering region is stationary, so we can impose the condition

$$\frac{\partial q_D}{\partial t} = \frac{\partial}{\partial t}\langle\psi_D|S_D|\psi_D\rangle = 0. \tag{3.70}$$

By using the time dependent Schrödinger equation for the scattering region we can write

$$H|\psi_D\rangle_t = i\hbar S \frac{\partial}{\partial t}|\psi_D\rangle_t, \tag{3.71}$$

or

$$\frac{-i}{\hbar} E S_D|\psi_D\rangle = \frac{-i}{\hbar}(K_{DL}|\psi_L\rangle + H_D|\psi_D\rangle + K_{DR}|\psi_R\rangle). \tag{3.72}$$

Then the time derivative of the charge within the device region can be written as

$$\frac{\partial q_D}{\partial t} = \langle \frac{\partial}{\partial t}\psi_D|S_D|\psi_D\rangle + \langle \psi_D|S_D|\frac{\partial}{\partial t}\psi_D\rangle,$$

$$= \frac{i}{\hbar}(\langle\psi_L|K_{LD}|\psi_D\rangle - \langle\psi_D|K_{DL}|\psi_L\rangle) + \frac{i}{\hbar}(\langle\psi_R|K_{RD}|\psi_D\rangle - \langle\psi_D|K_{DR}|\psi_R\rangle). \tag{3.73}$$

This shows that the rate of change of charge in the device region is equal to the sum of the total current that flows from/to the left and right-leads into/out the device region. The current flowing from/to the left-lead into/out from the device region can be written as

$$I_L = \frac{i}{\hbar}(\langle\psi_L|K_{LD}|\psi_D\rangle - \langle\psi_D|K_{DL}|\psi_L\rangle). \tag{3.74}$$

Similarly the current flowing from /to the right-lead into/out from the device region can be written as

$$I_R = \frac{i}{\hbar}(\langle\psi_R|K_{RD}|\psi_D\rangle - \langle\psi_D|K_{DR}|\psi_R\rangle). \tag{3.75}$$

In the steady state

$$\frac{\partial q_D}{\partial t} = I_L + I_R = 0. \tag{3.76}$$

The total current from the left-lead is explicitly written as

$$I_L = \int dE \sum_{n=1}^{N_L} f_L(E)\nu_{L,n}(E) I^L_{L,n} + \int dE \sum_{n=1}^{N_R} f_R(E)\nu_{R,n}(E) I^L_{R,n}, \tag{3.77}$$

and the current which originate due to state vector in the left lead and travel in the scattering region can be written as

$$I^L_{L,n} = \frac{i}{\hbar}(\langle\psi^L_{L,n}|K_{LD}|\psi^D_{L,n}\rangle - \langle\psi^D_{L,n}|K_{DL}|\psi^L_{L,n}\rangle). \tag{3.78}$$

Similarly the current which originate due to the state vector from right lead and travelling in to the scattering region by carrying through the left lead state vector $I^L_{R,n}$ can be written as

$$I^L_{R,n} = \frac{i}{\hbar}(\langle\psi^L_{R,n}|K_{LD}|\psi^D_{R,n}\rangle - \langle\psi^D_{R,n}|K_{DL}|\psi^L_{R,n}\rangle). \tag{3.79}$$

Further we can write

$$I^L_{L,n} = \frac{1}{\hbar}\langle\phi_{L,n}|K_{LD}G^-_D\Gamma_R G^+_D K_{DL}|\phi_{L,n}\rangle, \tag{3.80}$$

and

$$I^L_{R,n} = -\frac{1}{\hbar}\langle\phi_{R,n}|K_{LD}G^-_D\Gamma_L G^+_D K_{DR}|\phi_{R,n}\rangle. \tag{3.81}$$

Next we can write

$$I^L_L = \int dE\, \sum_{n=1}^{N_L} f_L(E)\nu_{L,n}(E)I^L_{L,n}, \tag{3.82}$$

and

$$I^L_R = \int dE\, \sum_{n=1}^{N_R} f_R(E)\nu_{R,n}(E)I^L_{R,n}, \tag{3.83}$$

where $\nu_{R,n}(E)$ and $\nu_{L,n}(E)$ are the projected density of states of the right and the left-lead at the energy E. We can write total current $I_L = I^L_L + I^L_R$. By using equation (3.78), (3.80), and (3.82) we obtain I^L_L as

$$I^L_L = \frac{1}{\hbar}\int dE\, f_L(E)\sum_{n=1}^{N_L}\nu_{L,n}(E)(\langle\phi_{L,n}|K_{LD}G^-_D\Gamma_R G^+_D K_{DL}|\phi_L, n\rangle),$$

$$I^L_L = \frac{1}{\hbar}\int dE\, f_L(E)\mathrm{Tr}[K_{DL}\sum_{n=1}^{N_L}(\nu_{L,n}(E)|\phi_{L,n}\rangle\langle\phi_{L,n}|)K_{LD}G^-_D\Gamma_R G^+_D]. \tag{3.84}$$

If we now consider the spectral representation of the left-hand side lead,

$$A_L(E) = 2\pi\sum_{n=1}^{N_L}\nu_{L,n}(E)|\phi_{L,n}\rangle\langle\phi_{l,n}|, \tag{3.85}$$

we can then write the current from the left-hand side lead as

$$I^L_L = \frac{1}{\hbar}\int dE\, f_L(E)\mathrm{Tr}[\Gamma_L G^-_D\Gamma_R G^+_D]. \tag{3.86}$$

Similarly the total current from the left lead into the scattering region carried by the states originate in the right lead can be written as

$$I^L_R = -\frac{1}{\hbar}\int dE\, f_R(E)\mathrm{Tr}[\Gamma_L G^-_D\Gamma_R G^+_D], \tag{3.87}$$

where the transmission T is defined as

$$T(E) = \mathrm{Tr}[\Gamma_L G^-_D\Gamma_R G^+_D]. \tag{3.88}$$

By using the equations (3.86), (3.87) and (3.88) one can write the total net current that can flow from the left-lead into the right-lead via the scattering region as

$$I = I_L = \frac{1}{\hbar}\int dE\, T(E)[f_L(E) - f_R(E)]. \tag{3.89}$$

In order to obtain the electric current we need to multiply I by $2e$, where 2 is for spin and e is the electron charge.

$$I = I_L = \frac{2e}{\hbar} \int dE\, T(E)[f_L(E) - f_R(E)]. \tag{3.90}$$

For collinear spin polarized systems the spin up channel transmission is independent from the spin down channel one (two spin fluid model). In this case the total transmission is written as

$$T(E) = T^{\uparrow}(E) + T^{\downarrow}(E). \tag{3.91}$$

For a spin polarised system equation (3.83) can be explicitly written as

$$T^{\sigma}(E) = \mathrm{Tr}[\Gamma_L^{\sigma} G_D^{-\sigma} \Gamma_R^{\sigma} G_D^{+\sigma}], \tag{3.92}$$

where $\sigma =\uparrow, \downarrow$. On a same footing the total current should be written as

$$I = I^{\uparrow} + I^{\downarrow}. \tag{3.93}$$

Chapter 4

Magnetic Tunnel junctions and their general working principle

4.1 Introduction

A magnetic tunnel junction consists of two ferromagnetic electrodes and an insulating spacer sandwiched between them. One ferromagnet's magnetic moment is fixed along a certain direction and is known as the reference layer. The other ferromagnet's magnetic moment is free to follow an external magnetic field and is called the free layer. When both ferromagnetic magnetic moments are parallel to each other then the junction offers the minimum resistance for a current flowing perpendicular to the layer stack. The state of the device is called the low resistance state. In binary terms, this state represents a "0" state. In contrast when the electrodes magnetic moments are anti-parallel to each other, then the junction offers the maximum resistance to a perpendicular current. The device state is then known as the high resistance state. In binary terms, this state represents the "1" state. The tunnelling magneto-resistance magnitude is defined through the TMR ratio $\left(\frac{R_{AP}-R_P}{R_P}\right) \times 100$, where R_{AP} is the resistance of the junction when the ferromagnet magnetic moments are anti-parallel to each other. In contrast R_P is the resistance of the junction when both ferromagnet magnetic moments are parallel to each other.

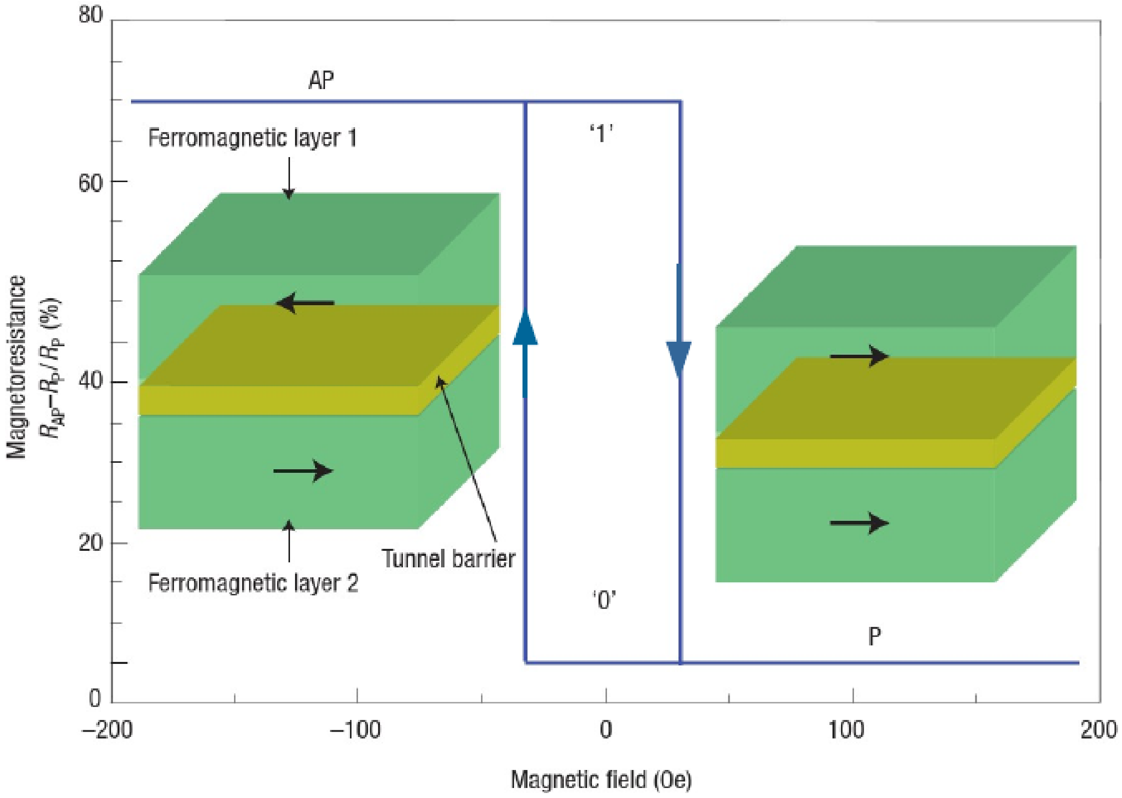

Figure 4.1: Schematic of a tunnelling magneto-resistance magnetic tunnel junction device structure. The blue line describe the magnetic response (hysteresis) of the junction [1]

4.2 TMR Theory

4.2.1 Julliere model

In 1975, Julliere [11] fabricated a Fe-Ge-Co junction and measured its current voltage characteristic at 4.2 K for both the parallel and anti-parallel configurations of the ferromagnetic electrodes. He measured a TMR of 14%. Julliere explained the experimentally measured tunnelling current by using as a material quantity the density of states of the ferromagnetic electrodes. In his hypothesis Julliere proposed that the conductance (the inverse of the resistance) is directly proportional to the density of states of the left electrode and the right electrode. In particular, the conductance $G^{\sigma\sigma'}$ for the (σ, σ') arrangement of the electrodes ($\sigma =\uparrow, \downarrow$) can be written as

$$G^{\uparrow\uparrow} \propto N_L^{\uparrow} N_R^{\uparrow}, \tag{4.1}$$

$$G^{\uparrow\downarrow} \propto N_L^{\uparrow} N_R^{\downarrow}, \tag{4.2}$$

$$G^{\downarrow\uparrow} \propto N_L^{\downarrow} N_R^{\uparrow}, \tag{4.3}$$

$$G^{\downarrow\downarrow} \propto N_L^{\downarrow} N_R^{\downarrow}, \tag{4.4}$$

where N_α^σ is the density of state for spin σ of the α-th electrode. The total conductance equation in parallel configuration can be then written as

$$G_P = G^{\uparrow\uparrow} + G^{\downarrow\downarrow}, \tag{4.5}$$

whereas in anti-parallel configuration

$$G_{AP} = G^{\uparrow\downarrow} + G^{\downarrow\uparrow}. \tag{4.6}$$

Equation (4.5) and (4.6) are in-line with the two current channel model proposed by N.F.Mott in late 1930 [8]. The TMR can then be written in terms of the spin conductances

$$TMR = \frac{G_P - G_{AP}}{G_{AP}}, \tag{4.7}$$

using equation (4.1), (4.2), (4.3), (4.4),(4.5) and (4.6) in (4.7), we obtain

$$TMR = \frac{N_L^{\uparrow} N_R^{\uparrow} + N_L^{\downarrow} N_R^{\downarrow} - N_L^{\uparrow} N_R^{\downarrow} - N_L^{\downarrow} N_R^{\uparrow}}{N_L^{\uparrow} N_R^{\downarrow} + N_L^{\downarrow} N_R^{\uparrow}}. \tag{4.8}$$

The polarized density of states of the left electrodes can be written as

$$P_L = \frac{N_L^{\uparrow} - N_L^{\downarrow}}{N_L^{\uparrow} + N_L^{\downarrow}} = \frac{\Delta N_L}{N_L}, \tag{4.9}$$

similarly for the right electrodes

$$P_R = \frac{N_R^{\uparrow} - N_R^{\downarrow}}{N_R^{\uparrow} + N_R^{\downarrow}} = \frac{\Delta N_R}{N_R}. \tag{4.10}$$

Using P_L and P_R in equation (4.8) the TMR equation can be written as

$$TMR = \frac{\Delta N_L \Delta N_R}{\frac{1}{2}(N_L N_R - \Delta N_L \Delta N_R)} = \frac{2P_L P_R}{(1 - P_L P_R)}. \tag{4.11}$$

Due to its simple mathematical structure equation (4.11) is mostly used in explaining the experimental results. However, it has some draw-backs which are as follows: Although the final TMR ratio equation has been written in term of the polarized density of states of the left and right electrodes, one should not strictly interpret it as the spin polarized density of states at Fermi level.

(1) It is a well known fact that Fe and Co have predominantly minority density of states at the Fermi level, but in tunnelling experiments the majority electrons carry the tunnelling current.

(2) In this model the barrier material does not appear in the final TMR equation, i.e. it is irrelevant. However it has been observed that the TMR sign changes when the barrier is changed, while keeping the same ferromagnet electrodes [44].

(3) The TMR in amorphous and epitaxial-grown barrier materials are very different in magnitude, although Julliere's model deals with both amorphous and epitaxial-grown barrier material on the same footing and predicts the same TMR.

In conclusion, we can say that Julliere's model is more suitable for TMR comparison, if the junction barrier material is the same (mostly amorphous) and ferromagnetic electrodes are different. As such it provides only a rough guideline and it should be improved.

4.2.2 Landauer-Büttiker theory

Landauer-Büttiker theory [40] is applicable to coherent transport where the phase of the wave-function of the tunnelling electrons is conserved. In the Landauer-Büttiker approach the transport is totally coherent and there is no inelastic scattering during the tunnelling transport in the insulating region. For this reason the phase of the wave-function is traceable before, during and after a tunnelling event. In the Landauer-Büttiker formalism the current can be written as

$$I = \frac{e}{h}\sum_{\mathbf{k}_{||}}\int \frac{\partial E(\mathbf{k})}{\partial k_z} dk_z f(\mu_1)\sum_{\mathbf{k}^{'}} T^{++}(\mathbf{k},\mathbf{k}^{'}). \tag{4.12}$$

In this expression the partial derivatives of the energy with respect to the wave-vector k_z will give the electron velocity in the z-direction (z is the chosen direction of transport). $\mathbf{K}_{||}(\mathrm{k_x},\mathrm{k_y})$ is the transverse components (perpendicular to the transport direction) of the wave-vector and made from $(\mathrm{k_x},\mathrm{k_y})$ components of the Bloch wave. In equation (4.12) $T^{++}(\mathbf{k},\mathbf{k}^{'})$ is the transmission probability of an electron from a wave-vector with wave-vector k to one with wave-vector $k^{'}$. For positive current

$$I^{+} = \frac{e}{h}\int_0^{\mu_1}\sum_{\mathbf{k}_{||},\mathbf{k}^{'}_{||}} T^{++}(\mathbf{k},\mathbf{k}^{'}), \tag{4.13}$$

similarly for negative current

$$I^{-} = \frac{e}{h}\int_0^{\mu_2}\sum_{\mathbf{k}_{||},\mathbf{k}^{'}_{||}} T^{--}(\mathbf{k},\mathbf{k}^{'}). \tag{4.14}$$

$T^{++}(\mathbf{k},\mathbf{k'})$ in Eq. (4.13) and $T^{--}(\mathbf{k},\mathbf{k'})$ in Eq. (4.14) are the transmission coefficient of the scattering matrix. Time reversal symmetry imposes that $T^{++} = T^{--}$. If one imposes a small difference in the chemical potential of the two electrodes we can write the net current as

$$I^{+} - I^{-} = \frac{e^2}{h}\sum_{\mathbf{k}_{||},\mathbf{k}^{'}_{||}} T^{++}(\mathbf{k}_{||},\mathbf{k}^{'}_{||})\frac{\mu_1-\mu_2}{e}. \tag{4.15}$$

In this expression $\frac{\mu_1-\mu_2}{e}$ is equal to the voltage difference across the sample. The conductance $G = \frac{I}{V}$, is thus given by

$$G = \frac{I}{V} = \frac{e^2}{h} \sum_{\mathbf{k}_{||},\mathbf{k}'_{||}} [T^{++}(\mathbf{k}_{||}, \mathbf{k}'_{||})]_{E_F}, \tag{4.16}$$

where the transmission coefficient is evaluated at the Fermi level, E_F. Since the two-dimensional periodicity is retained in the plane perpendicular to the current flow direction the parallel component of the wave-vector is conserved. Therefore, we can further simplify the final equation for the conductance as

$$G = \frac{I}{V} = \frac{e^2}{h} \sum_{\mathbf{k}_{||}} [T(\mathbf{k}_{||})]_{E_F}. \tag{4.17}$$

By summing over the $\mathrm{k}_{||}$ vectors the total number of conduction channels is found.

4.2.3 Simple barrier model

In a simple barrier model a free electron with energy E hits a potential barrier at height V and width, d, where $E < V$. Since a free electron behaves like a plane-wave, it can tunnel across the barrier. The plane-wave $\mathbf{k}$ vector has three components, namely k_x, k_y and k_z. Let us assume that the z-direction is the tunnelling direction then k_x, k_y vectors become transverse to the tunnelling direction. The electron wave-function with non-zero k_x, k_y components will travel a further distance at the same potential energy barrier height than the zero k_x, k_y component. In the case of zero k_x, k_y components the electron only tunnel perpendicular to the potential energy barrier height and covers the shortest distance. In the case of non-zero k_x, k_y components the electron travel oblique to the barrier because of the non-zero component of the electron velocity in the x and y directions. Thus, it has to travel a further distance than for the vanishing k_x, k_y case. The electron wave-function amplitude in the tunnelling region is proportional to $\exp^{(-\kappa.\mathrm{d})}$ where $\kappa^2 = \left(\frac{2m}{\hbar^2}\right)(V - E) + k_{||}^2$. Here, $k_{||}^2 = k_x^2 + k_y^2$. As a consequence, the electron with high κ will have its wave-function amplitude decay faster in the barrier region than those

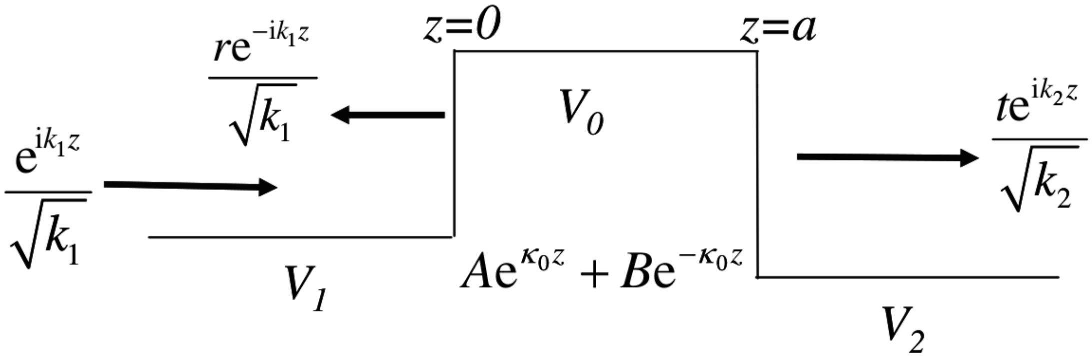

Figure 4.2: Wave-function scheme for a simple tunnel barrier model [2]

with lower κ. In the non-zero k_x, k_y case, κ will be larger than in the zero k_x, k_y case and thus the amplitude of the wave-function will be smaller than in the non-zero case. Since the tunnelling probability is directly proportional to $\exp^{(-2\kappa.\mathrm{d})}$, the tunnelling probability is smaller for high κ. Also, in the non-zero $k_{||}(k_x, k_y)$ case the electron travels a distance of $d\left(1+\frac{k_{||}^2}{k_z^2}\right)^{\frac{1}{2}}$ to cross the energy barrier, whereas in the case of zero $k_{||}(k_x, k_y)$ it will travel a distance, d, usually a short tunnelling distance. The transmission equation for the probability for the oblique case is $\mathrm{T_0}\ \exp^{\left[-2\mathrm{k_z d}\left(1+\frac{\mathrm{k}_{||}^2}{\mathrm{k}_z^2}\right)^{\frac{1}{2}}\right]}$, whereas for the non-oblique (perpendicular to the barrier height) case is $\mathrm{T_0}\ \exp^{(-2\kappa_z \mathrm{d})}$. Since the transmission probability in the oblique case is smaller than in the non-oblique one, the transmission probability is smaller in the non-zero $k_{||}(k_x, k_y)$ case. Finally, the transmission in the non-oblique case can be written as

$$T = |t|^2 = \frac{8\kappa_0^2\ \kappa_1\ \kappa_2}{(\kappa_1^2+\kappa_0^2)\ (\kappa_2^2+\kappa_0^2)\ \cosh(2\kappa_0 d) + 4\kappa_0^2\ \kappa_1\ \kappa_2 - (\kappa_1^2-\kappa_0^2)\ (\kappa_2^2-\kappa_0^2)}, \tag{4.18}$$

where $\kappa_1^2 = \frac{2m(E-V_1)}{\hbar^2} - k_{||}^2$, $\kappa_2 = \frac{2m(E-V_2)}{\hbar^2} - k_{||}^2$, and $k_0^2 = \frac{2m(V_0-E)}{\hbar^2} + k_{||}^2$.

If the barrier width, d, is thick enough such that $\exp^{(2\kappa_0 \mathrm{d})} \gg 1$, then the above expression can be simplified further into

$$\begin{aligned} T &= \frac{16\kappa_0^2 \ \kappa_1 \ \kappa_2 \ \exp^{(-2\kappa_0 \mathrm{d})}}{(\kappa_1^2+\kappa_0^2) \ (\kappa_2^2+\kappa_0^2)}, \\ &= \frac{4\kappa_0 \ \kappa_1}{\kappa_1^2+\kappa_0^2} \ \frac{4\kappa_0 \ \kappa_2}{\kappa_2^2+\kappa_0^2} \ \exp^{(-2\kappa_0 \mathrm{d})}, \\ &= T_1 \ T_2 \ \exp^{(-2\kappa_0 \mathrm{d})}, \end{aligned} \tag{4.19}$$

where $T_1 = \frac{4\kappa_0 \ \kappa_1}{\kappa_1^2+\kappa_0^2}$, and $T_2 = \frac{4\kappa_0 \ \kappa_2}{\kappa_2^2+\kappa_0^2}$. The final equation (4.19) factorises T into three terms. The first T_1 term is the transmission probability of an electron when it is incident to the finite potential energy barrier from the left electrode and penetrates as an evanescent state into the barrier region. Similarly T_2 is the transmission probability of an electron incident to the finite potential energy barrier from the right electrode and proceeds as an evanescent state into the barrier region. Then the third term $\exp^{(-2\kappa_0 \mathrm{d})}$ is the tunnelling probability for the electron wave-function, i.e. it is the probability that the electron will be able to cross the potential energy barrier. After writing the total transmission in terms of $\mathrm{T} = \mathrm{T}_1 \ \mathrm{T}_2 \ \exp^{(-2\kappa_0 \mathrm{d})}$, Julliere's model can be re-derived. However, in this form the total spin polarization current is defined in terms of the transmission probability of electrons from the electrodes into the potential energy barrier region at the interface for each value of $k_{||}$. Note that this requires the generalization of the Landauer-Büttiker formalism to spin-dependent transmission (see in Figures 4.3, 4.4 and 4.5). The polarization of each electrode can then be defined in terms of the transmission probabilities as

$$P_1 = \frac{T_1^{\uparrow} - T_1^{\downarrow}}{T_1^{\uparrow} + T_1^{\downarrow}}, \tag{4.20}$$

$$P_2 = \frac{T_2^{\uparrow} - T_2^{\downarrow}}{T_2^{\uparrow} + T_2^{\downarrow}}. \tag{4.21}$$

Then the TMR can be written as

$$\mathrm{TMR} = \frac{2P_1P_2}{1-P_1P_2}. \tag{4.22}$$

Although the simple barrier model is good for explaining the tunnelling across the energy barrier within the Wentzel-Kramers-Brillouin (WKB) approximation, it is not sufficient

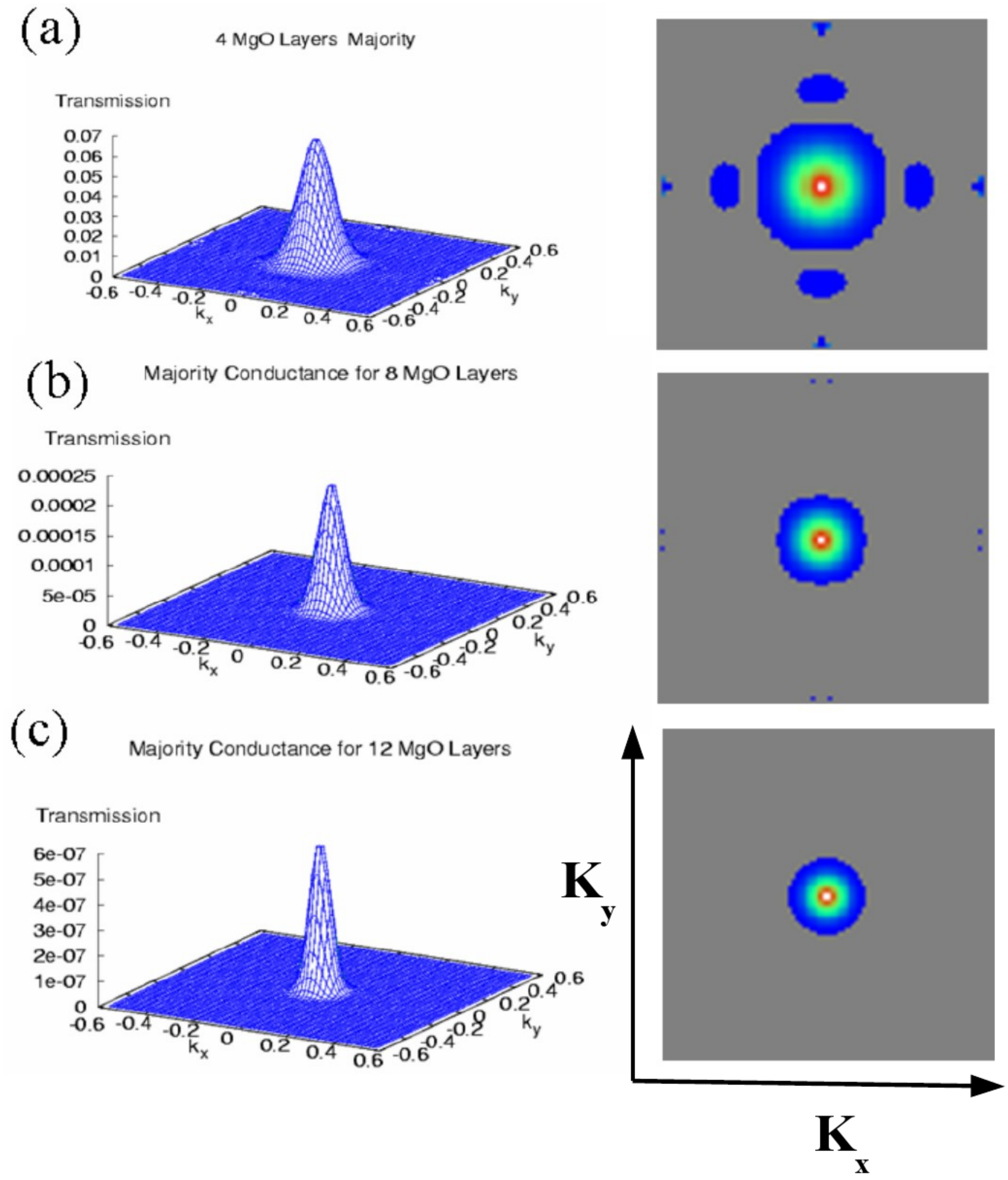

Figure 4.3: Majority spin channel conductance with parallel alignments of the magnetic moment of the iron electrodes. The left hand side is the transmission conductance with different thickness of MgO layers ((a) 4 layers of MgO, (b) 8 layers of MgO, and (c) 12 layers of MgO), whereas the right hand side is the contour plot of the same data. [2]

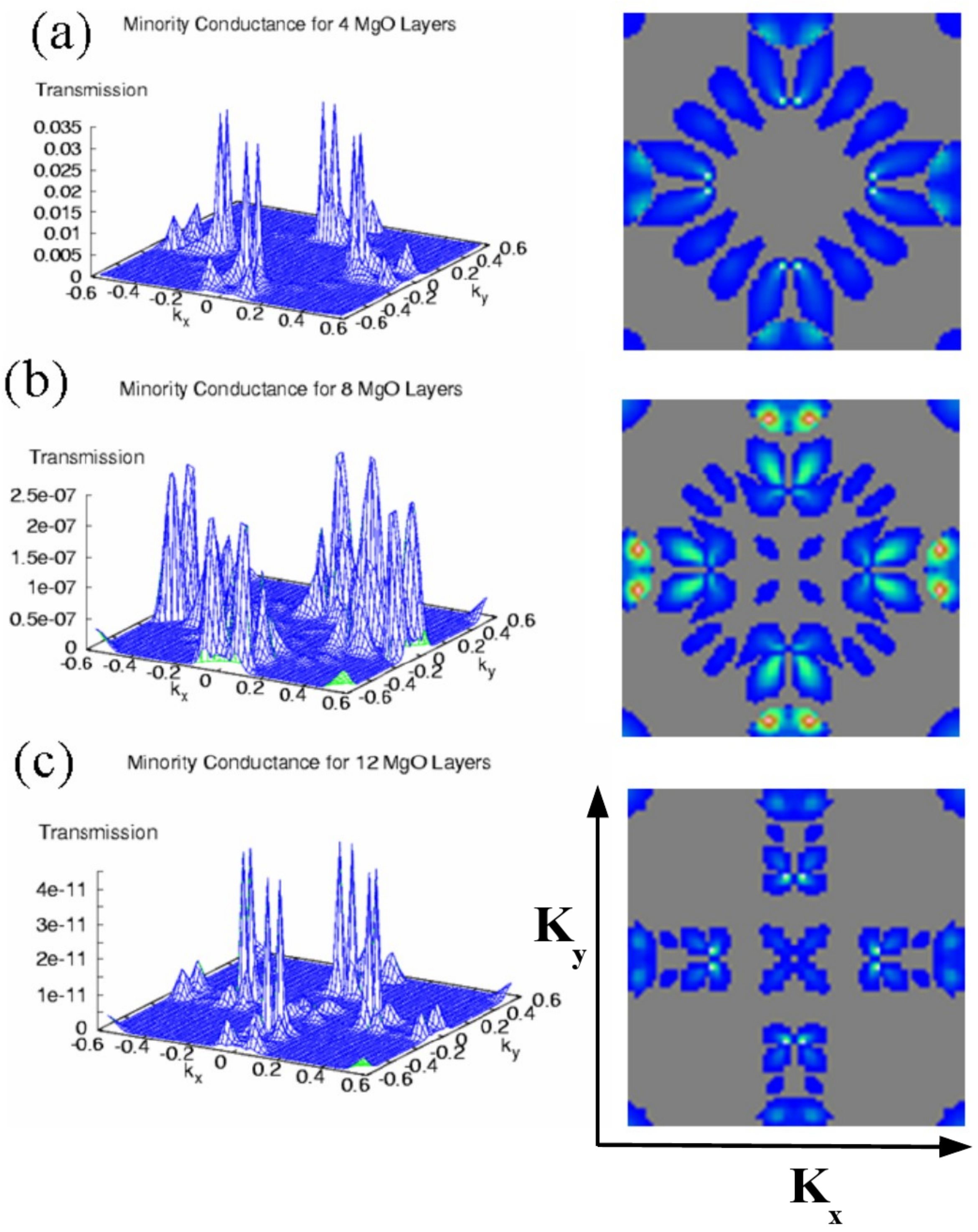

Figure 4.4: Minority spin channel conductance with parallel alignments of the magnetic moment of the iron electrodes. The left hand side is the transmission conductance with different thickness of MgO layers ((a) 4 layers of MgO, (b) 8 layers of MgO, and (c) 12 layers of MgO), whereas the right hand side is the contour plot of the same data. [2]

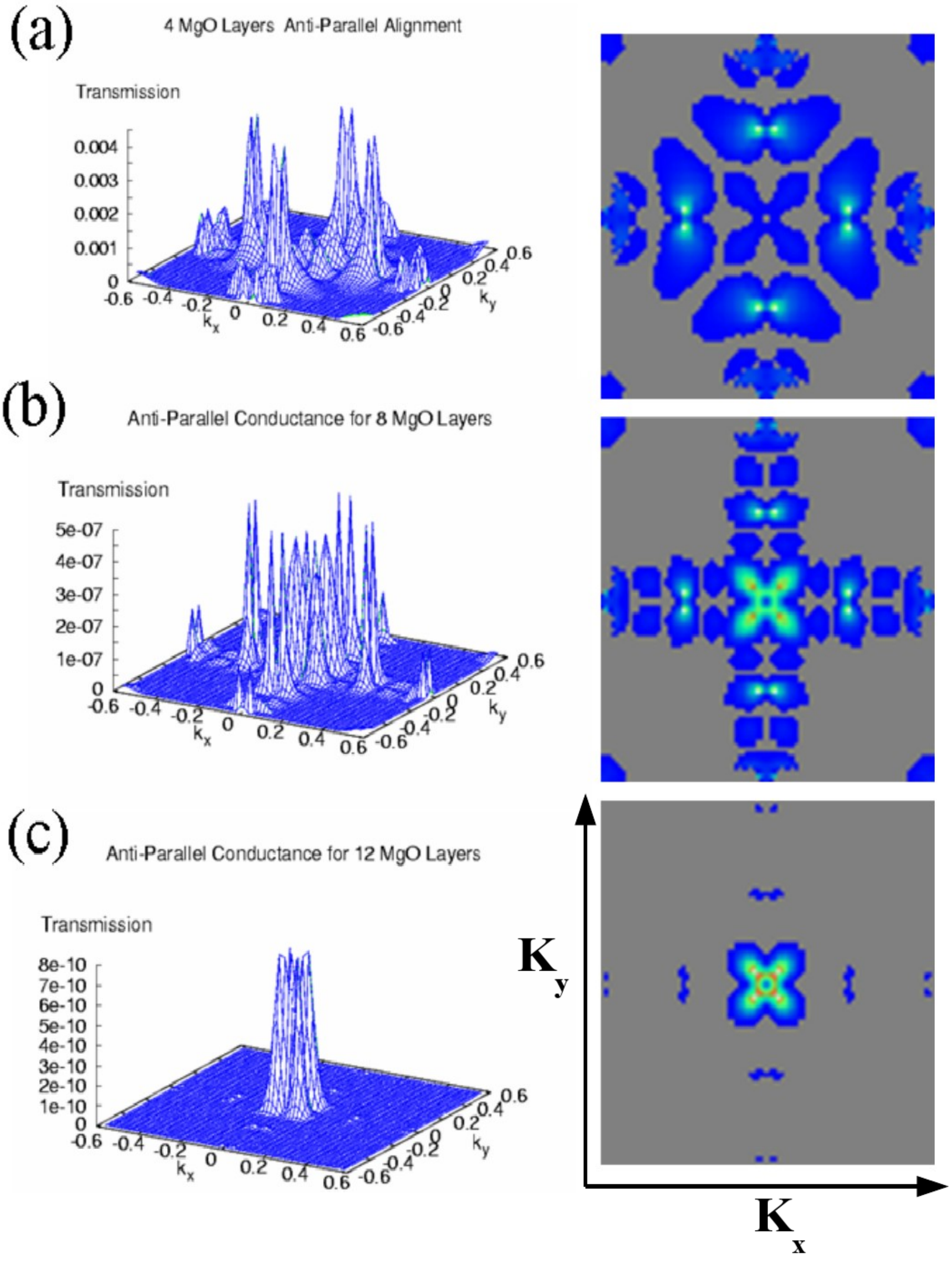

Figure 4.5: Conductance with anti-parallel alignments of the magnetic moment of the iron electrodes. The left hand side is the transmission conductance with different thickness of MgO layers ((a) 4 layers of MgO, (b) 8 layers of MgO, and (c) 12 layers of MgO), whereas the right hand side is the contour plot of the same data. [2]

to explain the symmetry filtering of the Bloch states by the insulating material. The simple barrier model in fact treats all the electrons with the same energy on equal footing ignoring the effect of the angular momentum of the wave-function (non-spherical Fermi surface). If the electron wave-function has a high oscillation frequency in the transverse plane perpendicular to the transport direction then the tunnelling probability of such Bloch states is lower. Also, the k_z component of the wave-vector in the barrier region should be written in such a way that it includes the curvature effect of wave-function from the transverse plane. The wave-function which has a high oscillation in the transverse plane (perpendicular to the transport direction) adds an extra component to k_z. The final equation including a curvature effect in k_z can be written as

$$k_z = \sqrt{\left(\frac{2m}{\hbar^2}\right)(V - E) + k_{\parallel}^2 - \frac{\langle\phi|(\nabla_{\parallel}^2)|\phi\rangle}{\langle\phi|\phi\rangle}}, \tag{4.23}$$

where $\nabla_{\parallel}^2 = \frac{\partial}{\partial x^2} + \frac{\partial}{\partial y^2}$. In expression (4.23), $|\phi\rangle$ is the transverse component $\phi(x, y)$ of the wave-function $\psi(x, y, z)$ of the electron. The last term in this expression includes the transverse curvature effect. A negative sign in the curvature term will become positive after one more negative sign contribution coming from the second partial derivatives of the transverse wave-function $\phi(x, y)$ is taken into account. From the curvature expression it is clear that if the wave-function has large oscillations in the transverse direction then k_z will be large and thus the tunnelling probability will be low. So, Bloch states presenting symmetry as p_x, p_y, $d_{x^2-y^2}$ and d_{xy} have high oscillation in the transverse plane (assuming the tunnelling is along the z-direction), therefore, these Bloch states have low tunnelling probability.

4.3 Classification of the Bloch states

Bloch states can be classified according to their orbital angular momentum symmetry. One has to look along the z-direction at the Bloch states and analyse their projection over the $x - y$ plane. Different possible Bloch states symmetries with respect to rotations

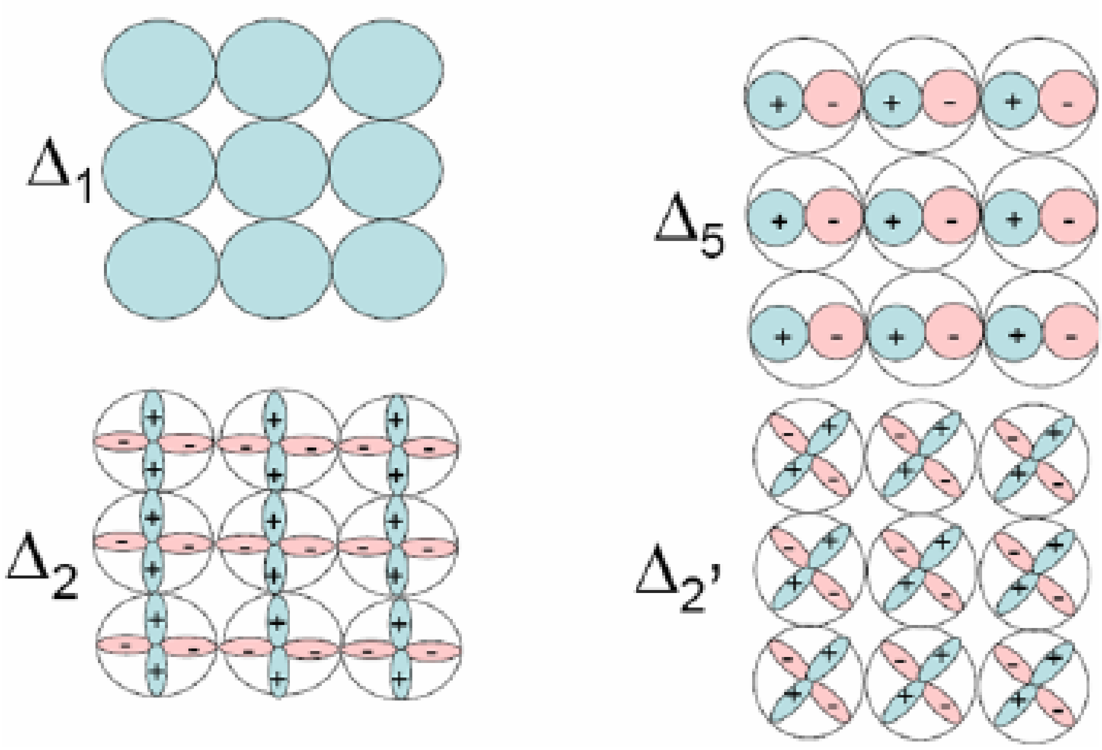

Figure 4.6: Classification of the Bloch states symmetry according to their projection on to the $x - y$ plane. One has to consider their symmetry with respect to rotations about the z axis [2].

about the z-axis are shown in Figure 4.6. Bloch states of s, p_z and d_{z^2} symmetry are called Δ_1-like states. Bloch states transforming as p_x, p_y, d_{xz} and d_{yz} symmetry are called Δ_5-state. The Bloch state with d_{xy} symmetry is called $\Delta_{2'}$. Finally a Bloch state of $d_{x^2-y^2}$ symmetry is called Δ_2.

4.4 2D (k_x, k_y) plot in first Brillouin zone

A (k_x, k_y) plot is a way to visualize the decay rate of the Bloch state z-amplitude over the plane perpendicular to the transport direction (z-direction). A material is periodic in 3D and the electrons travel with v_z velocity which is parallel to the k_z component of the wave-vector. The other components (k_x and k_y) are transverse to the transport direction. Since the material is periodic, its electronic properties will also have the periodicity. Therefore, plotting the decay rates of the wave-function over the first Brillouin zone is enough to conclude transport characteristics of the material. The magnitude of the decay rate of the wave-function of the electrons in the first Brillouin zone will tell us which portion of the Brillouin zone supports most of the current. If the decay rate has a minimum at some $\mathrm{k}_{\|}$-value the tunnelling probability will be high. If some-point has a high decay rate, it means that the tunnelling probability at that-point will be low. Each (k_x, k_y)-point will be associated to a certain magnitude of decay rate and will support a certain amount in total transmission. For example, in the case of ZnO, the minimum decay rate is 1.14 ($\mathring{A}^{-1}$) and the maximum decay rate is 2.83 ($\mathring{A}^{-1}$) (see in Fig.4.7). The minimum decay rate occurs at the Γ-point in the first 2D hexagonal Brillouin zone. Other-points (except the Γ-point) in the 2D hexagonal Brillouin zone have a higher decay rate. This suggests that in the case of ZnO the states close to the Γ-point will contribute to the maximum transmission, whereas the contribution of other k-points will be a small. The color mapping in the (k_x, k_y) plot varies linearly from the lowest decay rate coordinate-points to the highest decay rate coordinate-points.

4.5 Complex-band analysis

The (k_x, k_y) plot tells us about the transport supporting k-points in the first Brillouin zone. However, it does not tell us about the symmetry of the Bloch wave-function which

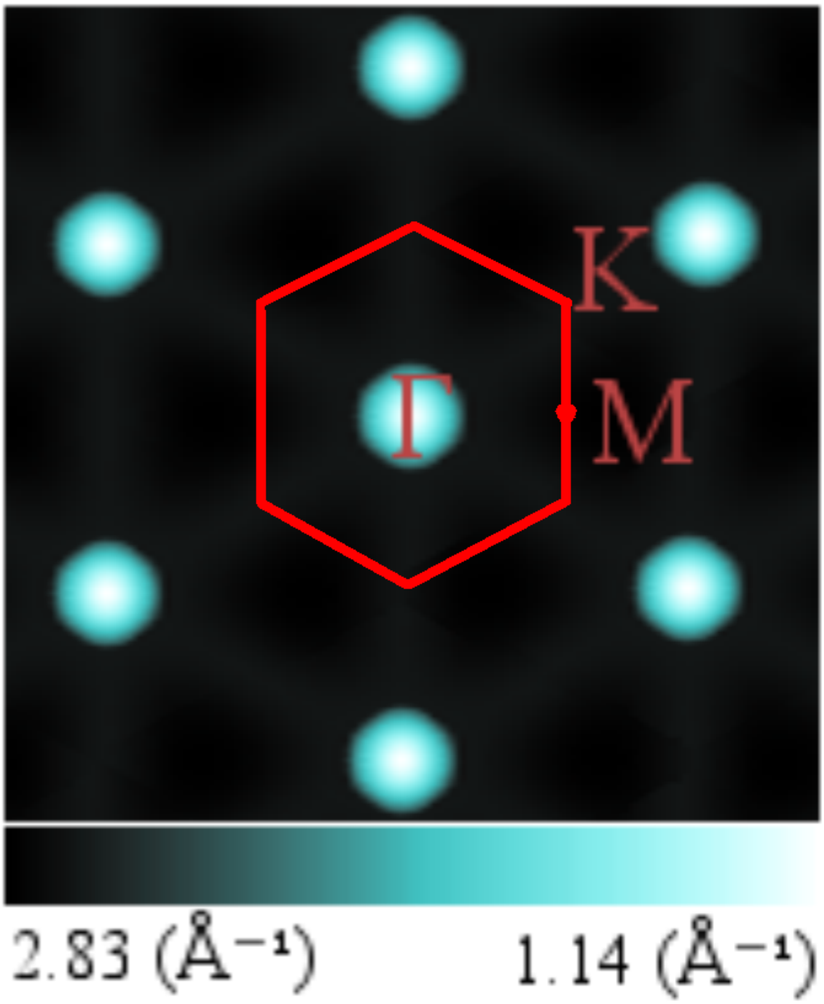

Figure 4.7: 2D (k_x, k_y) decay plot of Bloch wave-function of ZnO with the first Bruillion zone highlighted. ZnO has minimum Bloch wave-function decay rate of $1.14\AA^{-1}$ at the Γ-point and maximum of $2.83\AA^{-1}$ at the other-point in first 2D hexagonal Brillouin zone. Color in (k_x, k_y) plot varies linearly from lowest decay rate to the highest decay rate supporting coordinate-points. The transmission has been evaluated with the Fermi energy level of the ZnO is in the middle of the band-gap $(\mathrm{E} - \mathrm{E_F} = 0)$

have a minimum decay rate at the transport supporting points. As such, in order to determine which symmetry the Bloch wave-function will have at the minimum decay rate, complex wave-function analysis is required at each transport supporting-point. In a complex-band analysis we vary the energy of the incident Bloch wave-function electron and allow it to tunnel. During the tunnelling through the energy barrier the amplitude of the incident electron wave-function decays with different rates. At each energy level one allows the electron to tunnel and calculates its amplitude decay rate. By doing this for each energy level and calculating the amplitude decay rate one obtains the complex-band of a material. The most important feature in this analysis is that it gives the symmetry of the Bloch state, which has a minimum decay rate when it tunnels across the band-gap of a material. For example, in the case of ZnO, it is the Δ_1 symmetry whose wave-function amplitude has minimum decay rate at the Γ-point (see in Fig.4.8). The valence band of ZnO is made mainly from oxygen p orbitals ($p_x,\ p_y,\ p_z$), whereas the conduction band is made mainly from the zinc s orbital. Since s and p_z orbital have Δ_1 symmetry, ZnO filters Δ_1 symmetry of the Bloch state at Γ-point in the first Brillouin zone.

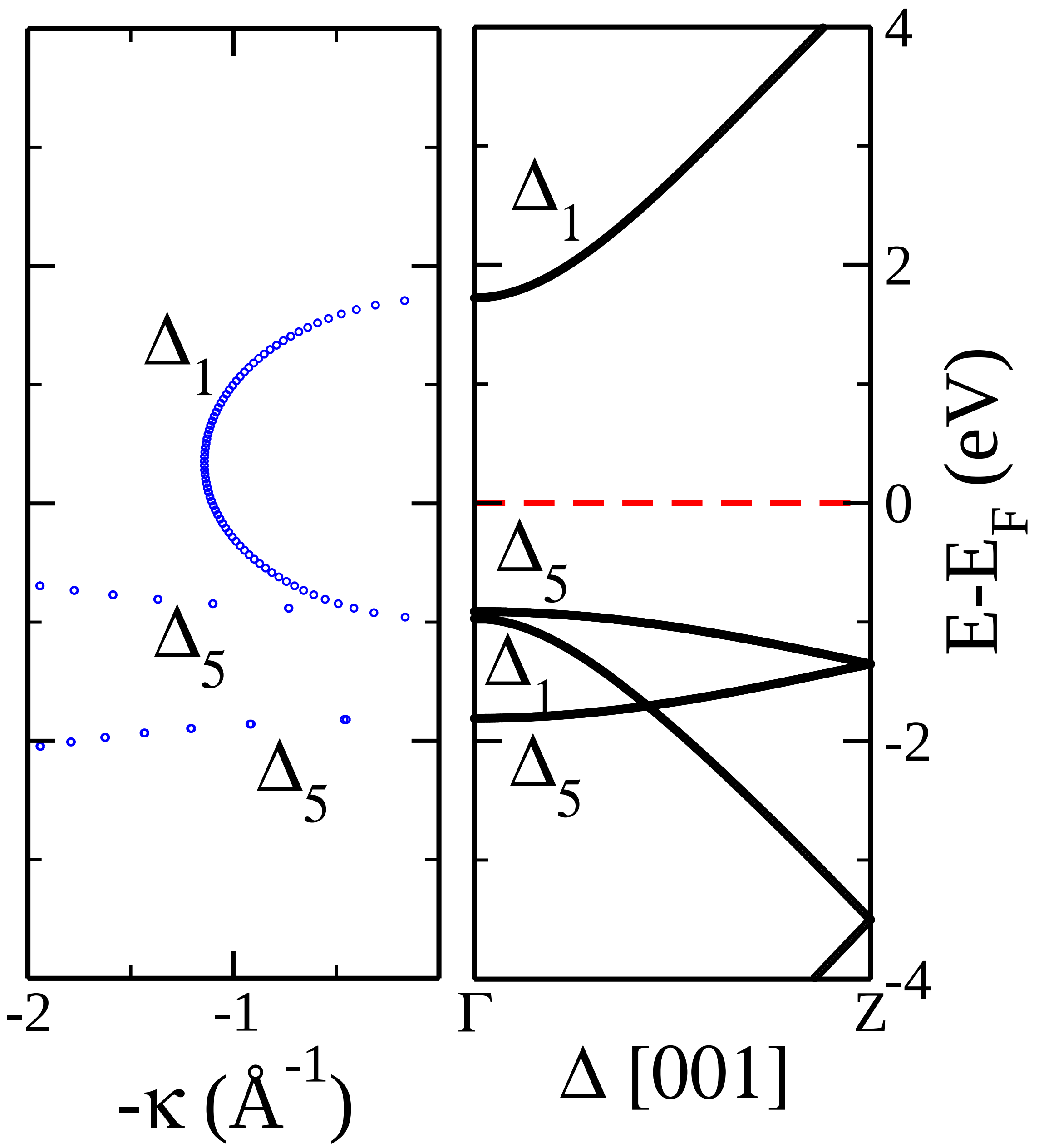

Figure 4.8: Real (right-hand side panel) and complex-band (left-hand side panel) structures of ZnO. Complex-band analysis suggests that the Δ_1 symmetry of Bloch state has a minimum decay rate κ during transport along [001] direction. The red dotted horizontal line at $\mathrm{E_f} = 0$ denotes the Fermi energy level of ZnO.

The work done in this thesis is based upon the symmetry filtering effect is caused by the insulators [3]. This effect says that an insulator allows certain a symmetry of the Bloch state to tunnel more easily than the others. The selection of the symmetry is a property of coherent transport in insulating materials. It couples strongly with only a certain symmetry of the Bloch states and allows it to tunnel smoothly while the other symmetries of the Bloch states faces maximum resistance and most of the time they are attenuated (transmission probabilities are zeros) before reaching the other side of the tunnel barrier. This whole argument needs to be tested on various footings, that whether tunnelling across the commensurate ferromagnet-insulator-ferromagnet junctions are governed by the symmetry filtering arguments or it is governed by the conventional Wentzel-Kramers-Brillouin (WKB)-types tunnelling, in which barrier does not favour one symmetry of the Bloch states over the others if they all have the same energy and phase. The one way to test this claim is by changing the width of the insulators in the MTJs and plot the current versus insulating barrier width (W). If the symmetry filtering arguments are correct then the transmission current must decay exponentially as the insulating barrier width increases. Second, the slope of the logarithm resistance versus insulating barrier width must be equal to twice the decay of the wave-vector κ, because in a perfect tunnelling case one can write the device resistance as $\mathrm{R} = \mathrm{R}_0 \exp^{(2\kappa \mathrm{d})}$, where d is the width of the insulating barrier. If we take the logarithm on both sides of this equation then one can further write, $\ln(\mathrm{R}) = \ln(\mathrm{R}_0) + 2\kappa d$. Which means logarithmic of resistance versus the width of the insulating barriers must be a straight line with the slope equal to 2κ (see for example Fe|MgO|Fe MTJs in Figure 4.12). So the slope of the transmission data from Smeagol calculations after varying the width of the insulators must be matched to the experiments (see for example Fe|MgO|Fe MTJs in Figure 4.12). Third, the theory of the Smeagol code is purely based on the Butler [3], and Mathon [15], works in which they have used tight binding concepts to capture the tunnelling phenomenon. The Smeagol code must be evaluated/investigated on two footings: first, the energy of the coherent tunnelling wave-function does not change during the tunnelling across any insulating barriers, so this condition must be remain preserved in the Smeagol code. Second, the phase of the coherent tunnelling wave-function also remains conserved during the tunnelling across the insulating barrier, and thus this condition should also remain preserved in the Smeagol code. The tight binding concept uses a hopping mechanism for the transport of electrons from one site to another. Typically, in this process energy and phase of the transported electrons wave-functions changes. If the energy of the hopping electron wave-function changes then this violates the fundamentals of the coherent tunnelling rules which states that the energy and the phase of the wave-function in coherent tunnelling process can not change in any circumstances. So a thorough investigation is required on the tight binding concept itself in that whether it will able to capture the coherent tunnelling process or not. Also, the TMR of the MTJs with varying insulating barrier width (here $HfO_2, SiO_2, ZnO, GaN, AlN$) should follow the same trend as a real fabricated, commensurate interface Fe|MgO|Fe based MTJ (see in Figure 4.11). If the tunnelling in the commensurate interface based MTJs happens via symmetry filtering then the trends in the TMR as a function of insulating barrier width must be the same as the Fe|MgO|Fe based MTJs and if this is the case then it will validate the claims even at qualitative levels. Calculation done by Butler [2] with different width of the MgO insulating layers during parallel alignment of the ferromagnetic electrodes are shown in figure 4.10. We took the transmission data from the calculations of Butler [2] and plotted the transmission versus the width of the MgO layers on the logarithmic scale. We found the negative linear trends between the transmission and the MgO barrier width which seems support the quantum mechanical tunnelling symmetry filtering line of arguments in the Fe|MgO|Fe junctions (see in Figure 4.9). We hope that this will work and provide the same trends in our HfO_2, SiO_2, ZnO, GaN, and AlN based MTJs as well. Still a full investigation is required

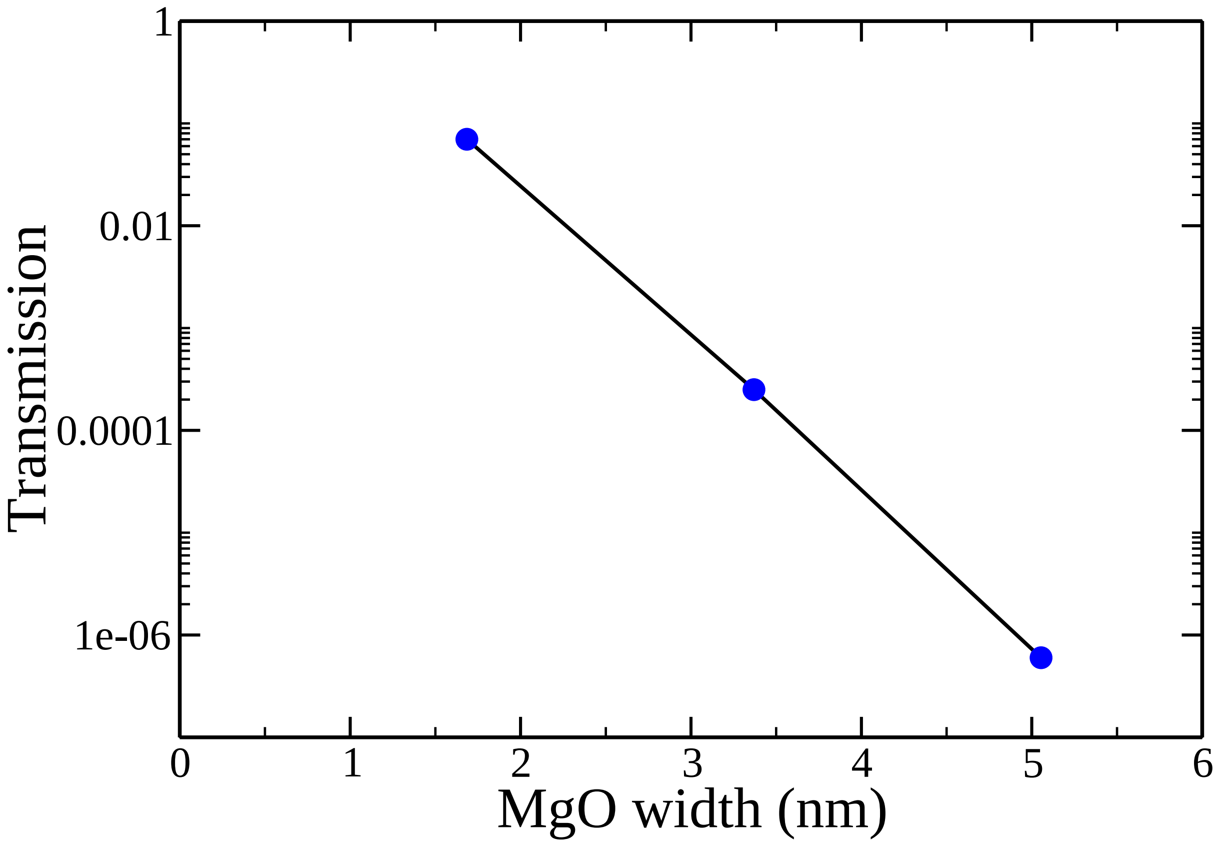

Figure 4.9: Majority spin channel conductance with parallel alignment of the iron electrodes magnetic moment in Fe|MgO|Fe MTJs. The blue points represents the transmission in Fe|MgO|Fe magnetic tunnel junctions with 4, 8, and 12 layers of MgO width. The MgO lattice parameter has taken 4.212Å [2].

for the validation of the slope of the calculated transmitted graph with experiments (see in Figure 4.12), and also to investigate the Smeagol simulation code to make sure that the two fundamental concepts for coherent tunnellings is preserved: the conservation of energy, and the conservation of the phase of the tunnelling wave-functions.

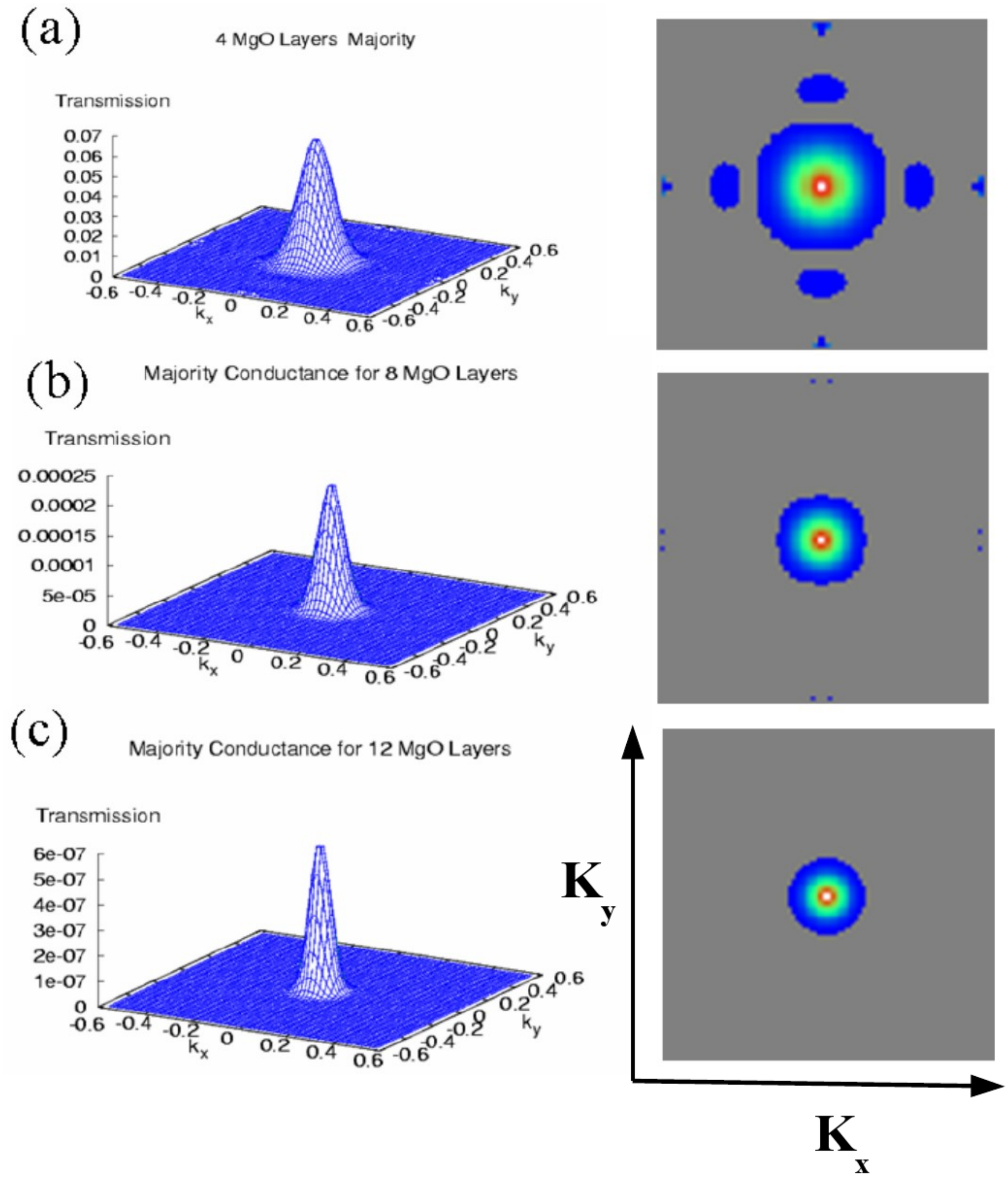

Figure 4.10: Majority spin channel conductance with parallel alignments of the magnetic moment of the iron electrodes. The left hand side is the transmission conductance with different width of MgO layers ((a) 4 layers of MgO, (b) 8 layers of MgO, and (c) 12 layers of MgO), whereas the right hand side is the contour plot of the same data [2].

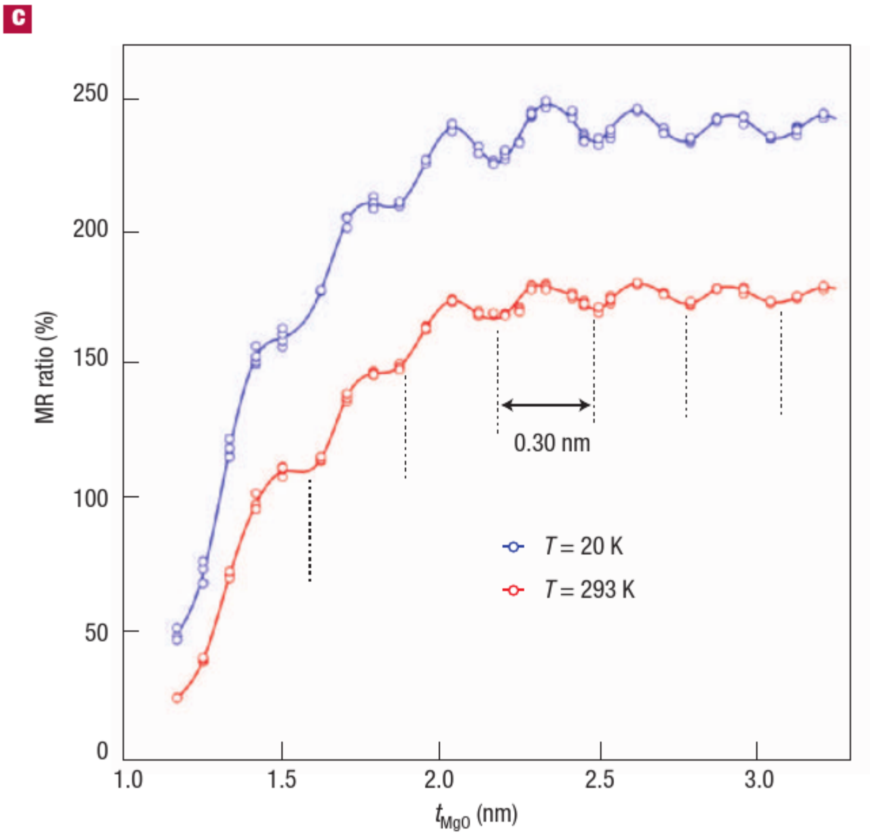

Figure 4.11: TMR variation as a function of the width of the insulating barrier, MgO, in a Fe|MgO|Fe magnetic tunnel junction. TMR oscillation with a period of 0.30nm suggest that there is perfect coherent tunnelling across the Fe|MgO|Fe MTJ. Figure reproduced from ref. [4].

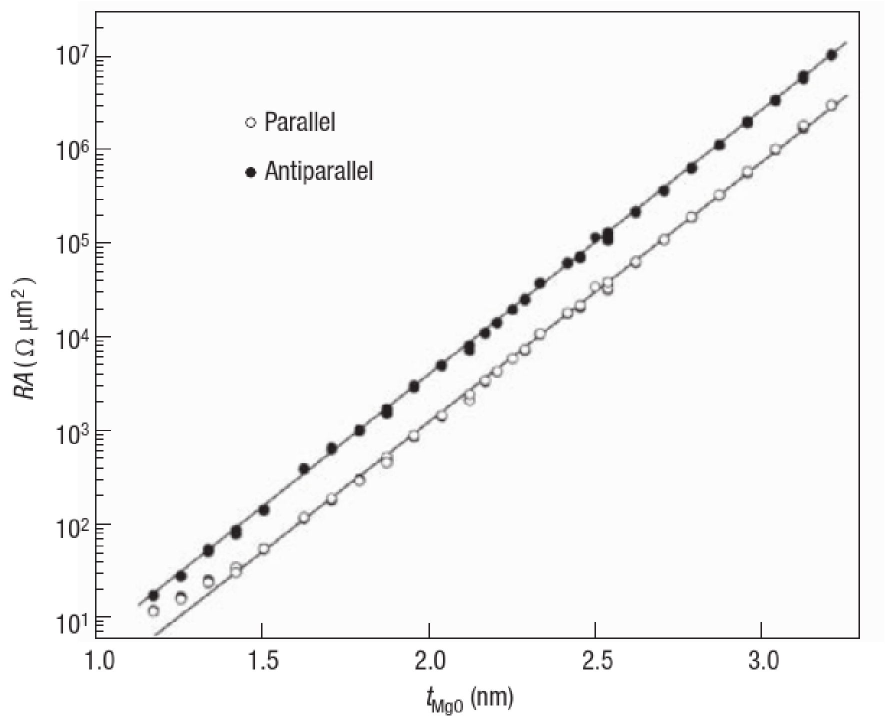

Figure 4.12: Resistance of the parallel and anti-parallel magnetic moments configuration of Fe|MgO|Fe junction as a function of MgO width. MgO cross section is $1\mu m \times 1\mu m$. The logarithmic plot on y-axis suggest that there is almost perfect tunnelling across the MgO junction. Figure reproduced from ref. [4].

4.6 Selection of ferromagnet electrode

The (k_x, k_y) amplitude decay plot of the insulating barrier te;; us about the transport supporting points. In contrast, the complex-band analysis tells us about the symmetry of the Bloch states, which tunnel easily at the transport supporting-points. By knowing the transport supporting-points we can decide on the ferromagnetic electrodes to use. The transport supporting-points and the filtering of the Bloch states at these-points are unique properties of the barrier material. The task of the ferromagnet is to supply the required symmetry of the Bloch state at the transport supporting-points for one spin (either spin-up or spin-down) along the transport direction. If the ferromagnet is able to supply the required symmetry of the Bloch state at each transport supporting-point then the corresponding TMR will be high, otherwise it will be low. So knowledge the transport supporting-points, the filtering of the Bloch states at these-points, and a compatible ferromagnet electrode are minimum requirements for the design of a magnetic tunnel junction (MTJ). One should keep in mind that the ferromagnet electrode should supply the required symmetry of the Bloch states at the transport supporting-points in the transport direction. In our case we have taken the transport direction as the z-axis.

4.7 Design of a magnetic tunnel junction

The lattice parameter of the insulating barrier and the ferromagnet electrodes needs to be commensurate at the interfaces at-least for the set-up of the ab-intio calculation. If the junction is commensurate in the experiments, then the TMR will be high, otherwise there will be defects generated due to the lattice mismatch at the interface. These defects will scatter the spin electrons and decrease the spin polarization current and lowering the TMR.

4.8 Band off-set calculation

After the junction formation, one should perform band off-set calculation to make sure that the MTJs is not metallic, i.e that it works in the tunnelling regime. If the junction turns metallic, then the purpose of the TMR calculation will fail. So, after the junction formation one should do a Siesta calculation to get the ground-state electronic properties such as density, total energy and band-gap of the MTJs. After the Siesta calculation, one should calculate the macroscopic average of the Hartree potential energy profile of the junction. One should also calculate the macroscopic average of the Hartree potential energy for the electrodes (electrochemical potential energy or Fermi energy), and the insulating materials. After that, by putting all together on a common macroscopic average of the Hartree potential energy profile of the junction one can draw a common Fermi energy level of the junction. If the junction does not cut or touch the valence band or conduction band of the insulator then the entire junction is insulating otherwise the junction is metallic. For example, in the case of Co|ZnO|Co MTJs the junction is metallic because the common Fermi level E_f is above the edge of the conduction band E_c of ZnO (see in Figure 4.13). Whereas in the case of Fe|AlN|Fe MTJs the junction is an insulator because the common Fermi level E_f is in the middle of the band-gap of AlN (see in Figure 4.14). This calculation is quick and one should always validate it before going further and doing transport.

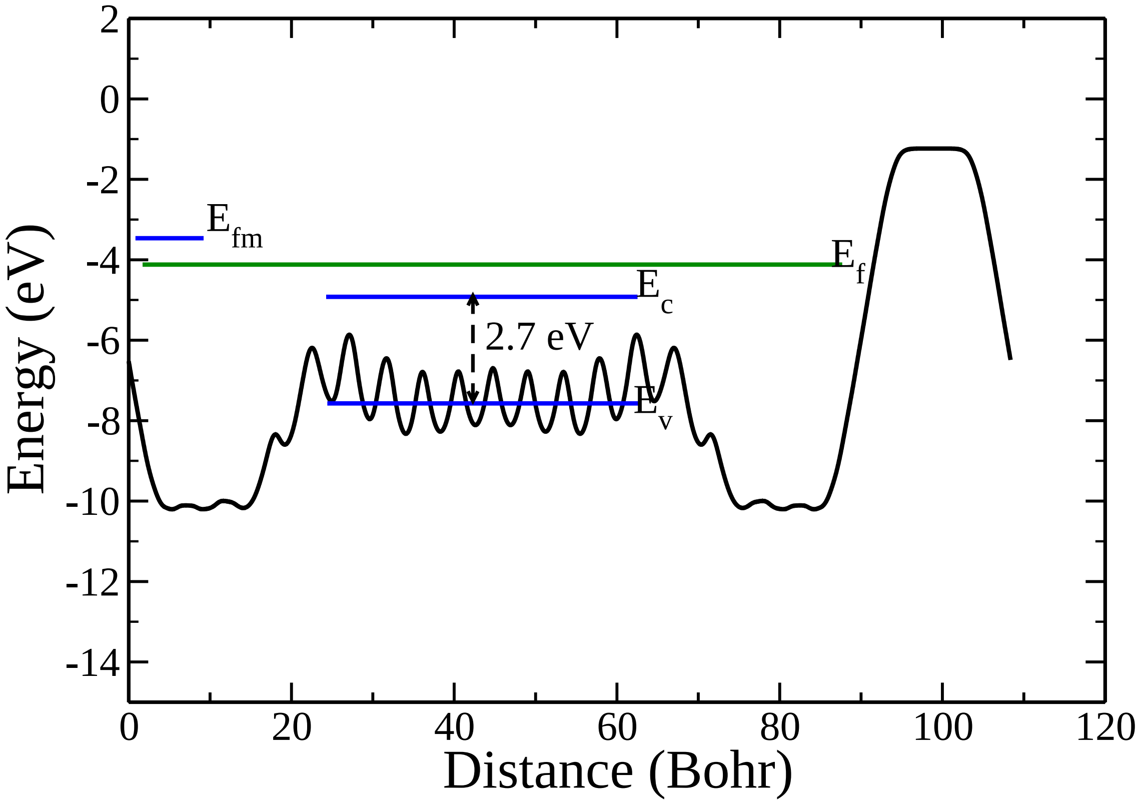

Figure 4.13: Co|ZnO|Co junction bands off-set. E_{fm} is the chemical potential of the cobalt electrodes. E_f is the common Fermi energy level of the whole junction. E_v is the valence band and E_c is the conduction band of ZnO. The continuous oscillatory curve, which starts at origin and ends around 110 Bohr, is the macroscopic average of the Hartree potential energy of electron in a Co|ZnO|Co junction.

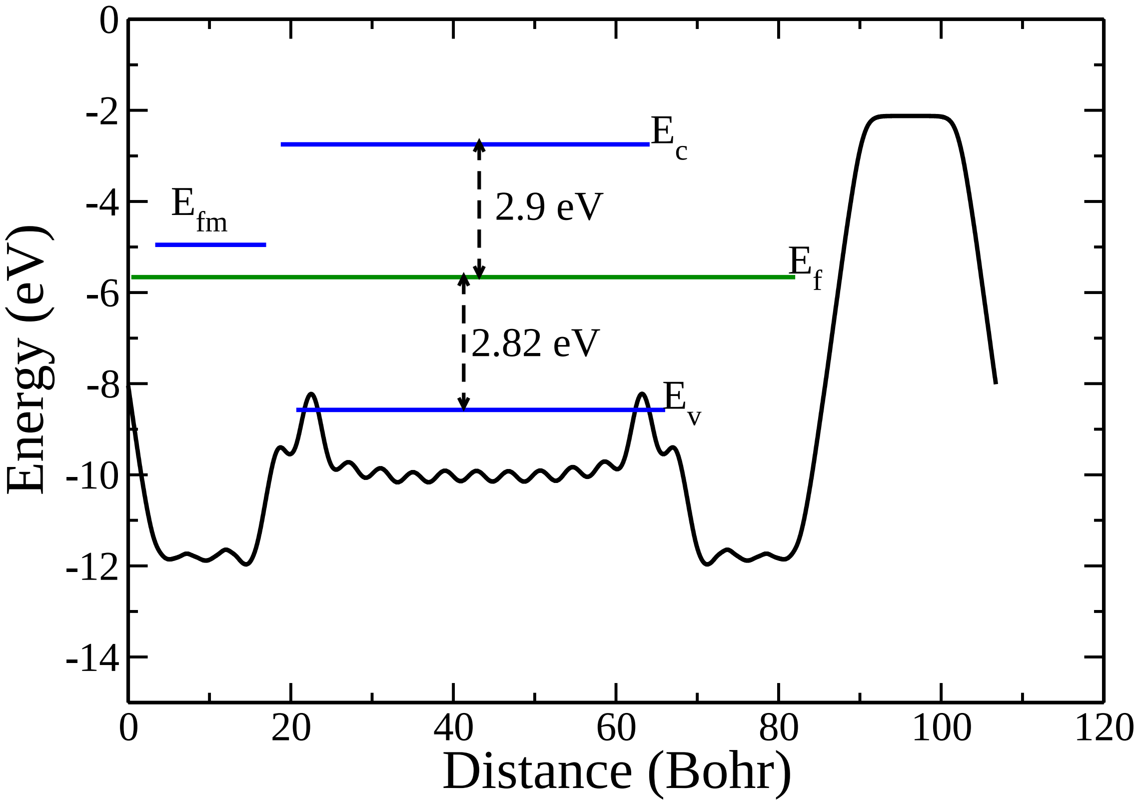

Figure 4.14: Fe|AlN|Fe junction bands off-set. E_{fm} is the chemical potential of the iron electrodes. E_f is the common Fermi energy level of the whole junction. E_v is the valence band and E_c is the conduction band of AlN. The continuous oscillatory curve, which starts at origin and end around 110 Bohr, is the macroscopic average of the Hartree potential energy of an electron in Fe|AlN|Fe junction.

4.9 Relaxation of MTJs interfaces

Once it is established that the junction is insulating, then one needs to relax the interface geometry properly. Relaxing the interface atoms to the correct structure is necessary because these atoms couple to each other and control the magnitude of the tunnelling current. There are various techniques through which the junction can be relaxed, but generally allowing the interface atoms to move in a certain direction (the z-direction along the transport direction in our case) can accelerate the relaxation. This trick generally helps in accelerating the relaxation process but does not guarantee that it will always work. The relaxation is in general dependent on the system under consideration. Once the interface atoms are relaxed then one should plot the force field of the full junction to make sure that the forces on each atom are less than the prescribed tolerance limit, which is in our case is 0.01 eV$\mathring{A}^{-1}$.

4.10 Siesta-Smeagol calculation set-up

In a TMR calculation the junction is divided into three regions, namely the left-lead, the scattering-region and the right-lead. The scattering-region is composed of two unit cells of left-lead interface atoms, the insulating material and two unit cells of right-lead interface atoms. The TMR calculation is divided into three parts. The first part is simply a Siesta calculation which generates a converged density matrix and Hamiltonian. This density matrix is then further used in a Smeagol coarse k-point grid calculation as an initial guess of the density matrix. The previously converged Hamiltonian file is used as the Hamiltonian matrix in a Smeagol k-point coarse grid calculation. Apart from both of these, the left-and right-lead Hamiltonians, the coupling matrices between the left-and the right-lead and the scattering region are also required. If the junction is symmetric then the left-lead and the right-lead coupling matrices will be same. If the junction is not symmetric then a problem arises. A non-symmetric junction is non-periodic and its unit cell contains a finite region of vacuum along the z-direction. This finite region of vacuum will generate a free surface on both side of the leads. So, we need to correct the periodic lead density matrix file from surface effects. After corrections we need to use this corrected lead density matrix as input in the Smeagol calculation using the inputs that come from the Siesta calculations that has been mentioned before. Once the coarse grid calculation is finished then we will use the same coarse grid converged density matrix as an input file for a dense mesh calculation. In a dense k-point mesh grid calculation we will assume that the converged density matrix of the dense grid is the same as the converged density matrix of the coarse grid. In a dense mesh calculation only one self-consistent cycle is needed, after that the Smeagol code performs the transport calculations.

Chapter 5

HfO_2 and SiO_2 as Tunnel Barriers

5.1 Introduction

The discovery by Fert [6] and Grünberg [7] of the giant magnetoresistance (GMR) effect in metallic magnetic multi-layers is often considered as the kick off of the now well-established field of *spintronics* [17]. GMR is the drastic change in the resistance of a magnetic nano-structure when its magnetic configuration is modified by a magnetic field. The simplest of such nano-structures is the spin valve, made of two magnetic layers separated by a non-magnetic metallic spacer. The two different magnetic configurations are obtained by aligning the magnetization vectors of the two magnetic layers either parallel (P) or anti-parallel (AP) to each other, with the parallel configuration often displaying the lower resistance. The same effect can be found when the spacer is an insulator and the charge carriers tunnel through its potential barrier. In this case the effect is called tunnelling magneto-resistance (TMR) and the spin valve is a magnetic tunnel junction (MTJ).

The first evidence for TMR was provided in the seventies for a Fe/Ge/Co MTJs at low temperature by Julliere [11], who also established a simple formula to relate the magnitude of the effect to the spin-polarization of the local density of states (DOS) of the two magnetic electrodes. Such spin polarization is simply defined as $P = \frac{D_\uparrow - D_\downarrow}{D_\uparrow + D_\downarrow}$, with D_σ being the DOS of the majority ($\sigma = \uparrow$) and minority ($\sigma = \downarrow$) electrons. Note that, depending on the particular experiments, the spin polarization of the current is not always proportional to that of the DOS [12]. A key result from Julliere's analysis is that, since the spin-polarization of magnetic transition metals is of the order of 50%, relatively small TMRs have to be expected. If one uses the "optimistic" definition of TMR, TMR= $\frac{I^{\mathrm{P}}-I^{\mathrm{AP}}}{I^{\mathrm{AP}}}$, with I^{P} (I^{AP}) being the current for the P (AP) configuration, then Julliere's theory returns us TMRs no larger than 60-70%. Such prediction has been confirmed through the nineties with many experimental demonstrations of room temperature TMR in various MTJs, mostly using amorphous $\mathrm{Al_2O_3}$ as insulating spacer [14] [13].

A major breakthrough came in the early 2000s, when Butler [3] and Mathon [15] independently demonstrated that epitaxial MTJs could, in practice, sustain an arbitrarily large TMR. This is because in epitaxial junctions the transverse k-vector (in the plane perpendicular to the MTJs stack direction), $\mathbf{k}_{\|}$, is conserved and the decay of the wave-function of the tunnelling electrons across the barrier depends on the orbital symmetry. For MgO along the [100] direction the states with the slowest decay rate are those around the Γ-point in the transverse Brillouin zone with Δ_1 symmetry. In Fe such symmetry is present along the [100] direction near the Fermi level, E_{F}, only for the majority electrons (spin-up electrons). As such a [100]-oriented Fe/MgO structure will effectively behave as a half-metal, if the barrier is thick enough. Such predictions were soon confirmed experimentally with reported room-temperature TMRs well exceeding 200% for the Fe/MgO/Fe system [16] [4], and now [100]-oriented FeCoB/MgO/FeCoB structures are at the foundation of a multitude of applications, ranging from magnetic data-storage to sensors [17].

Despite the concept of orbital-spin filtering applying to several stacks, such as [100] $\mathrm{SrRuO_3/BaTiO_3}$ and $\mathrm{SrRuO_3/SrTiO_3}$ [45], [100] Cu/EuO [46], Co(0001)/h-BN [47], [100] $\mathrm{Co_2MnSi/MgO}$ [48] and a few others, the FeCoB/MgO system is at present the only one used in mainstream applications. There are several reasons behind this fact including the highly perfected growth technology for such stacks and the temperature robustness of the magnetic properties of the Fe-Co alloy. Yet, FeCoB/MgO presents also some disadvantages. For instance, the Gilbert damping constant of Fe is large, so that applications based on spin-transfer torques are unlikely to be possible.

It is then important to enlarge the materials choice and thus design new possible stacks, not involving FeCoB and MgO. Here we investigate theoretically two such possibilities and study in details MTJs constructed with either SiO_2 or HfO_2 as barrier and with either Fe or Co as electrodes. SiO_2 and HfO_2 are both wide-gap semiconductors and they are already widely used in the microelectronics industry as gate oxides, while *hcp* Co has a small damping constant [49]. It is then expected that such new junctions will be highly compatible with standard CMOS technology and may offer the advantage of bringing memory elements close to the logic ones.

5.2 Computational details

We perform electronic structure and quantum transport calculations by using respectively density functional theory (DFT) and the non-equilibrium Green's functions method, still implemented with the Kohn-Sham DFT Hamiltonian (the NEGF+DFT scheme). The electronic structure of the various materials is calculated with the pseudo-potential local-orbital basis set SIESTA code [50] in the local density approximation (LDA) [51]. When computing the complex-band structure of SiO_2 and HfO_2 we use unit cells oriented respectively along the [0001] and the [001] directions, reflecting their hexagonal and cubic structure. In both cases we consider a grid spacing equivalent to a plane-wave cut-off of 700 Ryd and Monkhorst-Pack k-point meshes of $8\times8\times8$ and $5\times5\times5$, respectively for HfO_2 and SiO_2. Note that the complex-band structure is by definition always calculated along the z-direction, so that there is no need to sample the $\mathbf{k}_{||}\hat{z}$-direction. Finally we have considered a double zeta basis set for the s, p and d shells of Co and Fe, and s and p double zeta plus polarization orbitals for Si, Hf and O.

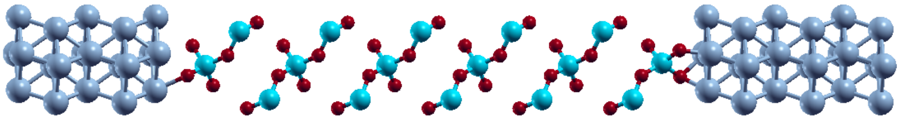

Figure 5.1: Schematic diagram of Co|SiO_2|Co based MTJs. The left and right magnetic-lead atoms are represented by the grey color, whereas the spacer SiO_2 is represented by the cyan (Si) and red (O) colors.

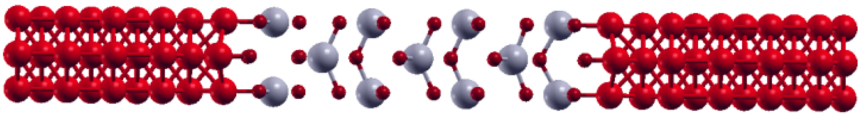

Figure 5.2: Schematic diagram of Fe|HfO_2|Fe based MTJs. The left and right magnetic-lead atoms are represented by the red color, whereas the spacer HfO_2 is represented by the grey (Hf) and red (O) colors.

We then construct two different MTJs, namely Co|SiO_2|Co (see in Figure 5.1) and Fe|HfO_2|Fe (see in Figure 5.2). In the first, both the electrodes and the barrier have an hexagonal structure, being Co in its naturally occurring *hcp* lattice and SiO_2 in the α-quartz phase (space group $P3_221$). The experimental in-plane lattice constants are 2.51Å for Co and 4.91Å for SiO_2, so that for a stack grown along the [0001] direction the lattice mismatch is about 2% (see in table 5.1). The epitaxy is then achieved by placing the Co atoms facing the O ones at the interface. In contrast both the barrier and the electrodes in Fe|HfO_2|Fe have cubic structure with experimental lattice constants of 5.08Å and 2.89Å, respectively for HfO_2 and Fe. In this case the lattice mismatch is more significant, of the order of 10% (see in table 5.1), and again epitaxy is achieved by placing the Fe atoms on top of oxygen at the interface. When constructing the MTJs stacks we fix the in-plane lattice constant to 4.91Å for Co/SiO_2 and to 5.64Å for Fe/HfO_2 (see in table 5.1) and relax the atomic coordinates by conjugate gradient until the forces are smaller than 0.01eV/Å. In particular, we consider two junctions where the SiO_2 and HfO_2 barriers are respectively 30.0Å and 22.15Å. Note that in the case of Fe/HfO_2 the large lattice mismatch implies significant strain in the junction. Here we have taken as common in-plane lattice parameter for the Fe|HfO$_2$|Fe MTJs the one of Fe, i.e. we have significantly expanded the lattice constant of HfO$_2$. We have verified that the HfO$_2$ band-gap (as calculated with the LDA) does not change in a significant way over such range of lattice parameters (see in Figure 5.3). In fact, it varies in a non-monotonic fashion when the lattice parameter goes from that of bulk HfO$_2$ (5.08Å) to that chosen for the junction (5.64Å), with the maximum variation being of the order of 0.4 eV (see in Figure 5.3). We then expect that our results will be rather insensitive (at least at a qualitative level) to the exact in-plane lattice parameter.

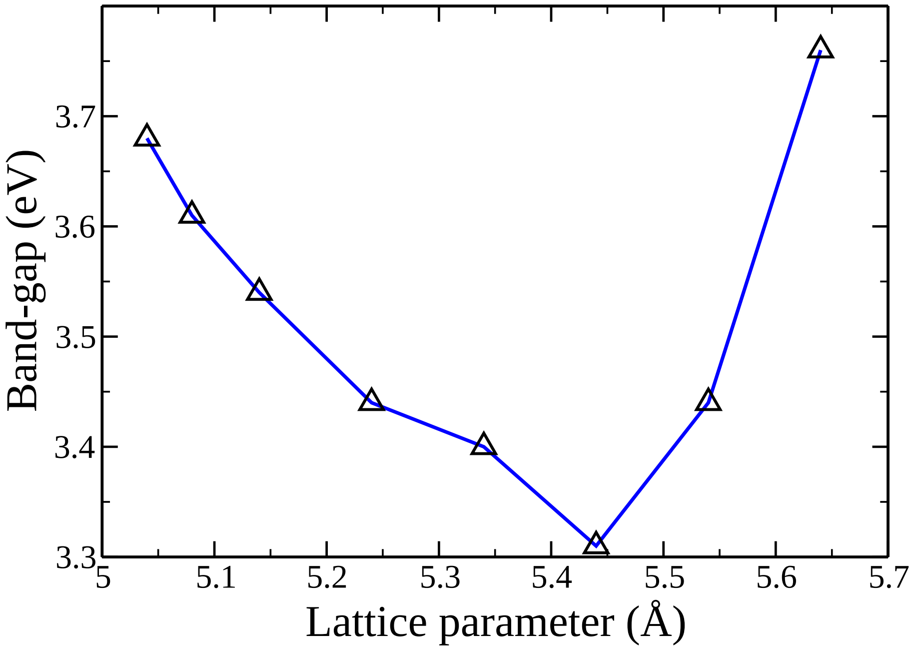

Figure 5.3: Schematic diagram of HfO$_2$ LDA band-gap as a function of lattice parameter. The triangles in the curve are the calculated data points.

Transport calculations are performed with the code Smeagol [56] [57] [58] , which implements the NEGF+DFT method with Siesta as a DFT platform. Smeagol calculates the electrical current at a given applied voltage, V, for spin σ ($\sigma =\uparrow, \downarrow$) from the Landauer-Büttiker formalism as

$$I^\sigma(V) = \frac{e}{h}\int dE\, T^\sigma(E;V)[f_\mathrm{L} - f_\mathrm{R}], \tag{5.1}$$

Material	**Required Lattice ($\AA$)**	**Natural Lattice ($\AA$)**	**Strain (%)**
bcc-Fe	2.82	2.89 [52]	2.4
hcp-Co	2.46	2.51 [53]	2.2
α-quartz-SiO_2	4.91	4.91 [54]	0
cubic-$\mathrm{HfO_2}$	5.64	5.08 [55]	11

Table 5.1: Materials natural and required lattice parameters and strains that are present in the Fe|$\mathrm{HfO_2}$|Fe and Co|$\mathrm{SiO_2}$|Co based magnetic tunnel junctions.

where e is the electron charge, h the Plank constant, $T^{\sigma}(E;V)$ the energy and voltage-dependent transmission coefficient, and f_{L} (f_{R}) the Fermi function associated to the left-hand (right-hand) side electrode. These curve evaluated at $E-\mu_{\mathrm{L}}$ ($E-\mu_{\mathrm{R}}$), where $\mu_{\mathrm{L/R}} = E_{\mathrm{F}} \pm \frac{eV}{2}$ is the chemical potential for the left/right electrode. Since the junction is translationally invariant in a plane perpendicular to the transport direction the transmission coefficient can be written as

$$T^{\sigma}(E;V) = \frac{1}{\Omega_{\mathrm{BZ}}} \int_{\mathrm{BZ}} d\mathbf{k}_{\parallel}\, T^{\sigma}_{\mathbf{k}_{\parallel}}(E;V)\,, \tag{5.2}$$

where the integration extends over the two dimensional Brillouin zone in the plane perpendicular to the transport direction and with area Ω_{BZ}. The transport calculations presented here are for the zero-bias limit only and are obtained by converging the charge density over a 8×8×1 k-point grid and the transmission coefficient over a 50×50×1 one. We have also performed additional tests for a 100×100×1 mesh, without noting any significant change in $T^{\sigma}(E;V)$ or the TMR.

5.3 Results and Discussion

5.3.1 SiO_2 and HfO_2 as tunnelling barriers

SiO_2 and HfO_2 are both wide-gap insulators widely used as gate oxides in the fabrication of nano-transistors. For SiO_2 our LDA calculations return an indirect band-gap of 5.6 eV with valence band maximum at the K-point and the conduction band minimum at Γ. This, as expected (LDA band-gaps are generally smaller than the experiment one, because error between calculated band-gap under LDA exchange correlation functional and experiment (9 eV) comes from local density approximation exchange and correlation functional [59]). In this case local density approximation functional under-bind the and make electrons more de-localised and thus consequently smaller band-gap. For cubic HfO_2 the LDA gives us a direct band-gap at X of 3.7 eV, which also in this case is underestimated. In fact, although we could not find experimental measurements for the cubic phase of HfO_2, the experimental range for the tetragonal one is 5-6 eV. Interestingly GW calculations report a gap value of 5.2 eV for the cubic phase and 6.1 eV for the tetragonal one [60] suggesting that the LDA underestimation of the experimental gap may be in the range of 2 eV. Note that we could have corrected the band-gap in the transport calculations by, for instance, applying a self-interaction corrections method [32] [33] or simply a scissor operator [61]. However, considering that the band-gaps are already rather large we have decided to continue the calculations at the LDA level. It is expected that the gap corrections in this case will introduce only quantitative effects, leaving the general physics of the problem unchanged.

Next we move to evaluate how the wave-function decays in the insulating barrier along the chosen directions. This is achieved by calculating the complex-band structure of the two materials. For a periodic solid the energy dispersion is obtained by calculating the N possible eigenvalues $\epsilon_n(k_x, k_y, k_z)$ corresponding to the real k-vector $\mathbf{k} = (k_x, k_y, k_z)$, where N is the number of basis functions in the unit cell. One can also solve the inverse problem and find the k_z component of the wave-vector (z is the direction of interest, namely the one of the transport), once both the transverse $\mathbf{k}_\parallel = (k_x, k_y)$ component and the energy, E, are fixed. When E corresponds to the material energy gap (or to mini-gaps) then the equation $E = \epsilon(\mathbf{k}_\parallel, k_z)$ can be solved for complex $k_z = q + i\kappa$. The transmission coefficient is expected to decay as a function of the barrier thickness, d, as $T(E, \mathbf{k}_\parallel) \sim T_0(E, \mathbf{k}_\parallel)\mathrm{e}^{-2\kappa(E,\mathbf{k}_\parallel)d}$, where $T_0(E, \mathbf{k}_\parallel)$ in general depends on the nature of the interface between the metal and the insulator. One can then plot $\kappa(E_\mathrm{F}, \mathbf{k}_\parallel)$ across the 2D Brillouin zone spanned by the transverse wave-vector $\mathbf{k}_\parallel$ and establish which portions of the Brillouin zone contribute the most to the tunnelling current. The results of such an exercise are presented in Fig. 5.4.

From the figure it is clear that for both insulators the minimum decay coefficient is found in the middle of the 2D Brillouin zone, namely at the Γ-point (see in table 5.2). This corresponds to tunnelling electrons having wave-vectors parallel to the transport direction, i.e. electrons that approach the energy barrier perpendicularly to the interface between the metal and the insulator. A situation as the one presented here is most typical and it is encountered for featureless potential barriers and parabolic band dispersions (the Fermi surface is spherical). It is also the same situation found for MgO along the [001] direction. One should also note that, in general, the decay across SiO_2 is significantly faster than that across HfO_2, due to its larger band-gap. Such decay coefficients are expected to become larger as the band-gap increases, so that corrections to the band-gap magnitude will change the rate of decay. These, however, will not modify the distribution of $\kappa(E_\mathrm{F}, \mathbf{k}_\parallel)$ across the Brillouin zone.

Next we need to analyse how the complex-band structure of the insulators relates to the real one of the magnetic electrodes. The tunnelling process in epitaxial junctions preserves the transverse wave-vector and only states with the same $\mathbf{k}_\parallel$ and the same symmetry contribute to the current. As such we now analyse the symmetry of the real

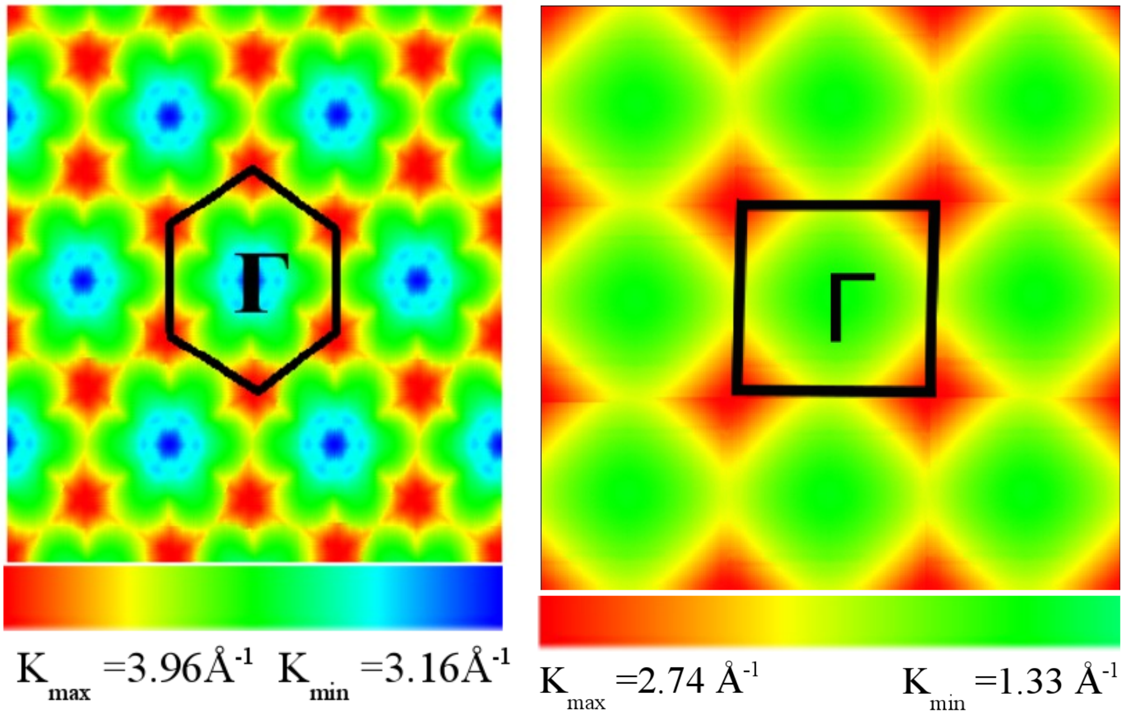

Figure 5.4: Heat colour plots of the wave-function decay coefficient, $\kappa(E_\mathrm{F}, \mathbf{k}_{\|})$, as a function of the transverse wave-vector, $\mathbf{k}_{\|}$, for SiO_2 (left-hand side panel) and HfO_2 (right-hand side panel). Calculations are carried out for $E_\mathrm{F} = 0$, placed in the middle of the band-gap. The black boxes mark the 2D Brillouin zones and the colour code is blue to green to red as κ gets larger. In both cases the decay coefficient is plotted in linear colour scale with the following limit: SiO_2 $\kappa_\mathrm{min} = 3.16\text{Å}^{-1}$, $\kappa_\mathrm{max} = 3.96\text{Å}^{-1}$; HfO_2 $\kappa_\mathrm{min} = 1.33\text{Å}^{-1}$, $\kappa_\mathrm{max} = 2.74\text{Å}^{-1}$.

and complex-band structure of the insulator along the direction of the transport at $\mathbf{k}_{\|} = \Gamma$, namely in the region of the 2D Brillouin zone, where the wave- function decay is minimum. Note, however, that this analysis provides only a tool for interpreting the behaviour of the transmission coefficient as a function of energy in terms of the band structure. The transmission itself, as explained in the Method section, is evaluated by integrating over the entire $\mathbf{k}_{\|}$ Brillouin zone and not by taking its value at the Γ-point only.

The symmetry of the Bloch states can be assigned by looking at their atomic orbital composition. In particular we denote as Δ_1 a Bloch state made of orbitals having zero angular momentum with respect to an axis orthogonal to the interface with the metal, namely s, p_z and $d_{3z^2-r^2}$ orbitals. In contrast, we label as Δ_2 orbitals with $d_{x^2-y^2}$ character, and as $\Delta_{2'}$ those with a d_{xy} one. Finally the Δ_5 symmetry is assigned to p_x, p_y, d_{xz} and d_{yz} orbitals. The real and complex-band structure for SiO_2 and HfO_2 calculated at the Γ-point in the 2D transverse Brillouin zone are presented in Fig. 5.5 and Fig. 5.6, respectively. In general the complex-bands appear smooth and connect the edges of the conduction and the valence band across the gap. We do not detect any sign of the spurious flat complex-bands, which sometimes appear when one considers non-orthogonal local-orbital basis sets, and in general they agree well with results available in literature [62].

The two insulators display a rather different behaviour. In fact, SiO_2 has a complex-band structure entirely dominated by the $\Delta_{2'}$ symmetry. The band presenting the slowest decay rates originates from one of the valence bands about 1 eV below the valence band maximum and closes at the conduction band minimum. There are two other complex-bands at the valence band maximum, also with $\Delta_{2'}$ symmetry, which however have a rather large curvature. As such these provide the slowest decay rate only in a tiny energy window around the top of the valence band and will not contribute to the transport, unless the Fermi level of the junction is pinned close to the valence band. In contrast HfO_2 has a band-gap dominated by two intersecting complex-bands presenting Δ_1 symmetry (as

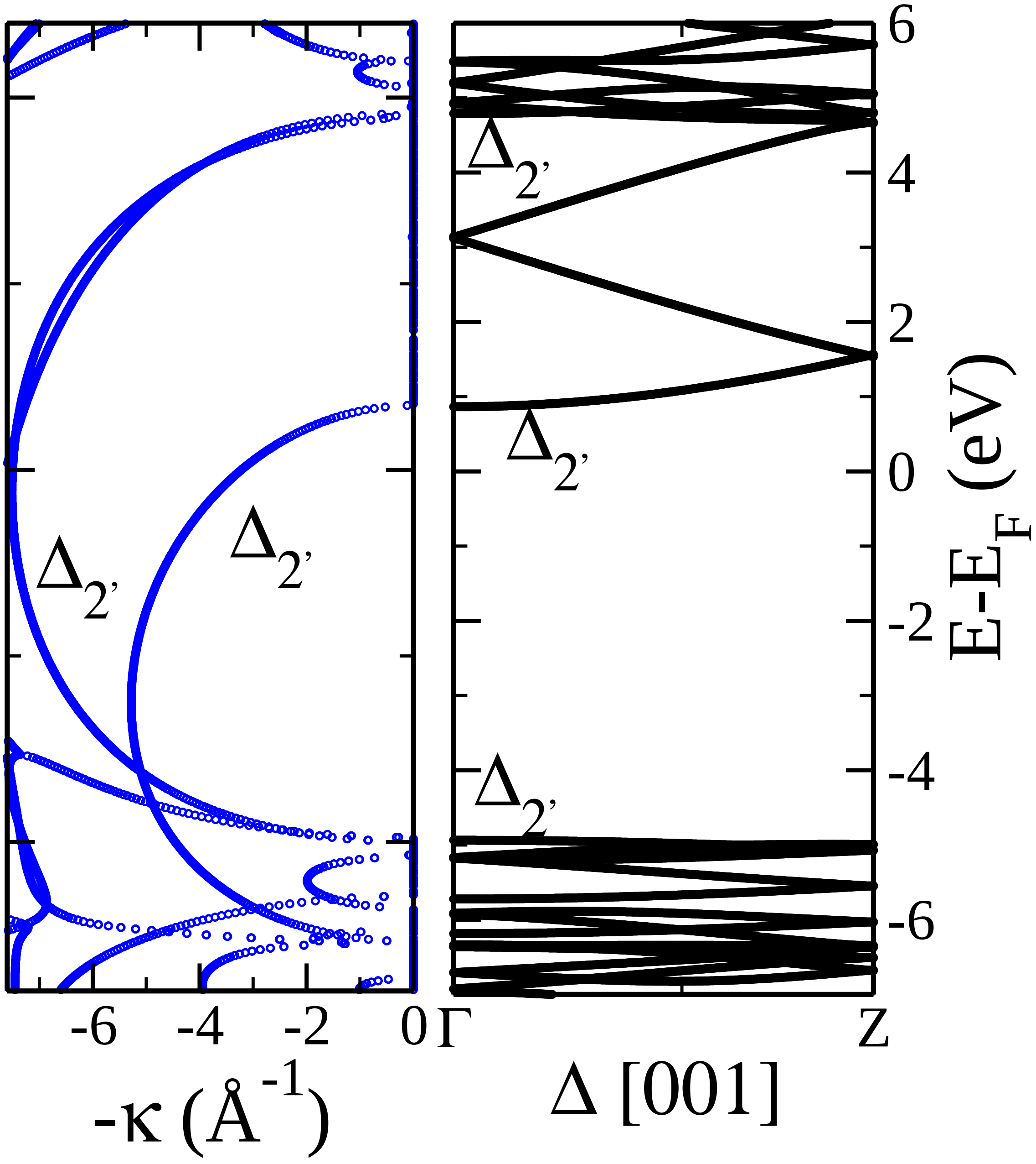

Figure 5.5: Real (right-hand side panel) and complex-band (left-hand side panel) structure of SiO_2 calculated at the Γ-point in the 2D transverse Brillouin zone. The symmetry labels, Δ_n, have been described in the text and the Fermi energy is taken in the middle of the gap.

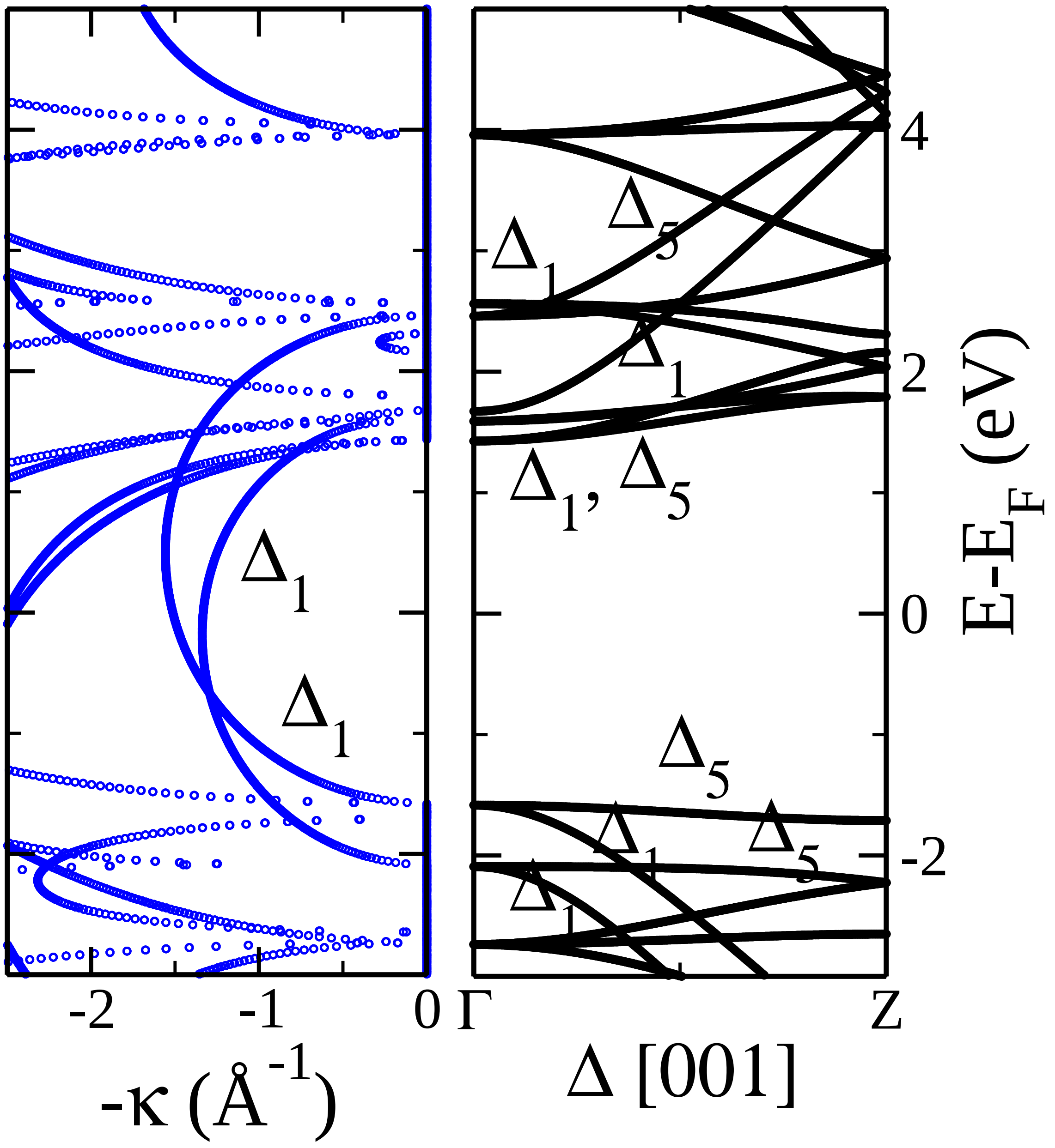

Figure 5.6: Real (right-hand side panel) and complex-band (left-hand side panel) structure of HfO_2 calculated at the Γ-point in the 2D transverse Brillouin zone. The symmetry labels, Δ_n, have been described in the text and the Fermi energy is taken in the middle of the gap. Note that the two complex-bands crossing the gap present Δ_1 symmetry, while there are also bands with much larger κ and Δ_5 symmetry.

Material	**Transport supporting point**	**Symmetry of the Bloch state is filtered at the transport supporting point**
HfO_2	Γ	Δ_1
SiO_2	Γ	$\Delta_{2'}$

Table 5.2: Material and its transport supporting points in $2d(k_x, k_y)$- first Brillouin zone, and symmetry filtering at the transport supporting points. In HfO_2, transmission is mainly concentrated around the Γ-point of the first Brillouin zone. In SiO_2 transmission is also mainly driven by the Γ-point. HfO_2 filters Δ_1 symmetry of the Bloch state at the Γ point, whereas SiO_2 filters $\Delta_{2'}$ symmetry of the Bloch state at the Γ point. In both cases the transport direction is along the z-axis.

identified from the orbital projections). These have a similar curvature and they appear shifted by about 1 eV with respect to each other.

5.3.2 Symmetry of the magnetic electrodes

We now move to analyse the symmetry of the real band structure of the magnetic electrodes along the direction of the transport. The most favourable situation is that in which one of the two spin sub-bands presents Bloch states at the Fermi energy with the same symmetry of those in the complex-band of the insulator, while the other spin sub-band does not. In this case only one spin direction will be transmitted with high efficiency and the electron/insulator stack will effectively behaves as a half-metal with the magnetoresistance increasing exponentially with the barrier thickness. For instance, this is the situation encountered for Fe/MgO along the [001] direction [3] [15].

The real band structure of *hcp*-Co along the [0001] direction and of *bcc* Fe along the [001] one are plotted in Fig. 5.7 and Fig. 5.8, respectively. We find that both magnetic

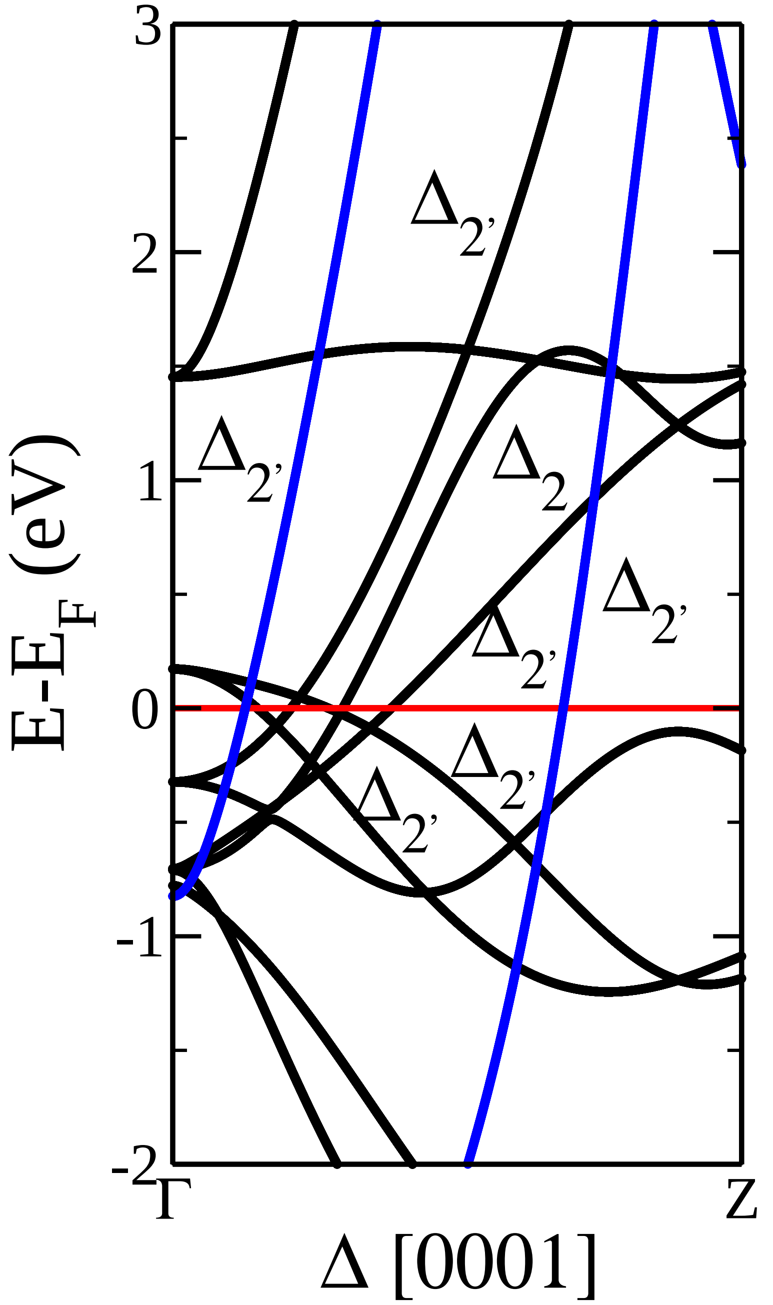

Figure 5.7: Real band structure of *hcp* Co plotted along the [0001] transport direction. The majority spin sub-band is in blue and the minority spin in black. The red horizontal line at $E_f = 0$ denotes the Fermi energy level of *hcp*-Co.

Ferromagnet	**Transport direction**	**Symmetry of the Bloch states available in the transport direction**
bcc-Fe	$\Gamma - Z$	$\Delta_{1\uparrow}$, $\Delta_{5\uparrow}$, $\Delta_{5\downarrow}$,
hcp-Co	$\Gamma - Z$	$\Delta_{2'\uparrow}$, $\Delta_{2'\downarrow}$

Table 5.3: Bulk *bcc*-Fe supplies both spin-up and spin-down Δ_5, and spin-up Δ_1 symmetries of the Bloch states along the transport direction [001]. Whereas, *hcp*-Co supplies both spin-up and spin-down $\Delta_{2'}$ symmetries of the Bloch state along [0001] direction.

electrodes supply Bloch states with the symmetry required by the insulator for each of the two spin directions (see in table 5.3). In the case of *hcp* Co there are bands with $\Delta_{2'}$ symmetry crossing the Fermi energy for both majority and minority spins (see in table 5.3). These are shifted with respect to each other by the exchange energy, but unfortunately provide high transmission for both spins. However, since Co is a strong ferromagnet with fully filled majority d band, the majority $\Delta_{2'}$ band at E_F has to be attributed to hybrid-$s-p-d$ states, so that the d orbital content is expected to be different from that of its minority counterpart (spin-down band).

The case of *bcc* Fe along [001] is different. In fact, there is only one majority band with Δ_1 symmetry at E_F, while there are also Δ_5 states for both spins (see in table 5.3). In particular the Fermi level crosses the top of the majority Δ_5 band and the bottom of the minority one. Thus, we expect single spin filtering for the majority Δ_1 channel, and some residual transmission for Δ_5 electrons with both spin directions (see in table 5.3).

5.3.3 Tunnel magneto-resistance

We finally turn our attention to the TMR of the proposed junctions and we start our analysis from the Co|SiO$_2$|Co one. The transmission coefficient as a function of energy is plotted for both spin channels and for both the parallel and anti-parallel configura-

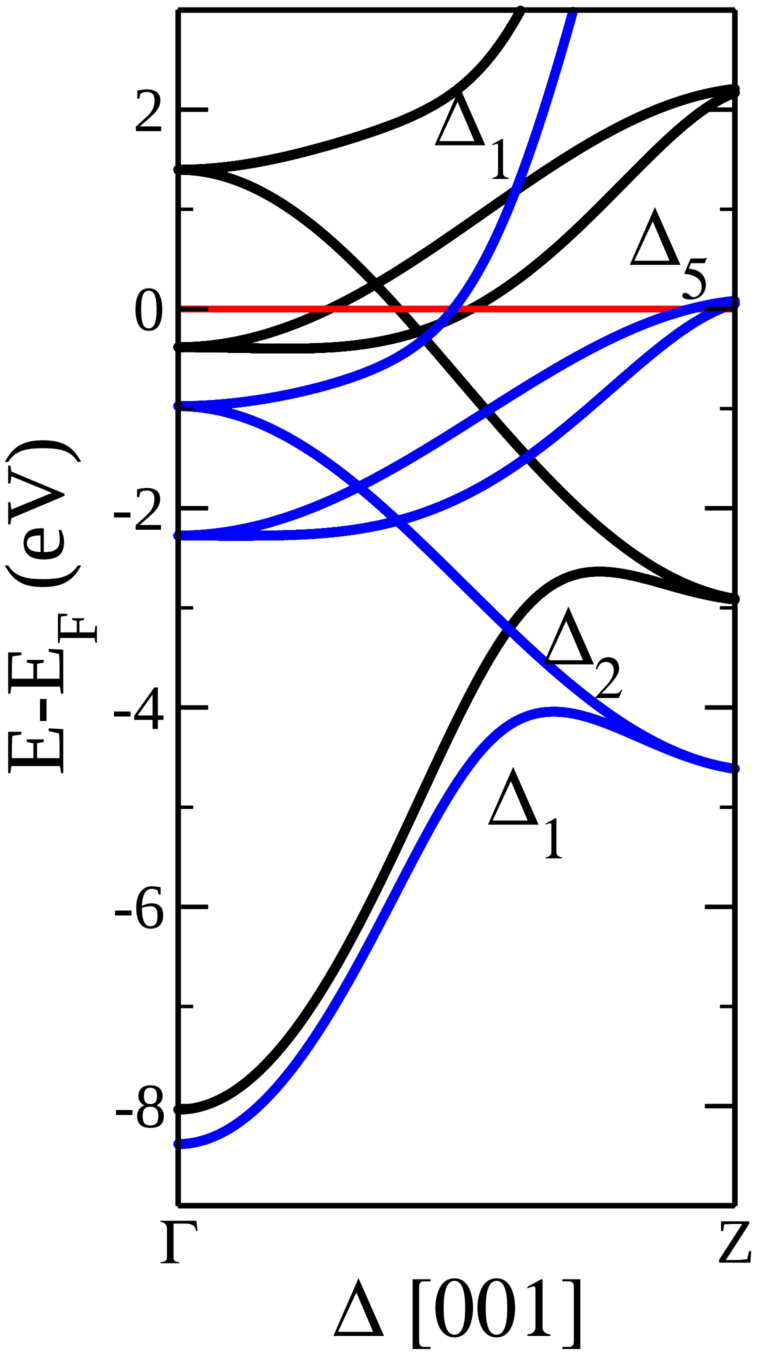

Figure 5.8: Real band structure of *bcc* Fe plotted along the [001] transport direction. The majority spin sub-band is in blue and the minority spin in black. The red horizontal line at $E_f = 0$ denotes the Fermi energy level of *bcc*-Fe.

tions in Fig. 5.9. As expected, in general, $T(E)$ drops drastically in an energy region approximately 6 eV wide, which corresponds to the calculated SiO_2 band-gap (along the transport direction). The Fermi level of the junction is positioned about 2 eV above the SiO_2 valence band maximum, so that the MTJs at low bias is deep in the tunnelling regime. Furthermore, once $T(E)$ is plotted in logarithmic scale as in Fig. 5.9, one can notice that $\log[T(E)]$ as a function of E effectively follows the lower-lying complex-band structure of SiO_2. This confirms that the transport is essentially dominated by the $\Delta_{2'}$ states identified by our symmetry analysis.

If one now focusses the attention on $T^\sigma(E)$ for the two spins (spin-up and spin-down) in the parallel configuration, it is easy to note that there are two energy regions where the transmission is dominated by one spin. This happens between E_F and $E_\mathrm{F}+1$ eV for the minority spin and between 1.5 eV and 3 eV above E_F for the majority one. It is difficult to ascribe such dependence to some clear features of the band structure along the transport direction since there are several bands with the right symmetry and, in addition, the transmission coefficient is integrated over the entire Brillouin zone, so that an entire region of k-points around Γ contributes to the transport. The same situation is not encountered for the anti-parallel configuration for which the $T^\sigma(E)$'s are almost spin-degenerate, since a majority (minority) electron in one electrode travels in the minority (majority) band of the other electrode. As such the transmission coefficient for the anti-parallel configuration is approximately a convolution of the transmission coefficients for the two spins in the parallel configuration. Note that here the spin degeneracy in the AP configuration is not exact since the two Co/SiO_2 surfaces relaxed to a slightly different geometry, so that the junction does not possess inversion symmetry.

The resulting TMR as a function of energy is plotted in the lower panel of Fig. 5.9 for an energy window of 2 eV around E_F. As expected from our analysis of the transmission coefficients we find a significant TMR in a region 1 eV wide above the Fermi level. The

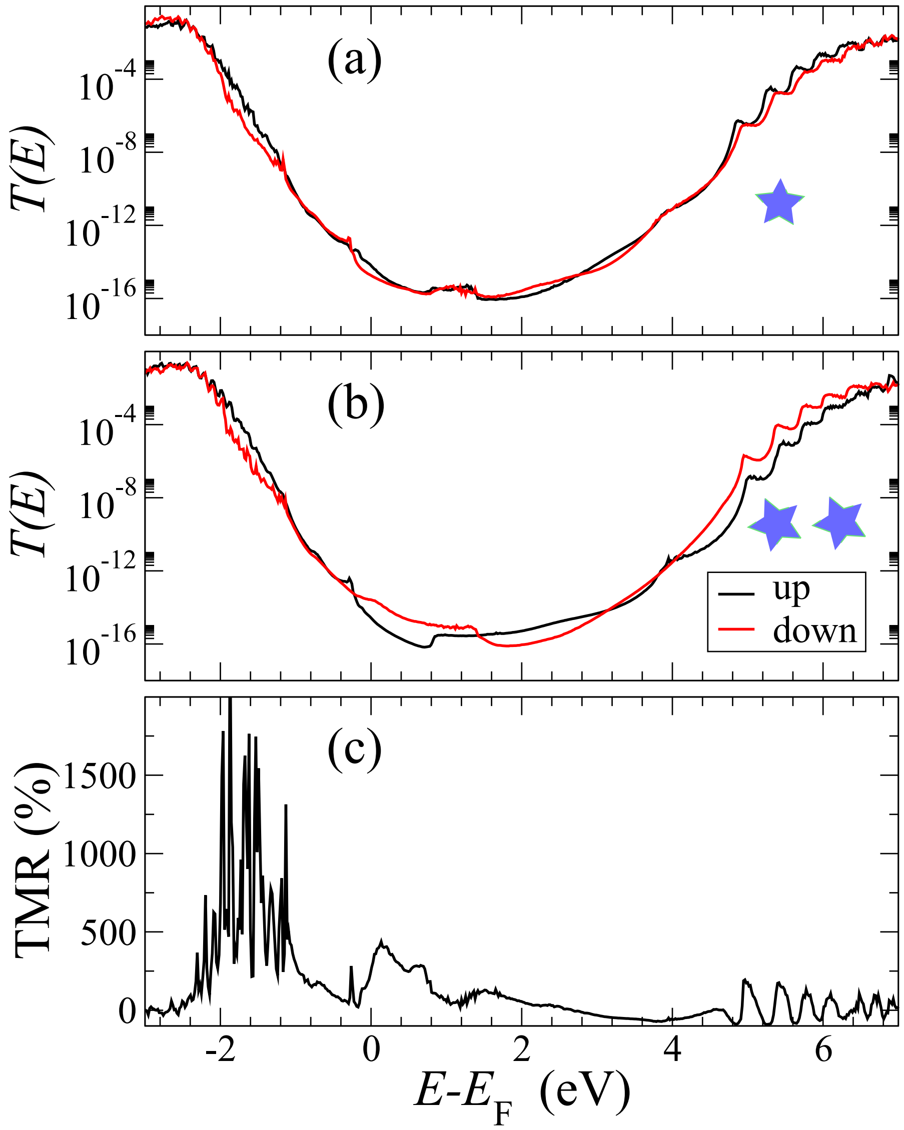

Figure 5.9: Transmission coefficient as a function of energy for the Co|SiO$_2$|Co MTJs. The thickness of the SiO$_2$ is $30.0\AA$ in the junction. The parallel (★), and anti-parallel (★★), configurations are plotted in panel (a) and (b) respectively. $T(E)$ for the majority (minority) spins is plotted in black (red). For the anti-parallel case the spin direction is set by the left-hand side electrode. The transmission coefficient is plotted on a logarithmic scale. In the lower panel (c) we present the calculated zero-bias TMR as a function of energy in the same energy window as the transmission coefficients.

maximum value of about 450% is reached at $E = E_F + 0.14$ eV, while the calculated TMR at the Fermi energy is approximately 250% (see in table 5.4). This is indeed larger than what expected from the simple density of state argument brought by Julliere's analysis, indicating that some spin filtering effect is at play. However, our discussion on the band structure of the insulator and the electrodes suggests that, if such spin filtering takes place, it will be related either to complex-bands with $\Delta_{2'}$ symmetry and large decay constant, or to portions of the 2D Brillouin zone away from the Γ-point.

Finally we take a look at the Fe|HfO$_2$|Fe MTJs. In this case the various transmission coefficients are shown in Fig. 5.10, again plotted in logarithmic scale. In this case the situation is significantly more complex since the $T(E)$'s present quite some structure even in the gap region. The band-gap is about 4 eV and the Fermi level cuts approximately 1 eV above the valence band maximum. Let us start the discussion once again from the majority spins in the parallel configuration. In this case $T(E)$ displays relatively high transmission in the energy region comprised between $E_F - 1$ eV and E_F, a region corresponding to the presence of bands with both Δ_1 and Δ_5 symmetry. For $E > E_F$ the transmission drops significantly, although the Δ_1 band is still present and it is the low-transmission Δ_5 symmetry to stop contributing.

When the same analysis is carried out on the minority spin band we find a region of small transmission between $E_F - 1$ eV and E_F. This is a region where there are no Δ_1 or Δ_5 bands, since the first of the Δ_5 bands has its onset just around E_F. As one passes E_F the Δ_5 band starts to dominate the transport. This remains relatively large until one reaches the energy corresponding to the minority Δ_1 band, which is also the energy corresponding to the upper band-edge of the Δ_5. This analysis clearly demonstrates that for Fe|HfO$_2$|Fe there is some level of spin filtering, since in an energy region extending 1 eV below the Fermi level and terminating just above E_F the high transmission Δ_1 band appears only for majority spins.

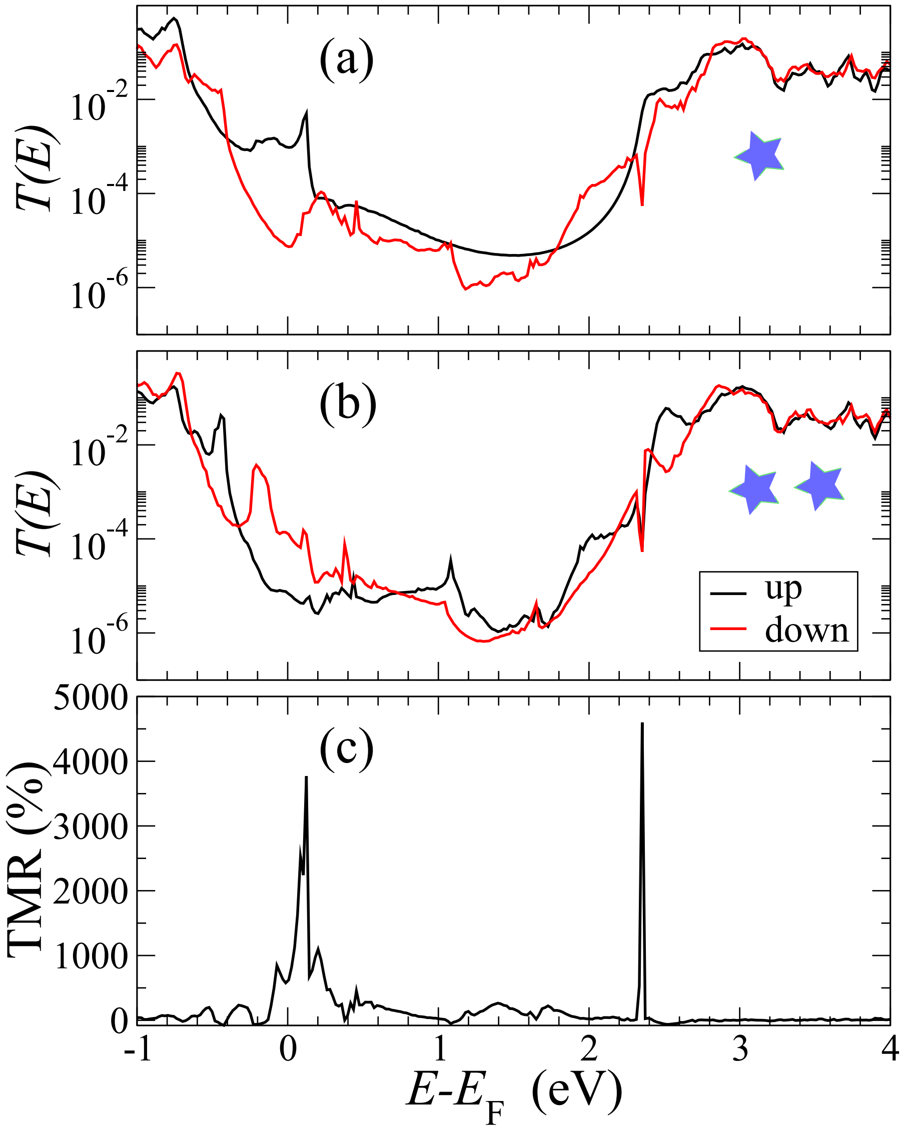

Figure 5.10: Transmission coefficient as a function of energy for the Fe|HfO$_2$|Fe MTJs. The thickness of the HfO$_2$ is 22.15$\mathring{A}$ in the junction. The parallel (★), and anti-parallel (★★), configurations are plotted in panel (a) and (b) respectively. $T(E)$ for the majority (minority) spins is plotted in black (red). For the anti-parallel case the spin direction is set by the left-hand side electrode. The transmission coefficient is plotted on a logarithmic scale. In the lower panel (c) we present the calculated zero-bias TMR as a function of energy in the same energy window as the transmission coefficients.

As in the case of Co|SiO_2|Co the transmission coefficients for the anti-parallel configuration appear as some convolution of those for the two spins in the parallel one. However, since the band-gap of HfO_2 is significantly smaller than that of SiO_2 and so is the complex component of the wave-vector in the gap, the small differences between the left-hand and right-hand interfaces with the electrodes significantly lift the spin degeneracy of $T(E)$. Note that the analysis of the various transmission functions in terms of the complex-band structure done here is not as sharp and definitive as the one that one can carry out for Fe/MgO. The reason behind such behaviour is that indeed the transmission is maximised at Γ (see in Figure 5.4), but the complex wave-vector at the Fermi level is a relatively smooth function across a wide region in the middle of the Brillouin zone. This means that a significant portion of the central part of the Brillouin zone may also contribute to the transport.

The TMR as a function of energy is then plotted in the lower panel of Fig. 5.10 and nicely corroborates our analysis. In fact we find a robust TMR, reaching up to 3,500% for energies up to 0.25 eV above the Fermi level. This is the energy window where the tunnelling in the majority sub-band is dominated by states with Δ_1 symmetry and that in the minority one by states with Δ_5. Note that the upper edge of the majority Δ_5 band almost coincides with the lower edge of the minority one, and the TMR is maximized essentially at that particular energy. At the calculated Fermi level the TMR is about 600%, which is significantly larger than that predicted by Julliere's formula. In this case we can indeed identify the spin filtering mechanism at the Γ-point as the main contributor to such large TMR, and therefore the Fe|HfO_2|Fe MTJs can represent a valid alternative to other spin filtering MTJs stacks (see in table 5.4). Unfortunately, however, since the spin filtering occurs only in a relatively small energy window, we expect that the bias dependence of the TMR will be rather severe and that little TMR will be detected for biases larger than approximately 0.5 V.

Junction	**Transport supporting point**	**Symmetry filter of the Bloch state at the Transport supporting point**	**TMR (%)**
Fe[001]|HfO_2[001]|Fe[001]	Γ	Δ_1	3500
Co[0001]|SiO_2[001]|Co[0001]	Γ	$\Delta_{2'}$	250

Table 5.4: Transmission in Fe|HfO_2|Fe junction is only around the Γ point, and HfO_2 filters Δ_1 symmetry of the Bloch state at the Γ point. Zero-bias transmission analysis suggests that tunnelling magneto-resistance in Fe|HfO_2|Fe junction is ~3500%. Whereas, transmission in Co|SiO_2|Fe junction is also around the Γ point, and SiO_2 filters the $\Delta_{2'}$ symmetry of the Bloch state at the Γ point. Zero-bias transmission analysis suggests that tunnelling magneto-resistance in Co|SiO_2|Co junction is ~250%.

5.4 Conclusion

In summary, we have explored the possibility of using the wide-gap insulators SiO_2 and HfO_2 as tunnel barriers in novel magnetic tunnel junctions. Both SiO_2 and HfO_2 are currently used in the microelectronic industry so that MTJs based on such insulators have the potential to be integrated in hybrid memory/logic components. We have performed a complex-band structure analysis and identified the dominant symmetry of the tunnelling electrons in the two materials (see in table 5.2). We have found that electron transmission is high for Bloch states with $\Delta_{2'}$ symmetry in SiO_2, while it has Δ_1 symmetry for HfO_2 (see in table 5.2).

We have then investigated two possible MTJs, namely Co|SiO_2|Co and Fe|HfO_2|Fe, respectively oriented along the [0001] and the [001] direction. The first one does not present spin filtering for any energies around E_F since Co supplies electrons with $\Delta_{2'}$ for both spins (see in table 5.3). However, since Co is a strong magnet the orbital character of such $\Delta_{2'}$ band appears different for the two spins and still a significant zero-bias TMR is found. In contrast, the Fe|HfO_2|Fe MTJs presents spin filtering and the TMR is predicted rather large for a relative narrow energy just above E_F (see in table 5.4). Our work has demonstrated that SiO_2 and HfO_2 can be used as tunnel barriers in MTJs (see in table 5.4), although for high performance junctions one probably has to look at magnetic electrodes different from simple transition metals.

Chapter 6

ZnO, GaN and AlN as Tunnel Barriers

6.1 Introduction

ZnO, AlN and GaN are known as display materials in the electronic industry. Due to recent advances in fabrication technology, better quality epitaxial films based on these semiconducting materials have been successfully grown on many substrates. Due to this progress we have investigated the performance of such semiconducting materials as insulating layers in tunnelling magneto-resistance (TMR) junctions. A typical TMR junction consists of two ferromagnetic layers and an insulating spacer sandwiched between them. The first materials requirement for a large TMR is that the ferromagnetic and the insulating layers need to be epitaxially grown. This is in order to avoid a large inter-facial defect concentration and to avail of symmetry spin-filtering. Keeping this condition in mind, we have constructed and analysed three junctions, namely Co(Fe)|ZnO|Co(Fe), Co(Fe)|AlN|Co(Fe) and Co(Fe)|GaN|Co(Fe), all of them using either [111]-oriented *bcc*-Co and *bcc*-Fe as ferromagnetic electrodes. The ground-state electronic properties of these junctions are obtained with *ab-initio* density functional theory (DFT) calculations, while the electron transport is calculated with the non-equilibrium Green's function formalism as implemented in Smeagol. For all these semiconducting spacers the valence band maxima are predominantly p_z in character, whereas the conduction band minima are s-like. This imposes particular symmetries to the complex-band structure, which in turn affects the spin-filtering and the TMR. We have found that ZnO, AlN and GaN are all capable of showing the symmetry filtering mechanism found in the Fe|MgO|Fe tunnel junctions. However, in general the TMR remains small, since the complex-band structure of the barrier is mismatched with the real band structure of the electrodes. In this chapter, we will discuss about the selection of ferromagnet electrodes, symmetry filtering by semiconductors materials, Siesta-Smeagol set up for transport calculation, transmission analysis, band off-set calculation between the ferromagnet and the semiconductors and in the end we will conclude the chapter.

6.2 Ferromagnetic electrodes and formation of MTJs

We consider here three conventional ferromagnetic electrodes namely iron, cobalt and nickel (Fe,Co and Ni). Fe has a *bcc*, Co a *hcp* and Ni has a fcc crystal structure at room temperature. The lattice parameter of Fe, Co and Ni are 2.89 Å [52], 2.51Å [53] and 3.52Å [63], respectively. Co also exists in a *bcc* crystal structure [64] in metastable form and it is stable against isotropic and monoclinic strain [64]. However, *bcc* Co is not stable against tetragonal Bain strain [64]. Wurzite crystal structure materials with [0001] face appears easy to fabricate on the *bcc* [111] face or the fcc [111] one, therefore we have chosen a ferromagnet with [111] orientation in our magnetic tunnel junction (MTJ) formation and transport analysis. Our strain calculations between the ferromagnet and the display semiconductor materials (ZnO, GaN, and AlN) suggest that the fcc Ni does not represent a suitable ferromagnet for forming a MTJs with display materials (ZnO, GaN, and AlN).

A brief analysis goes as follows: The Ni [111] face looks like a hexagonal closed packed structure with atom to atom distance $\frac{3.52\overset{\circ}{A}}{\sqrt{2}} = 2.49$Å. In the junction formation the lattice mismatch between the Ni [111] and the ZnO [0001] face is $\sim 23.38\%$, whereas between the Ni [111] and the GaN [0001] face is $\sim 21\%$. Finally between the Ni [111] and the AlN [0001] face the mismatch is $\sim 19.4\%$. Due to the large lattice mismatch between the Ni [111] surface and the ZnO, GaN and AlN [0001] faces we have decided to discard Ni as a ferromagnetic electrode in our magnetic tunnel junction (MTJ) analysis.

In the case of the *bcc*-Fe and *bcc*-Co [111] face the lattice mismatch between the ferromagnet and the display materials [0001] face is about $\sim 6\%$. Therefore we have chosen *bcc* Fe and *bcc* Co as ferromagnetic electrodes. Both *bcc*-Fe and *bcc*-Co have almost the same band structure and supply both spin channel with a Δ_1 symmetry (see in table 6.5) of the Bloch state in the [111] transport direction (see in Figure 6.1). In our MTJs set up Fe and Co act as a ferromagnetic electrodes, whereas ZnO, GaN and AlN act as an insulating spacer between them. In order to design a commensurate junction between the *bcc*-Fe or *bcc*-Co [111] face and the ZnO [0001] face the required lattice parameter for *bcc*-Fe or *bcc*-Co is 2.73Å and for ZnO is 3.34Å. In order to design a commensurate junction we compress the *bcc*-Fe and *bcc*-Co natural lattice parameter from 2.89Å to 2.73Å, which translate into $\sim 5.5\%$ strain. This $\sim 5.5\%$ compressive strain does not affect significantly the iron work-function (see in Figure 6.2), however it does affect the cobalt one (see in Figure 6.3) and makes it more reactive by 1.2 eV than natural *hcp* cobalt. For the ZnO case we have extended its natural lattice parameter from 3.25Å to 3.34Å, which corresponds to about $\sim 2.8\%$ strain (see in table 6.1). This $\sim 2.8\%$ extensive strain changes the ZnO crystal structure from bulk wurzite into a graphite like planar form (see in Figure 6.4). In the GaN case we have extended the lattice parameter from 3.15Å to 3.34Å, which corresponds to $\sim 6\%$ strain (see in table 6.1). Such $\sim 6\%$ extensive strain does not change the GaN bulk wurzite crystal structure (see in Figure 6.5). Finally in the case of AlN we have extended the lattice parameter from 3.09Å to 3.34Å, which is $\sim 8\%$

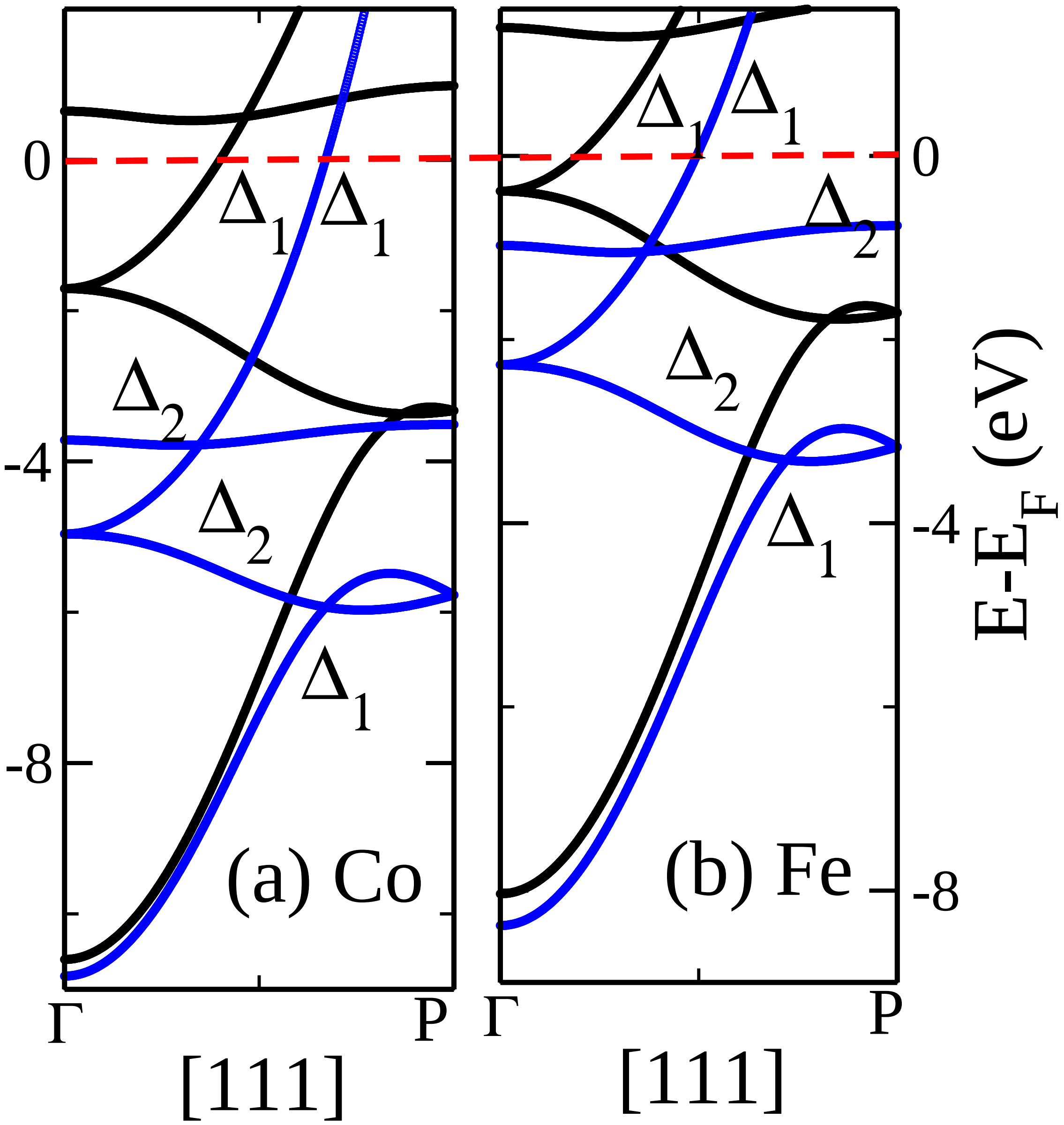

Figure 6.1: (a) *bcc* cobalt and (b) *bcc* iron bands structures along the [111] transport direction. Iron and cobalt both supply "spin-up" (blue color) and "spin-down" (black color) Δ_1 symmetry Bloch states along the [111] transport direction. The red dashed line denotes the Fermi level, $E_f = 0$ eV.

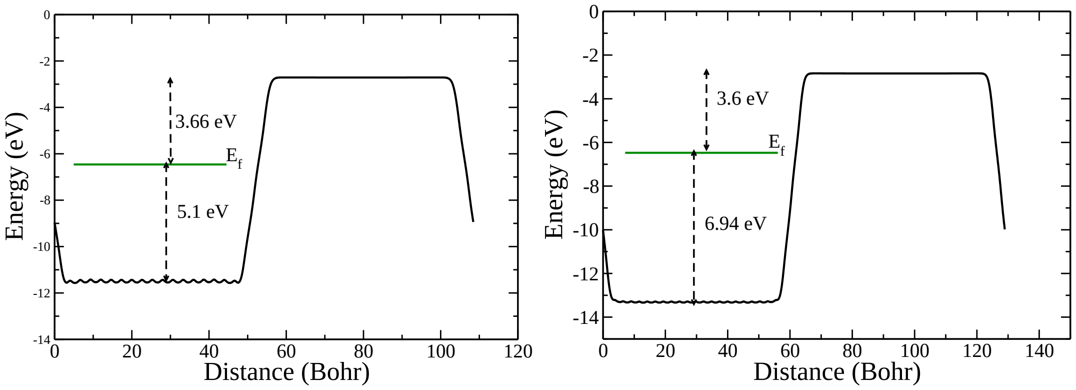

Figure 6.2: Left: The work-function of natural *bcc* iron with a bulk lattice parameter of 2.87 Å. The Fermi energy E_f is the calculated electrochemical potential of natural bulk *bcc* iron. The calculated work-function of *bcc* iron is 3.66 eV. Right: The work-function of *compressed bcc* iron with a bulk lattice parameter of 2.73 Å. The Fermi energy E_f is the calculated electrochemical potential of compressed bulk *bcc* iron. The calculated work-function of compressed *bcc* iron is 3.6 eV.

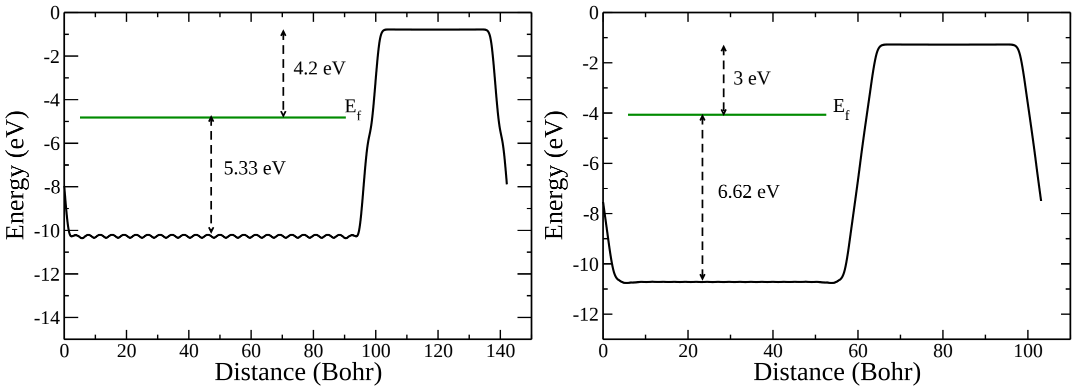

Figure 6.3: Left: The work-function of *natural hcp cobalt* with a bulk lattice parameter of 2.51Å. The Fermi energy E_f is the calculated electrochemical potential of natural bulk *hcp* cobalt. The calculated work-function of natural *hcp* cobalt is 4.2 eV. Right: The Work-function of *compressed bcc cobalt* with a bulk lattice parameter of 2.73Å. The Fermi energy E_f is the calculated electrochemical potential of compressed bulk *bcc* cobalt. The calculated work-function of compressed *bcc* cobalt is 3.0 eV and it is significantly smaller than that of *hcp* Co.

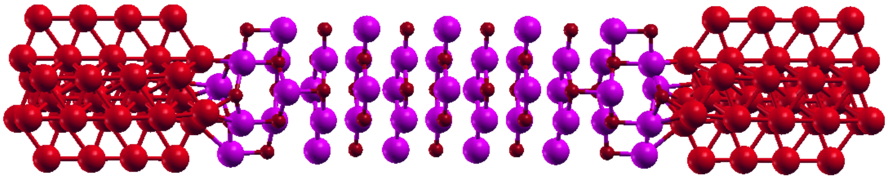

Figure 6.4: Schematic diagram of Co|ZnO|Co or Fe|ZnO|Fe based MTJs. The left and right magnetic-lead atoms are represented by the red color, whereas the spacer the planar ZnO is represented by the pink (Zn) and red (O) colors.

strain (see in table 6.1). The extensive $\sim 8\%$ strain does change the AlN bulk wurzite crystal structure into a graphite-like planar one (see in Figure 6.6). We have relaxed all the magnetic tunnel junctions (MTJ) until the maximum forces on each atom was than our tolerance limit of 0.01eV/Å.

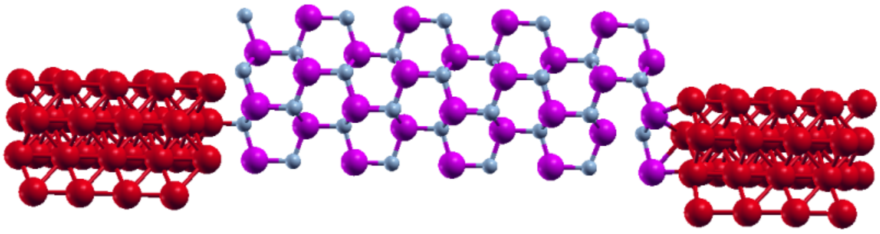

Figure 6.5: Schematic diagram of Co|GaN|Co or Fe|GaN|Fe based MTJs. The left and right magnetic-lead atoms are represented by the red color, whereas the spacer GaN is represented by the pink (Ga) and grey (N) colors.

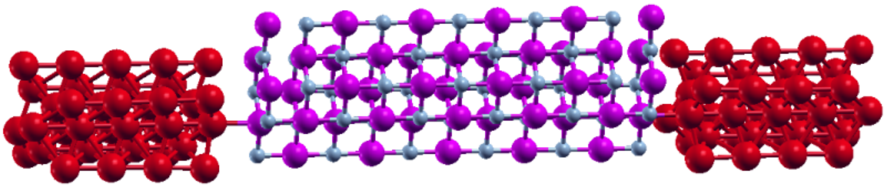

Figure 6.6: Schematic diagram of Co|AlN|Co or Fe|AlN|Fe based MTJs. The left and right magnetic-lead atoms are represented by the red color, whereas the spacer the planar AlN is represented by the pink (Al) and grey (N) colors.

Material	**Required Lattice** ($\AA$)	**Natural Lattice** ($\AA$)	**Strain** (%)
bcc-Co	2.73	2.89 [52]	5.5
bcc-Fe	2.73	2.89 [52]	5.5
wurzite-ZnO	3.34	3.25 [65]	2.7
wurzite-GaN	3.34	3.15 [66]	5.7
wurzite-AlN	3.34	3.09 [67]	7.5

Table 6.1: Materials natural and required lattice parameters and strains that are present in various magnetic tunnel junction based on *bcc*-Co and *bcc*-Fe as a ferromagnet, with ZnO, GaN, and AlN as an insulating barriers.

6.3 Electronic properties of the display materials

ZnO, GaN and AlN have all a wurzite crystal structure in the bulk [68] [69]. The natural lattice parameter of ZnO is 3.25Å [65] of GaN is 3.15Å [66] and of AlN is 3.09Å [67]. All these are wide direct band-gap semiconductors (see in table 6.2). The experimental band-gap of ZnO, GaN and AlN are $\sim$ 3.25 eV [22], $\sim$ 3.15 eV [23] and $\sim$ 6.1 eV [23], respectively (see in table 6.2). In contrast of the LDA band-gaps of ZnO, GaN and AlN are $\sim$ 0.61 eV [70], $\sim$ 2.2 eV [70] and $\sim$ 4.16 eV [70], respectively (see in table 6.2). In our transport calculation we have used the LDA+ASIC (atomic self-interaction correction) scheme to correct the band-gaps. These are $\sim$ 2.7 eV for ZnO, $\sim$ 3 eV for GaN and $\sim$ 5.72 eV for AlN, (see in table 6.2) i.e. they are significantly closer to the experimental ones.

6.4 Symmetry filtering by the display materials

In order to study the symmetry filtering in ZnO, GaN and AlN, we perform 2D (k_x, k_y) decay plot of the Bloch wave-function for the smallest decay rate wave-vector κ and the

Material	**Bulk crystal structure**	**Calculated band-gap (eV)**	**Experiment band-gap (eV)**
ZnO	wurzite	0.61 [LDA] [70]	3.25 [22]
ZnO	wurzite	2.7 [LDA+ASIC]	3.25 [22]
GaN	wurzite	2.2 [LDA] [70]	3.15 [23]
GaN	wurzite	3.0 [LDA+ASIC]	3.15 [23]
AlN	wurzite	4.16 [LDA] [70]	6.1 [23]
AlN	wurzite	5.72 [LDA+ASIC]	6.1 [23]

Table 6.2: Materials, bulk crystal structure and its calculated and experiment band-gaps. The method used in band-gap calculations are written in square-bracket. LDA stands for local density approximations, whereas ASIC, stands for atomic self-interaction correction.

transport supporting-point in the first Brillouin zones.

Our 2D decay plot analysis suggests that ZnO has a minimum decay rate of 1.14 $\AA^{-1}$ at the Γ-point (see in Figure 6.7). Since ZnO has a minimum Bloch wave-function amplitude decay rate at the Γ-point (see in table 6.3), it means that the Bloch wave-functions, which tunnels through the Γ-point has a higher probability to reach the right-side electrode than the one which tunnels through the other-points in the Brillouin zone. Therefore, we conclude that ZnO supports the Γ-point driven transport (see in table 6.3). Most of the current originates from electrons tunnelling at the Γ-point.

GaN and bulk wurzite AlN have a minimum Bloch wave-function amplitude decay rate of $1.04\AA^{-1}$ (see in Figure 6.8) and of $1.98\AA^{-1}$ (see in Figure 6.9) (see in table 6.3). These are respectively located at the Γ, K and M-points in the first 2D hexagonal Brillouin zone. Planar AlN have minimum decay rate $2.4\AA^{-1}$ at the Γ-point, and $2.9\AA^{-1}$ at the K and M-points (see in table 6.3). We have then performed a complex-band analysis of ZnO in order to understand its symmetry filtering ability at the transport supporting-point. Our

Material	**Transport supporting points in $2d(k_x, k_y)$ first Brillouin zone**	**Minimum Bloch wave-function amplitude decay rate ($\mathrm{\AA}^{-1}$), at the transport supporting point with $\mathrm{E_F} = 0$**	**Maximum Bloch wave-function amplitude decay rate ($\mathrm{\AA}^{-1}$), at the transport supporting point with $\mathrm{E_F} = 0$**
Bulk-ZnO	Γ	1.14	2.83
Planar-ZnO	Γ	1.52	2.44
Bulk-GaN	Γ, K, M	1.04	3.63
Bulk-AlN	Γ, K, M	1.98	4.19
Planar-AlN	Γ	2.4	3.97
Planar-AlN	K, M	2.9	3.97

Table 6.3: Materials transport supporting points in the $2d(k_x, k_y)$ first Brillouin zones. The Bloch wave-function amplitude decay rate ($\mathrm{\AA}^{-1}$), at the transport supporting points have been evaluated at the Fermi energy ($\mathrm{E} - \mathrm{E_F} = 0$).

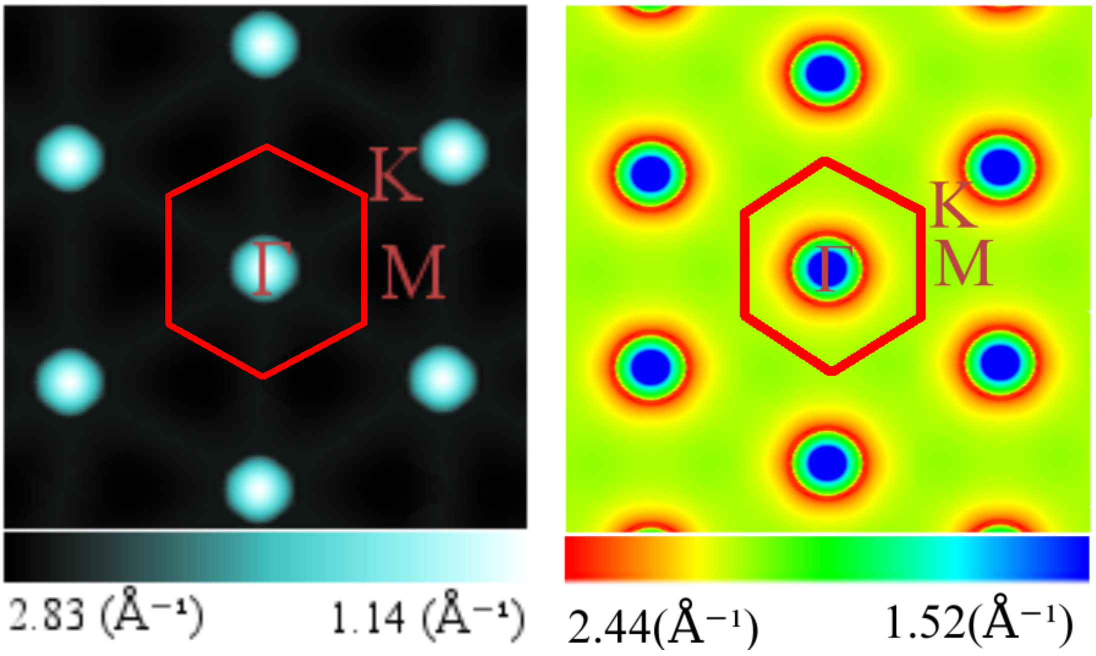

Figure 6.7: Left: 2D (k_x, k_y) decay plot of the Bloch wave-function of bulk wurzite ZnO in the first Brillouin zone. ZnO has minimum Bloch wave-function amplitude decay rate of $1.14\mathring{A}^{-1}$ at the Γ-point. The maximum is $2.83\mathring{A}^{-1}$. Right: 2D (k_x, k_y) decay plot of the Bloch wave-function of planar ZnO in the first Brillouin zone. Planar ZnO has minimum Bloch wave-function amplitude decay rate of $1.52\mathring{A}^{-1}$ at the Γ-point. The maximum is $2.44\mathring{A}^{-1}$. The color code representing k in the (k_x, k_y) plot varies linearly from the lowest decay rate to the highest decay rate. The transmission has been evaluated when the Fermi energy level of the ZnO is in the middle of the band-gap $(\mathrm{E} - \mathrm{E_F} = 0)$.

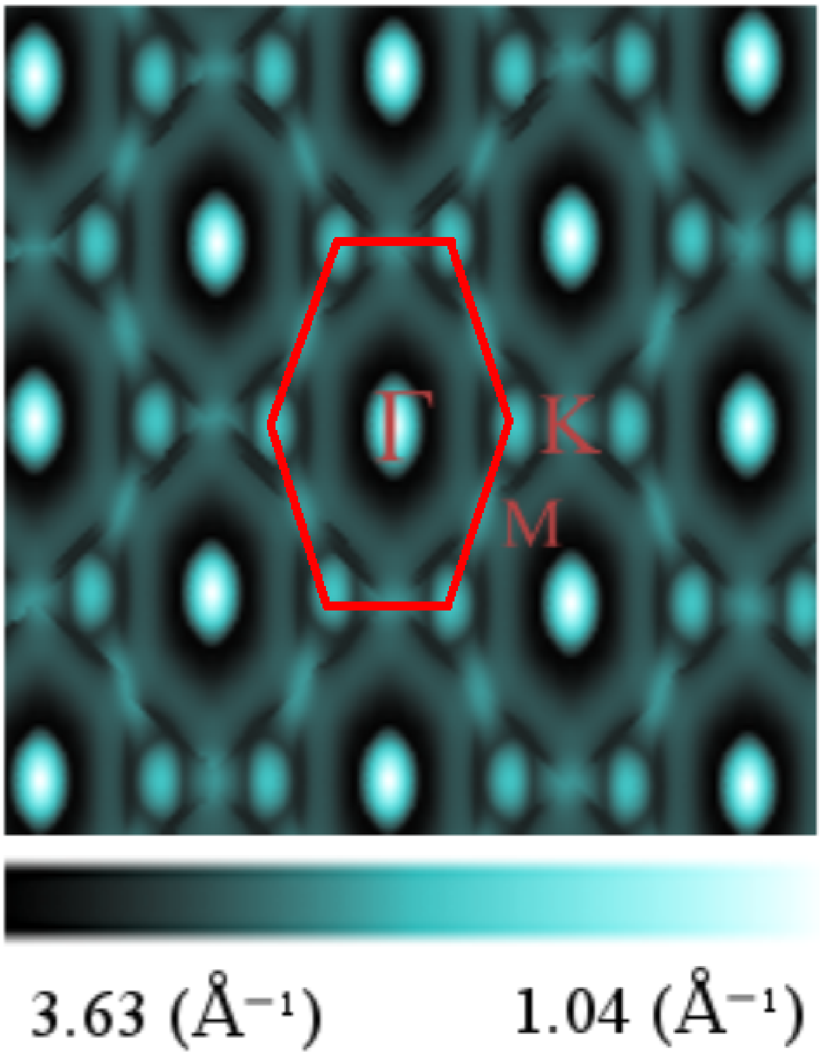

Figure 6.8: 2D (k_x, k_y) decay plot of the Bloch wave-function of GaN in the first Brillouin zone. GaN has a minimum decay rate of $1.04\mathring{A}^{-1}$ at the Γ, K and M-points, whereas the maximum decay rate is $3.64\mathring{A}^{-1}$. The color code representing k in the (k_x, k_y) plot varies linearly from the lowest decay rate to the highest decay rate. The transmission has been evaluated when the Fermi energy level of the GaN is in the middle of the band-gap $(\mathrm{E} - \mathrm{E_F} = 0)$.

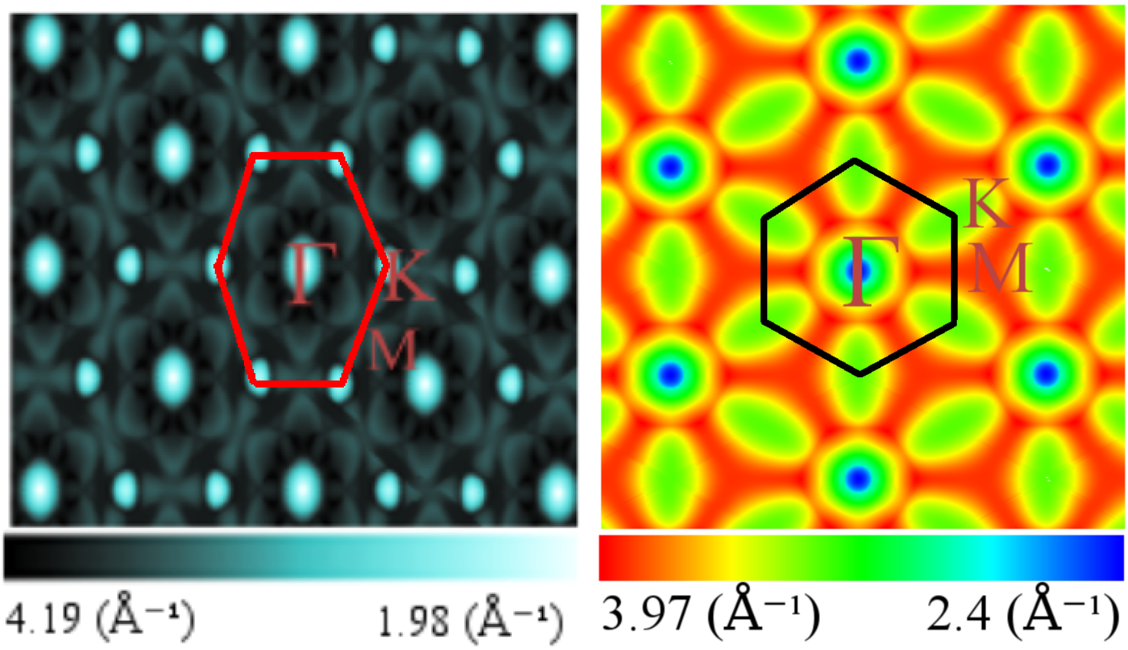

Figure 6.9: Left: 2D (k_x, k_y) decay plot of the Bloch wave-function of bulk wurzite AlN in the first Brillouin zone. AlN has a minimum decay rate of $1.98\mathring{A}^{-1}$ at the Γ, K and M-points, whereas the maximum decay rate is $4.19\mathring{A}^{-1}$. Right: 2D (k_x, k_y) decay plot of the Bloch wave-function of planar AlN in first Brillouin zone. Planar AlN has a minimum decay rate of $2.4\mathring{A}^{-1}$ at the Γ-point, whereas the maximum decay rate is $3.97\mathring{A}^{-1}$. The color code representing k in the (k_x, k_y) plot varies linearly from the lowest decay rate to the highest decay rate. The transmission has been evaluated when the Fermi energy level of the AlN is in the middle of the band-gap $(\mathrm{E} - \mathrm{E_F} = 0)$.

Material	**Transport supporting point**	**Symmetry filtering at the transport supporting point**
ZnO	Γ	Δ_1
GaN	Γ, K, M	Δ_1, Δ_1, Δ_1
AlN	Γ, K, M	Δ_1, Δ_1, Δ_1

Table 6.4: Material and its transport supporting points in $2d$ (k_x, k_y)- first Brillouin zone, and symmetry filtering at the transport supporting points. In ZnO, transmission occurs mainly around the Γ-point of the first Brillouin zone. In GaN and AlN transmission mainly driven by the Γ, K and M points. ZnO filters the Δ_1 symmetry of the Bloch state at the Γ point, whereas GaN, and AlN filters the Δ_1 symmetry of the Bloch state at the Γ, K and M points. In all cases the transport direction is along the z-axis.

complex-band analysis suggests that ZnO filters the Δ_1 symmetry (see in table 6.4) of the Bloch state at the Γ-point (see in Figure 6.10), if the transport is along the [001] direction. For GaN (see in Figure 6.11) and AlN (see in Figure 6.14) complex-band analysis suggests that they both filter the Δ_1 symmetry of the Bloch state at the Γ-point during transport along the [001] direction (see in table 6.4). We have performed similar complex-band analysis at K and M-points for GaN (see in Figure 6.12, 6.13) and for AlN (see in Figure 6.15, 6.16) as well. We found that both GaN and AlN filter the Δ_1 symmetry of the Bloch state at these-points (see in table 6.4). We have then performed band calculation of *bcc* iron and *bcc* cobalt along K to H (see in Figure 6.17) and along M to L (see in Figure 6.18) directions. Both *bcc* iron and *bcc* cobalt exhibit a $\Delta_{2'}$ symmetry of the Bloch state along K to H direction (see in table 6.5). Whereas along the M to L *bcc* cobalt supplies the Δ_1 and iron supplies the $\Delta_{2'}$ symmetry of the Bloch states (see in table 6.5).

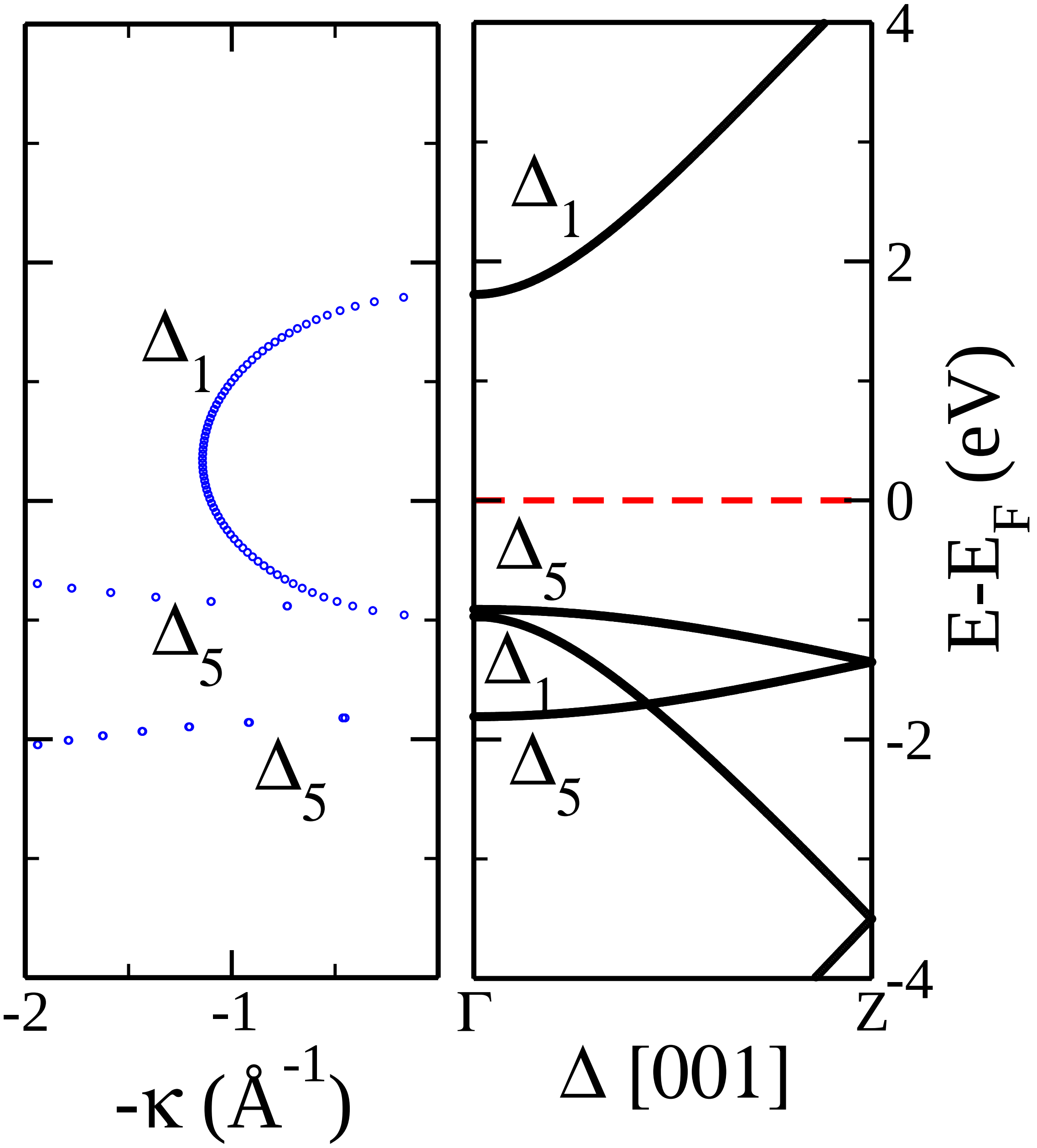

Figure 6.10: LDA+ASIC (atomic self-interaction correction) real (right-hand side panel) and complex-band (left-hand side panel) of ZnO along the transport direction. Our complex-band analysis suggests that the Δ_1 symmetry of the Bloch state has a minimum decay rate, κ, for transport along the [001] direction. The red dashed line denotes the Fermi level, $\mathrm{E_f} = 0$ eV.

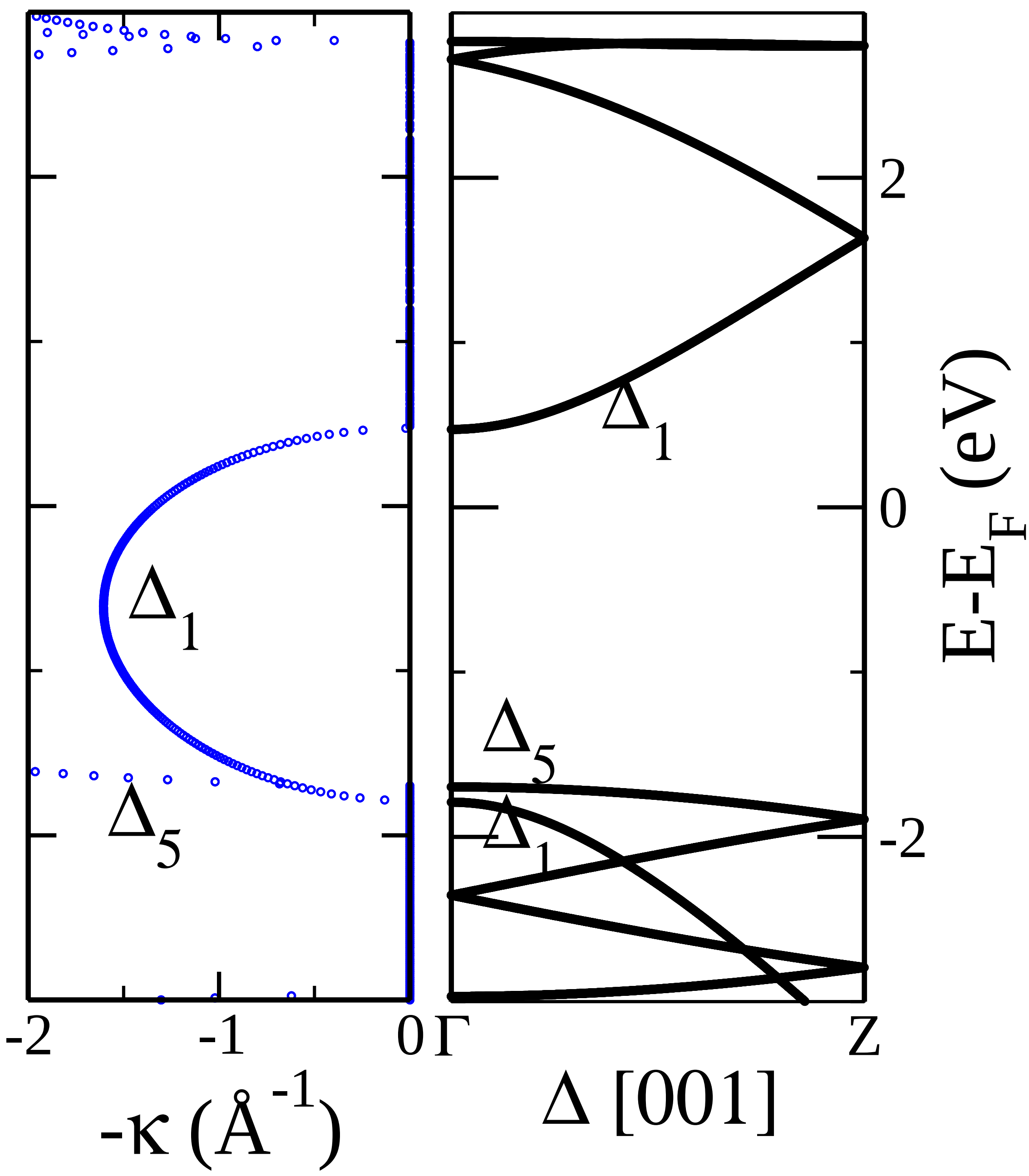

Figure 6.11: LDA real (right-hand side panel) and complex-band (left-hand side panel) of GaN at the Γ-point. Our complex-band analysis suggests that the Δ_1 symmetry of the Bloch state has a minimum decay rate, κ, for transport along the [001] direction.

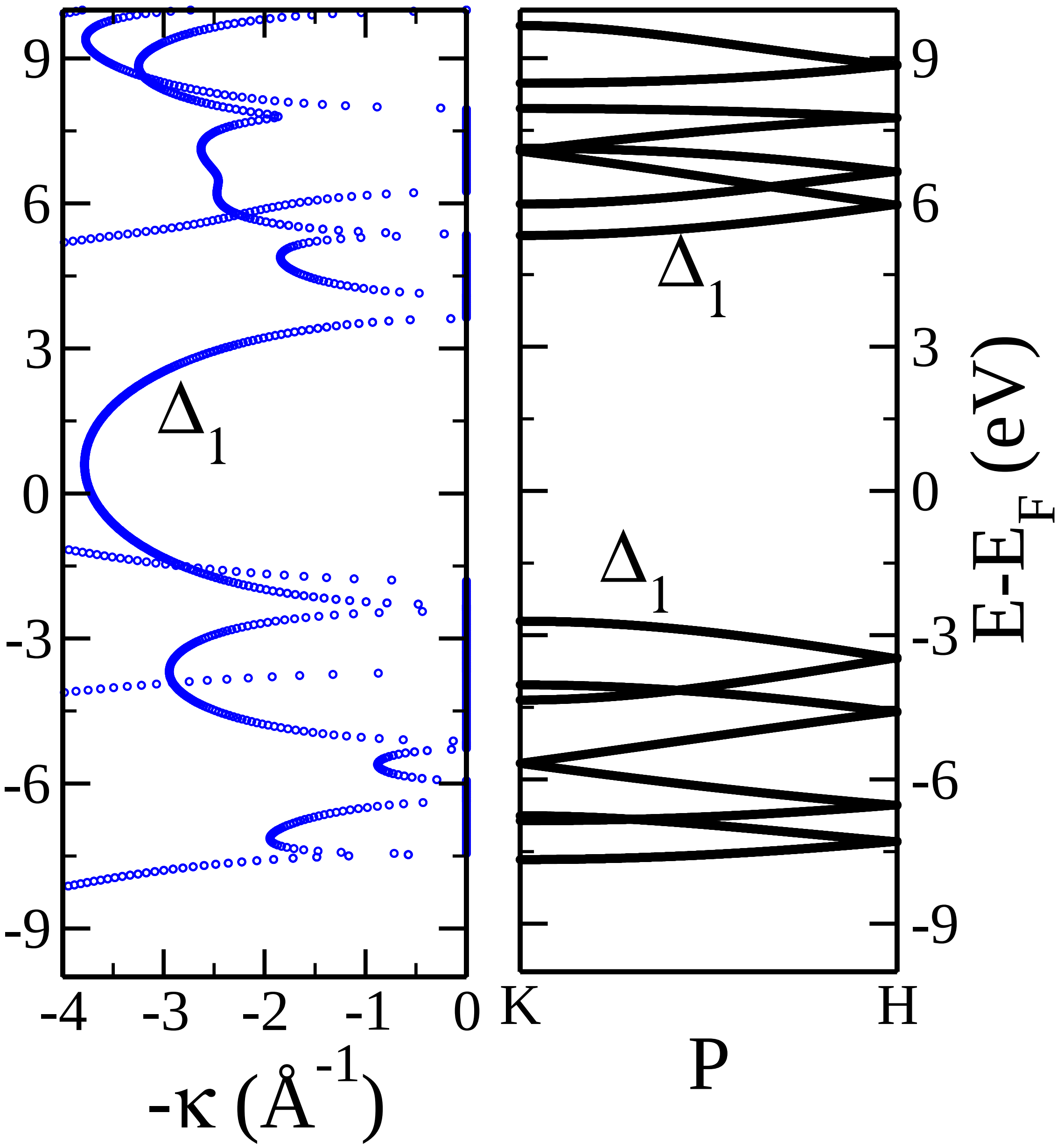

Figure 6.12: LDA real (right-hand side panel) and complex-band (left-hand side panel) of GaN at the K-point. Our complex-band analysis suggests that the Δ_1 symmetry of the Bloch state has a minimum decay rate, κ, for transport along the [001] direction.

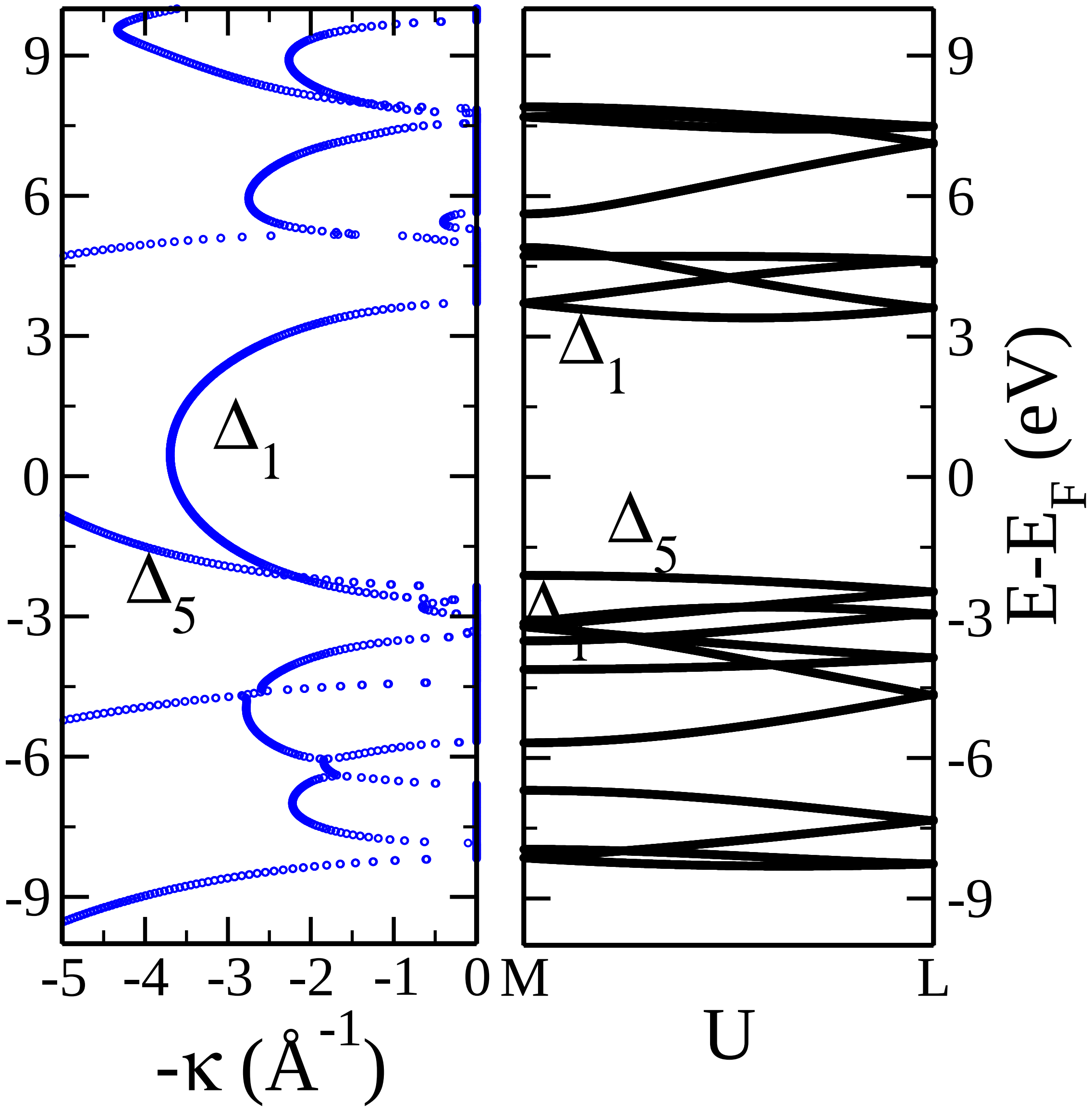

Figure 6.13: LDA real (right-hand side panel) and complex-band (left-hand side panel) of GaN at the M-point. Our complex-band analysis suggests that the Δ_1 symmetry of the Bloch state has a minimum decay rate, κ, for transport along the [001] direction.

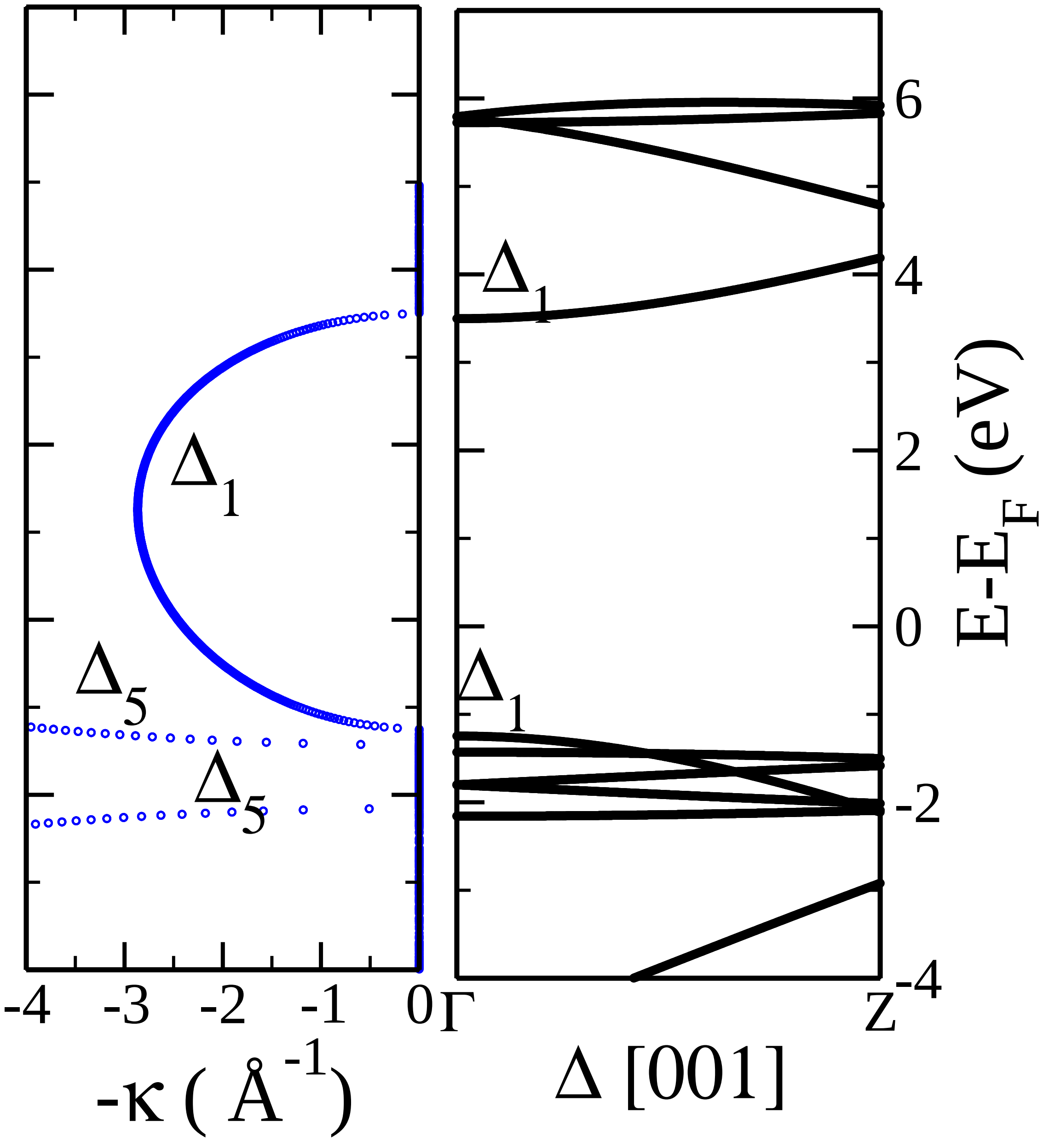

Figure 6.14: LDA real (right-hand side panel) and complex-band (left-hand side panel) of AlN at the Γ-point. Our complex-band analysis suggests that the Δ_1 symmetry of the Bloch state has a minimum decay rate, κ, for transport along the [001] direction.

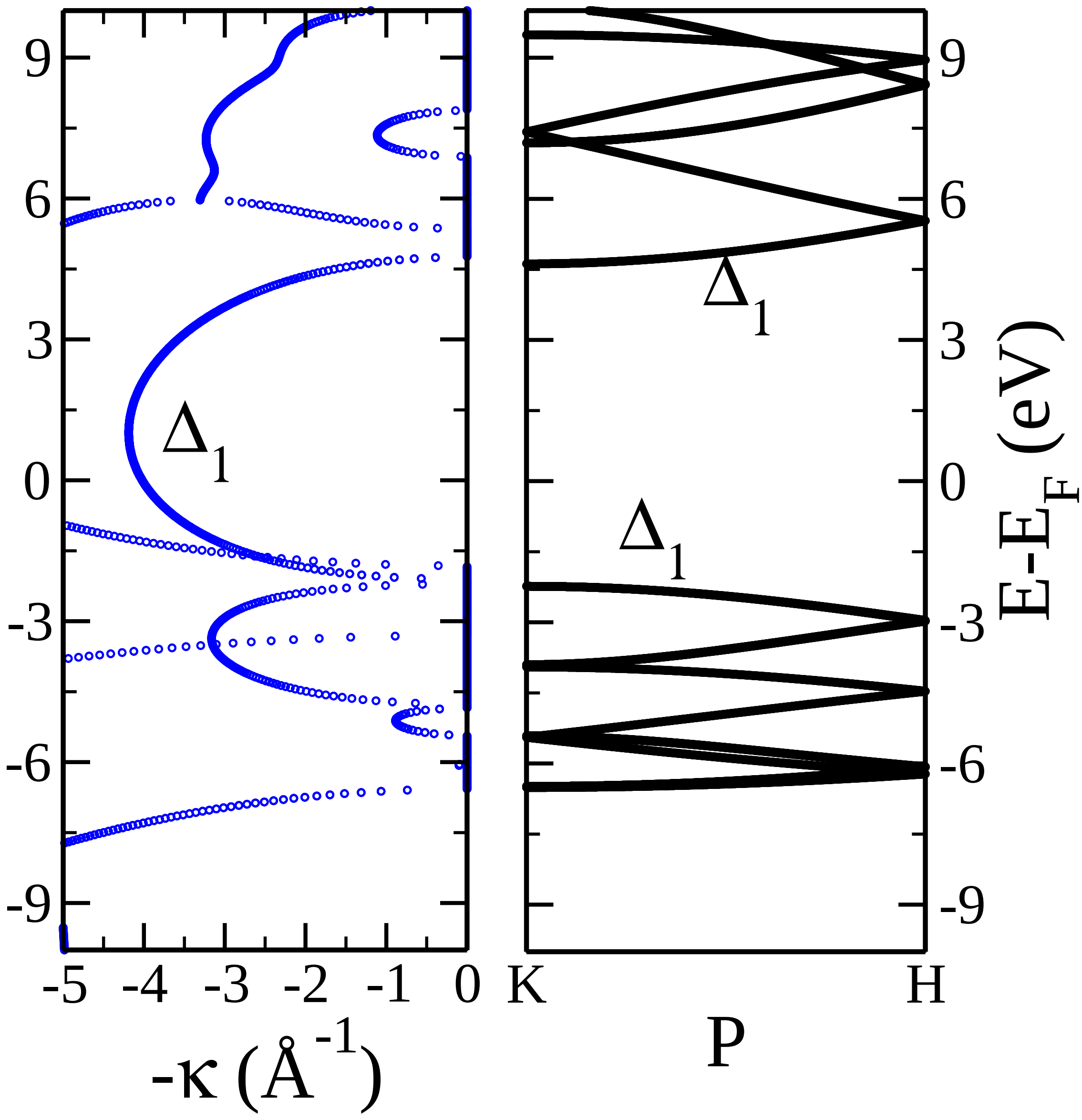

Figure 6.15: LDA real (right-hand side panel) and complex-band (left-hand side panel) of AlN at the *K*-point. Our complex-band analysis suggests that the Δ_1 symmetry of the Bloch state has a minimum decay rate, κ, for transport along the [001] direction.

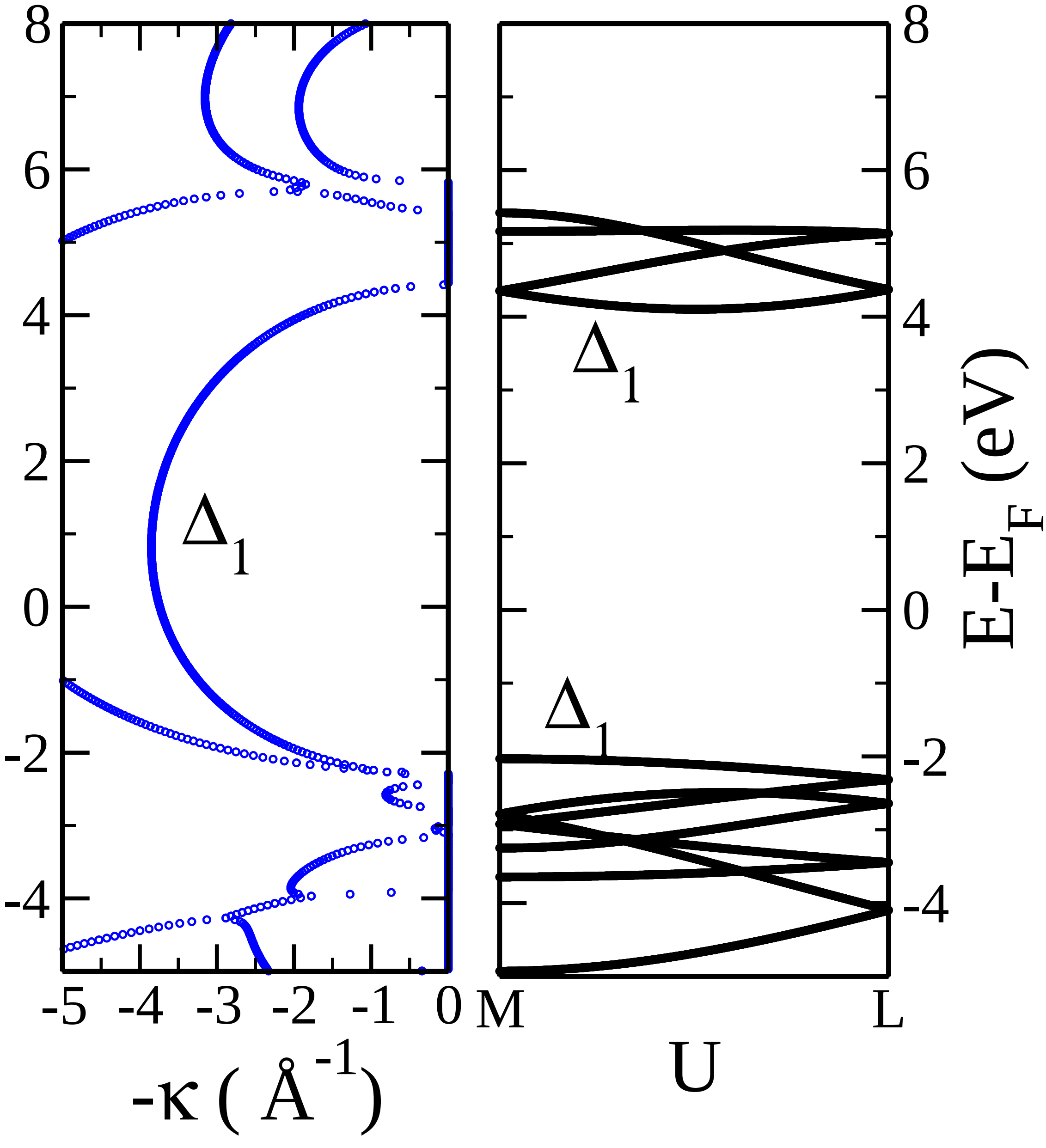

Figure 6.16: LDA real (right-hand side panel) and complex-band (left-hand side panel) of AlN at the M-point. Our complex-band analysis suggests that the Δ_1 symmetry of the Bloch state has a minimum decay rate, κ, for transport along the [001] direction.

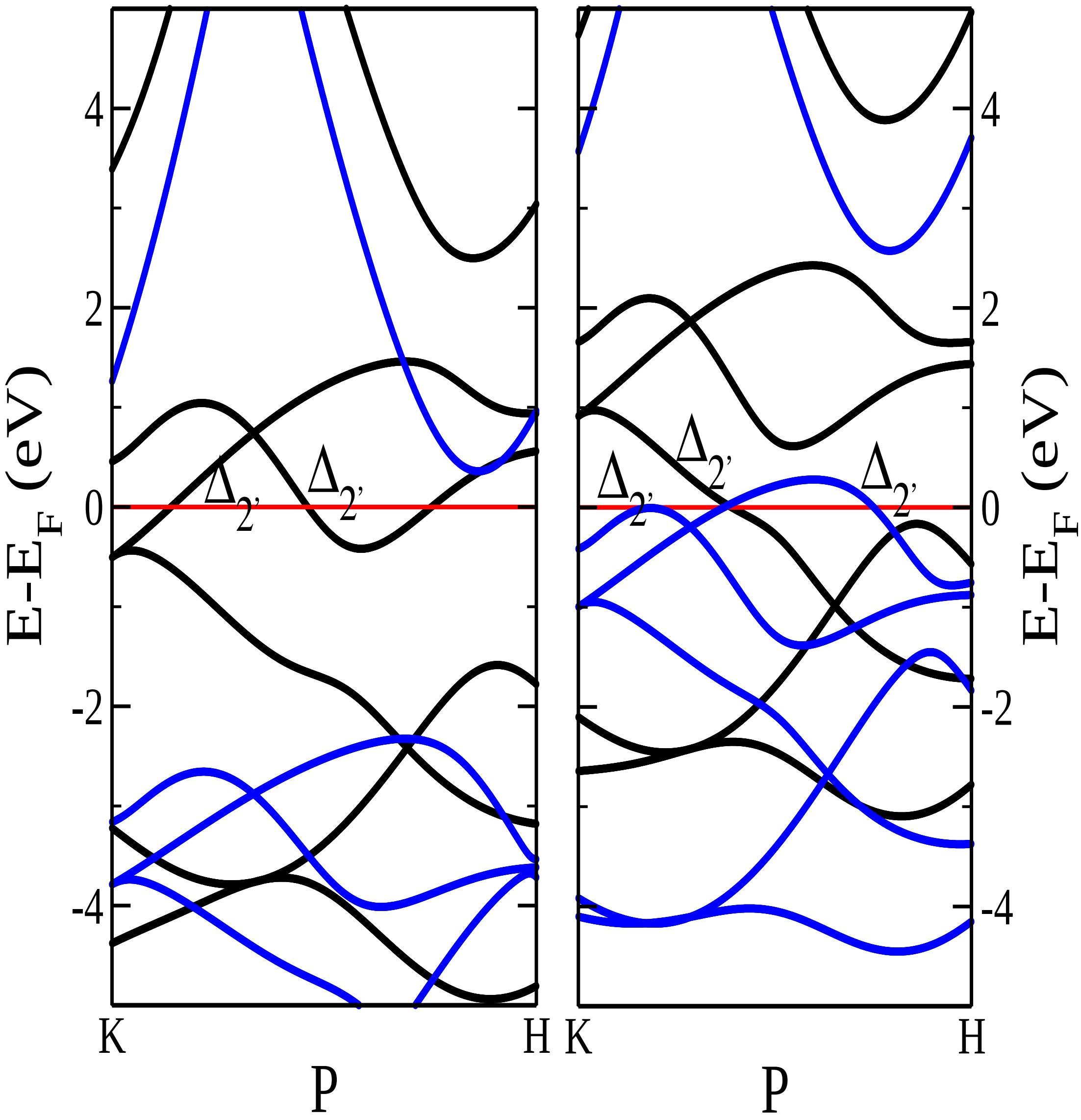

Figure 6.17: Left *bcc* cobalt and right *bcc* iron band structures along K to H direction. The K coordinates is $(\frac{4\pi}{3a}, 0, 0)$, whereas the H coordinate is $(\frac{4\pi}{3a} + \frac{\pi}{a}, \frac{\pi}{a}, \frac{\pi}{a})$. a is the lattice parameter of *bcc* iron and *bcc* cobalt, which in our case is $2.73\mathring{A}$. The red horizontal line in both figures is the Fermi energy level, $\mathrm{E_F}$. The blue curve in the figure is for spin up, whereas the black curve is for the spin down band.

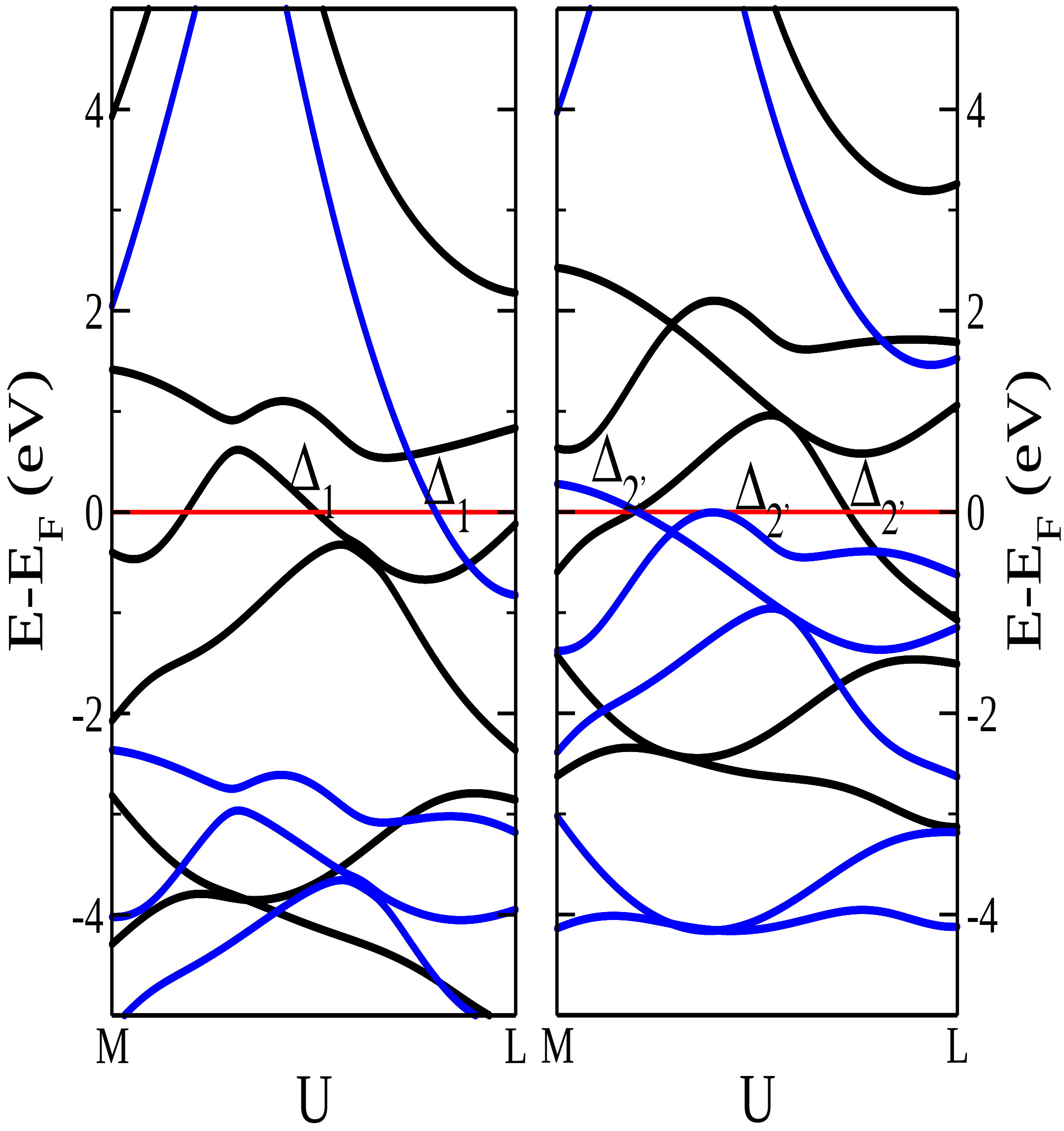

Figure 6.18: Left *bcc* cobalt and right *bcc* iron band structures along M to L direction. M has coordinates $(\frac{\pi}{a}, \frac{-\pi}{\sqrt{3}a}, 0)$, whereas L has coordinates $(\frac{\pi}{a} + \frac{\pi}{a}, \frac{(\sqrt{3}-1)\pi}{\sqrt{3}a}, \frac{\pi}{a})$. a is the lattice parameter of *bcc* cobalt and *bcc* iron, which in our case is $2.73 \mathring{A}$. The red horizontal line in both figures is the Fermi energy level, $\mathrm{E_F}$. The blue curve in the figure is for spin up, whereas the black curve is for the spin down band.

Ferromagnet	**Transport direction**	**Symmetry of the Bloch states available in the transport direction**
bcc-Co	$\Gamma - \mathrm{P}$	$\Delta_{1\uparrow},\ \Delta_{1\downarrow}$
bcc-Fe	$\Gamma - \mathrm{P}$	$\Delta_{1\uparrow},\ \Delta_{1\downarrow}$
bcc-Co	$\mathrm{K} - \mathrm{H}$	$\Delta_{2'\downarrow}$
bcc-Fe	$\mathrm{K} - \mathrm{H}$	$\Delta_{2'\uparrow},\ \Delta_{2'\downarrow}$
bcc-Co	$\mathrm{M} - \mathrm{L}$	$\Delta_{1\uparrow},\ \Delta_{1\downarrow}$
bcc-Fe	$\mathrm{M} - \mathrm{L}$	$\Delta_{2'\uparrow},\ \Delta_{2'\downarrow}$

Table 6.5: *bcc*-Fe and *bcc*-Co both supply spin-up and spin-down Δ_1 symmetry of the Bloch state along $\Gamma - \mathrm{P}$ direction. *bcc*-Co supplies spin-down $\Delta_{2'}$ symmetry of the Bloch state along $\mathrm{K} - \mathrm{H}$ direction, whereas *bcc*-Fe supplies both spin-up and spin-down $\Delta_{2'}$ symmetry of the Bloch states. *bcc*-Co supplies both spin-up and spin-down Δ_1 symmetry of the Bloch state along $\mathrm{M} - \mathrm{L}$ direction, whereas *bcc*-Fe supplies both spin-up and spin-down $\Delta_{2'}$ symmetry of the Bloch state along the same direction.

6.5 Siesta-Smeagol set up for the display materials

We perform transport analysis for MTJs with eleven unit cells of ZnO, nine unit cells of GaN, and nine unit cells of AlN as insulator. We then have performed Siesta calculations using the LDA +ASIC functional with a $10 \times 10 \times 1$ Monkhorst k-space grids and 700 Rydberg real space mesh grid cut-off for ZnO, $6 \times 6 \times 1$ Monkhorst k-space grids and 700 Rydberg real space mesh grid cut-off for GaN and AlN semiconductors. We use the Siesta converged density matrix as a starting density matrix for the Smeagol calculation with same k-grid spacing. We then have performed Smeagol calculations for the same grid size and used the output converged density matrix as a final density for a dense k-point mesh ($50 \times 50 \times 1$) calculation for all three MTJs.

6.6 Results and Discussion

The tunnelling magneto-resistance of a MTJ is defined as $\frac{T_P - T_{Ap}}{T_{Ap}}$, where T_P is the combined transmission of both spin channels of the ferromagnetic electrodes when the magnetic moments are parallel to each other. In contrast T_{Ap} is the transmission when the magnetic moments of the ferromagnetic electrodes are anti-parallel to each other. Linear response (zero bias) for the Fe(Co)|ZnO|Fe(Co) junction suggests that the Co-based MTJs has $\sim$ 45% TMR, whereas the Fe-based has $\sim$ 69.2% TMR (see in Figure 6.19) (see in table 6.6). The transmission analysis for the Fe(Co)|ZnO|Fe(Co) junction (see in Figure 6.19) suggests that at zero bias the common Fermi energy level of the junction is in the conduction band of ZnO (see in table 6.6). In other words, the Co(Fe)|ZnO|Co(Fe) junction behaves like a metallic junction and not like a MTJ (see in table 6.6). In order to verify this we have performed a band off-set calculation for the Co(Fe)|ZnO|Co(Fe) junction. Our band off-set calculations for the Co|ZnO|Co (see in Figure 6.20) and Fe|ZnO|Fe junctions (see in Figure 6.21) confirms that the common Fermi level is in the conduction

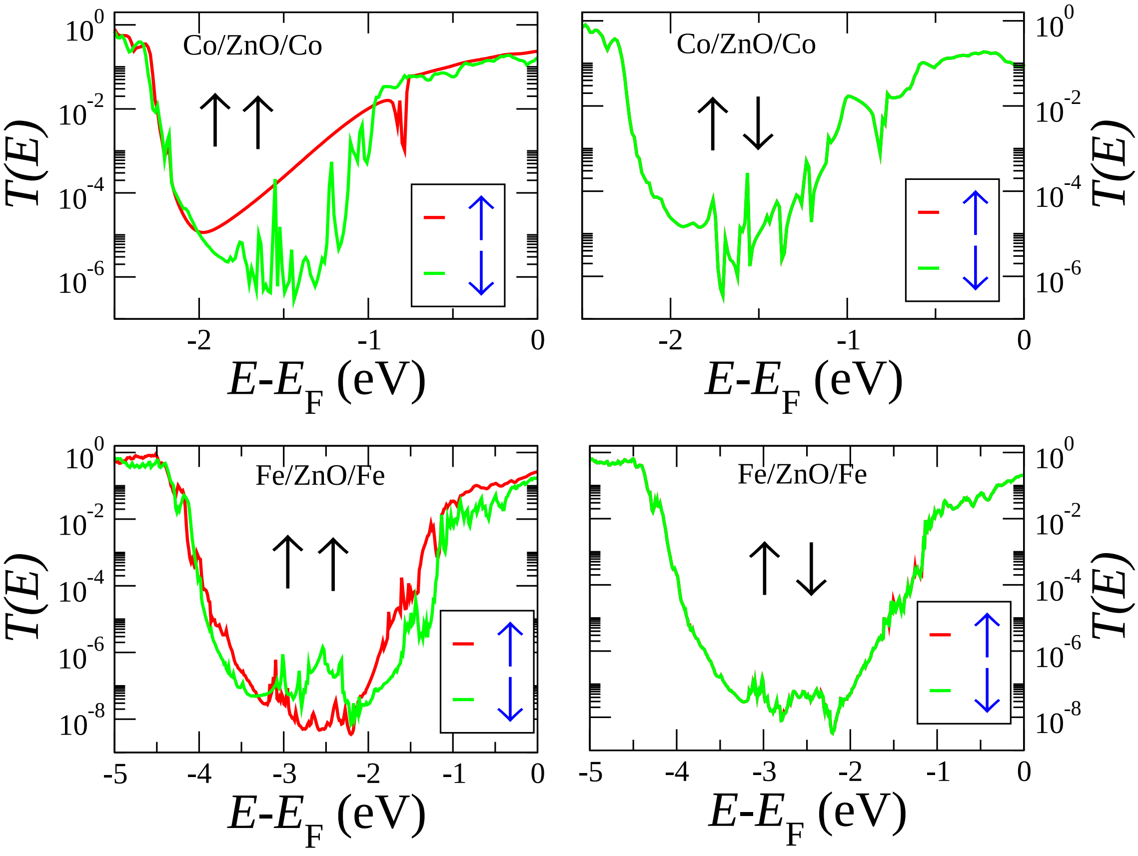

Figure 6.19: Transmission analysis of Co|ZnO|Co and Fe|ZnO|Fe MTJs in the parallel and anti-parallel configurations of the ferromagnetic electrodes.

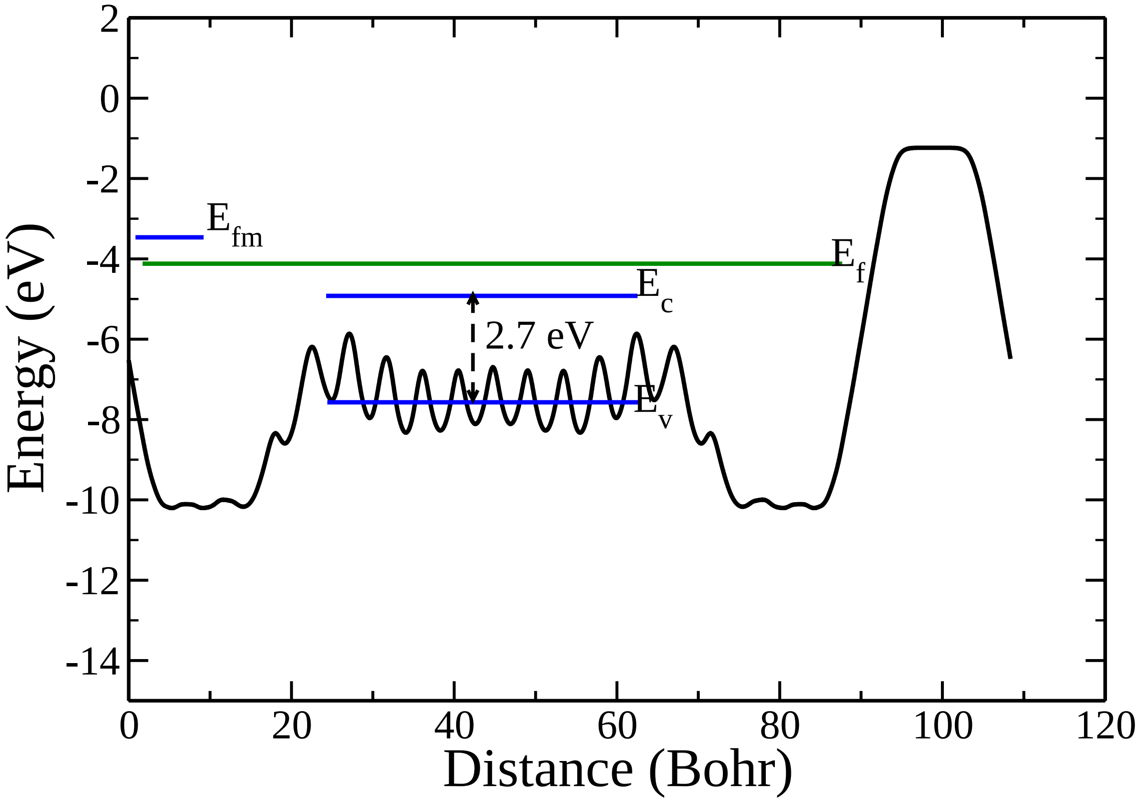

Figure 6.20: Co|ZnO|Co junction bands off-set. E_{fm} is the chemical potential of the cobalt electrodes. E_f is the common Fermi energy level of the entire junction. E_v is the valence band maximum and E_c is the conduction band minimum of ZnO. The continuous oscillatory curve, which starts at the origin and ends at around 110 Bohr, is the macroscopic average of the Hartree potential energy of electron in the Co|ZnO|Co junction.

band of ZnO for both junctions and the entire MTJ behaves like a metal (see in table 6.6).

As for as GaN MTJs is concerned, linear response transport (zero bias) (see in Figure 6.22) suggests that the Fe and Co-based MTJs have $\sim 29\%$ and $\sim 30\%$ TMR respectively (see in table 6.6). Our transmission analysis of Fe(Co)|GaN|Fe(Co) junctions (see in Figure 6.22) indicates that at zero bias the common Fermi energy level is close to but not within the conduction band (see in table 6.6). In other words, the whole junction is close to behave like a metal but it is still insulating (see in table 6.6). In order to verify this claim we have performed a band off-set (see in Figure 6.23) calculation for the Co|GaN|Co junction and found that this is indeed the case. Finally, let us take a look at the AlN-based MTJs. Linear response (zero bias) transport for the Fe(Co)|AlN|Fe(Co) junction

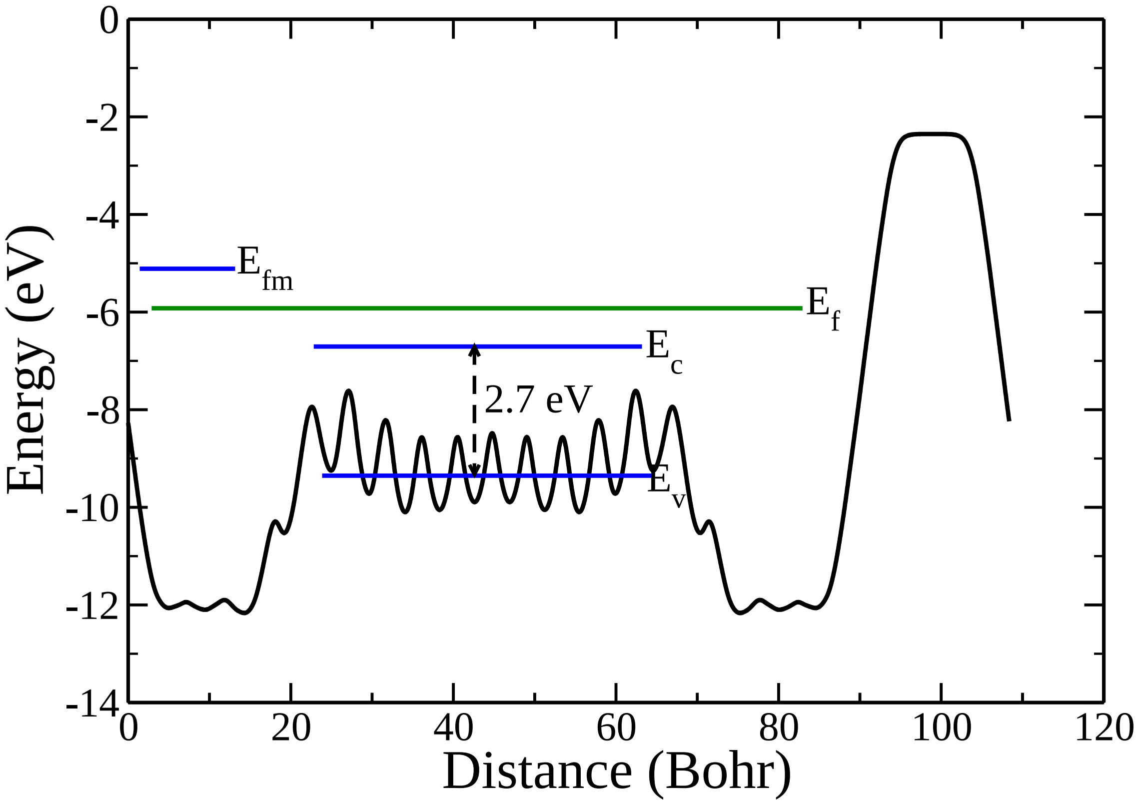

Figure 6.21: Fe|ZnO|Fe junction bands off-set. E_{fm} is the chemical potential of the iron electrodes. E_f is the common Fermi energy level of the entire junction. E_v is the valence band maximum and E_c is the conduction band minimum of ZnO. The continuous oscillatory curve, which starts at the origin and ends at around 110 Bohr, is the macroscopic average of the Hartree potential energy of electron in the Fe|ZnO|Fe junction.

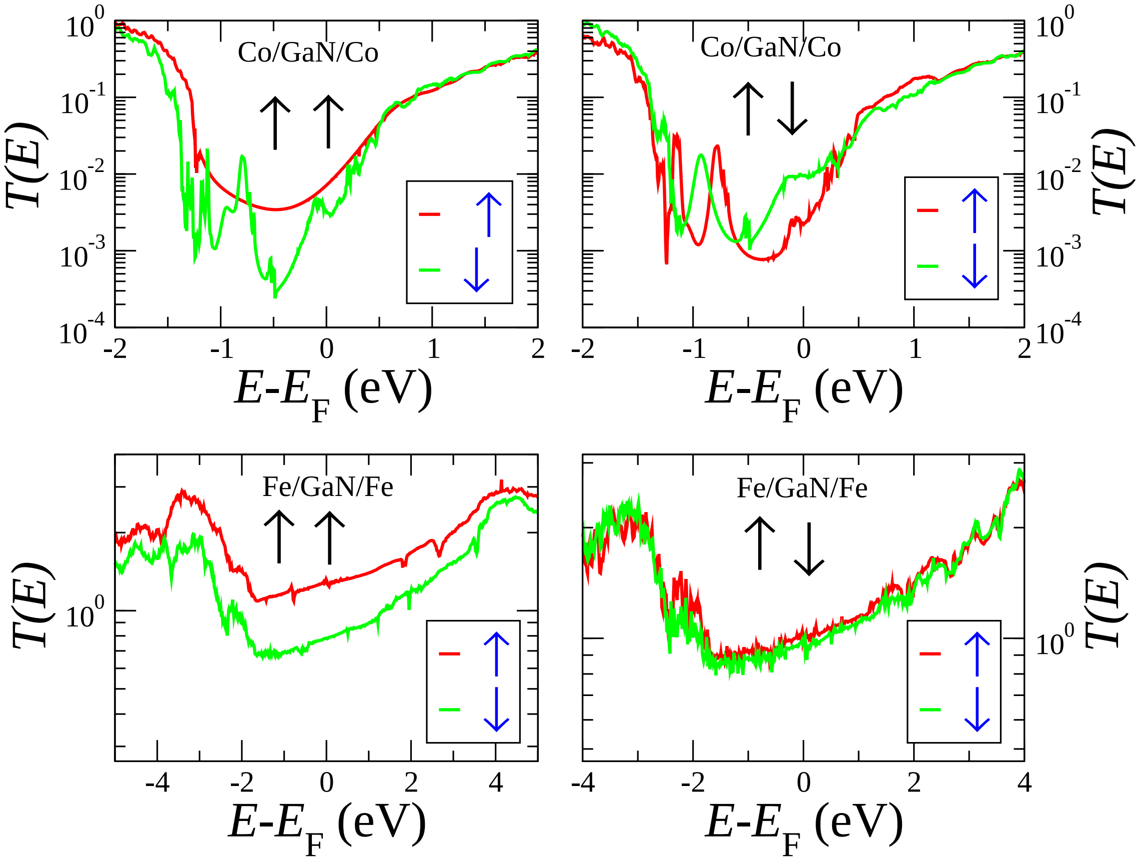

Figure 6.22: Transmission analysis of Co|GaN|Co and Fe|GaN|Fe based MTJs in the parallel and anti-parallel configurations of the ferromagnetic electrodes.

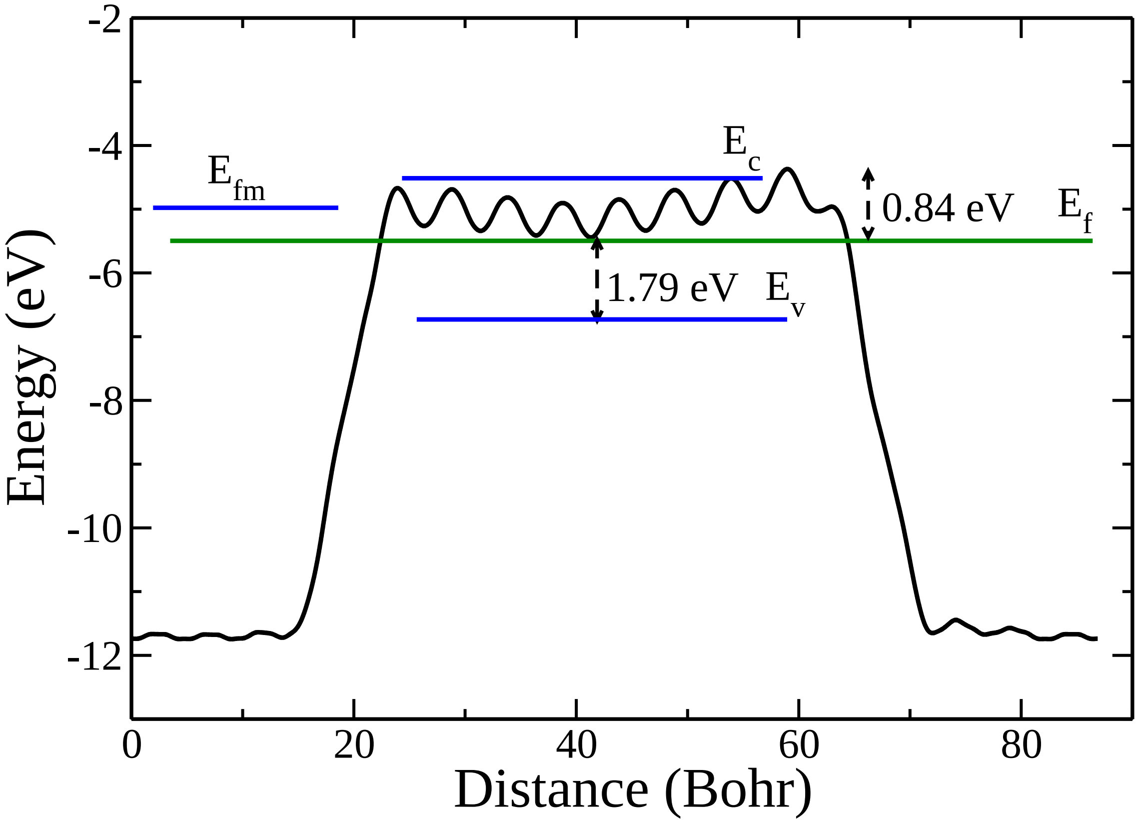

Figure 6.23: Co|GaN|Co junction bands off-set. E_{fm} is the chemical potential of the cobalt electrodes. E_f is the common Fermi energy level of the entire junction. E_v is the valence band maximum and E_c is the conduction band minimum of GaN. The continuous oscillatory curve, which starts at the origin and ends at around 85 Bohr, is the macroscopic average of the Hartree potential energy of electron in the Co|GaN|Co junction.

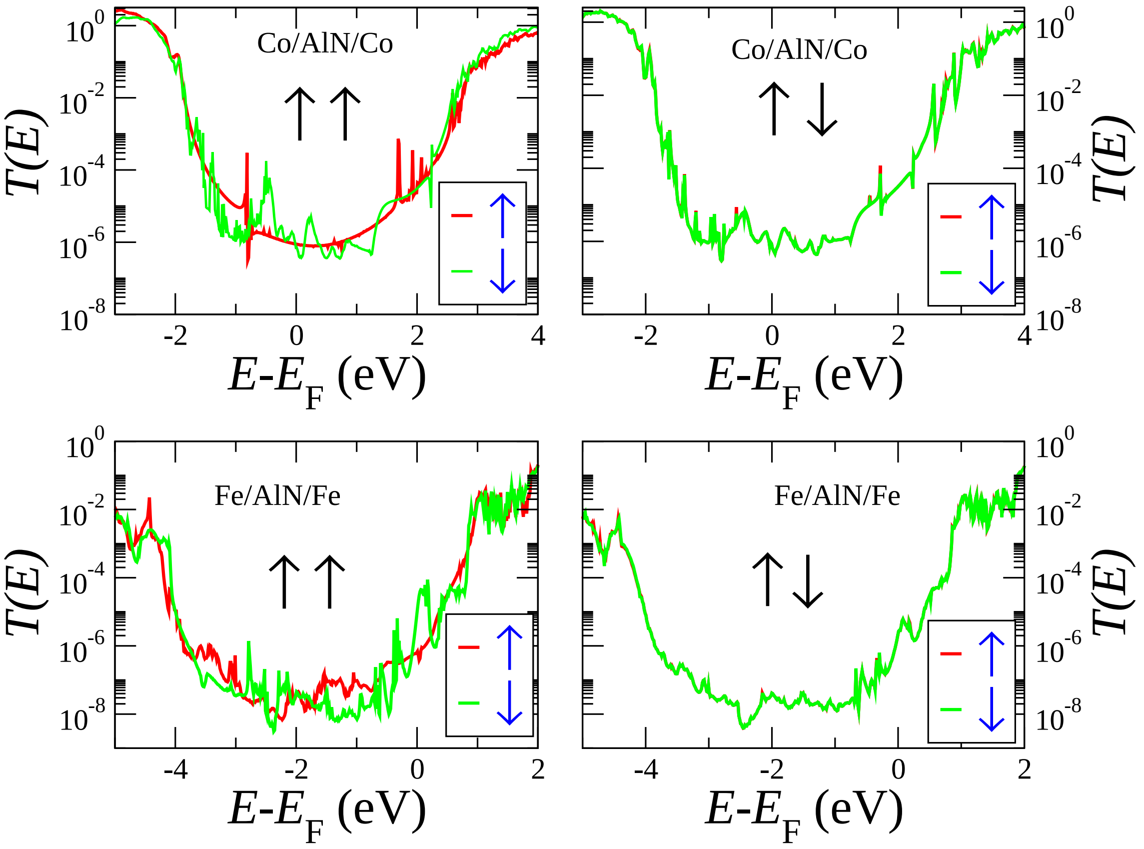

Figure 6.24: Transmission analysis of Co|AlN|Co and Fe|AlN|Fe based MTJs in the parallel and anti-parallel configurations of the ferromagnetic electrodes.

(see in Figure 6.24) suggests that Fe and Co-based MTJs have $\sim 20.4\%$ and $\sim 47\%$ TMR respectively (see in table 6.6). Our transmission analysis of the Co(Fe)|AlN|Co(Fe) junction (see in Figure 6.24) indicates that at zero bias the common Fermi energy level of the junction is in the middle of the band gap of AlN. In this case the junction is perfectly insulating (see in table 6.6). We have also performed band off-set (see in Figures 6.25, 6.26) calculations of Co(Fe)|AlN|Co(Fe) junction and found that the junctions are indeed perfectly insulating (see in table 6.6).

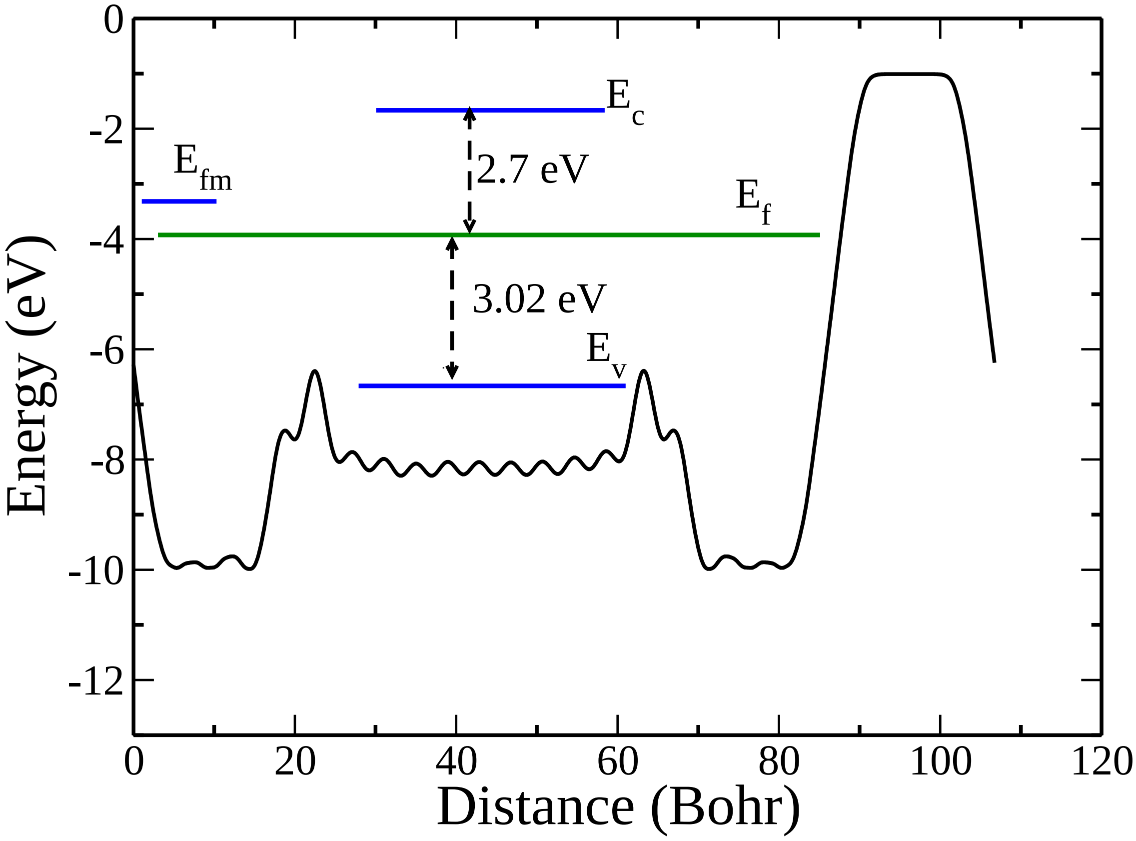

Figure 6.25: Co|AlN|Co junction bands off-set. E_{fm} is the chemical potential of the iron electrodes. E_f is the common Fermi energy level of the entire junction. E_v is the valence band maximum and E_c is the conduction band minimum of AlN. The continuous oscillatory curve, which starts at the origin and ends at around 110 Bohr, is the macroscopic average of the Hartree potential energy of electron in the Co|AlN|Co junction.

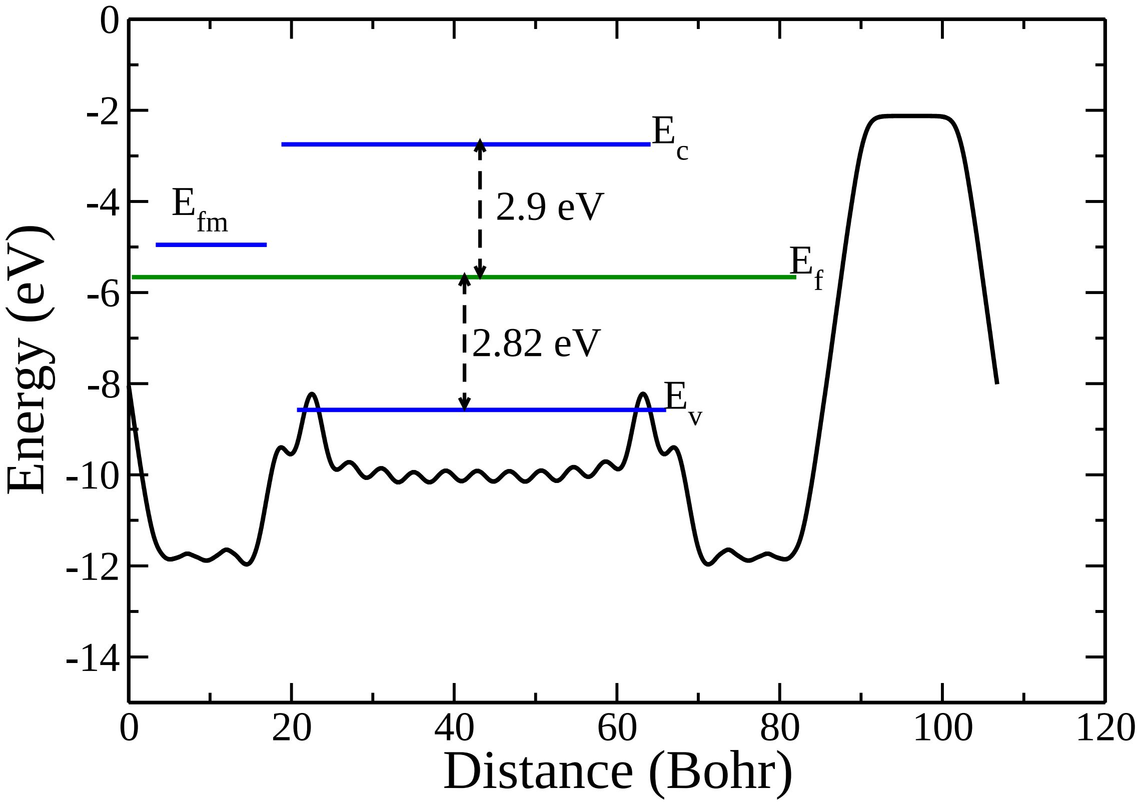

Figure 6.26: Fe|AlN|Fe junction bands off-set. E_{fm} is the chemical potential of the iron electrodes. E_f is the common Fermi energy level of the entire junction. E_v is the valence band maximum and E_c is the conduction band minimum of AlN. The continuous oscillatory curve, which starts at the origin and ends at around 110 Bohr, is the macroscopic average of the Hartree potential energy of electron in the Fe|AlN|Fe junction.

Junction	**Junction-state**	**Transport supporting point**	**Symmetry of the Bloch state is filtered at the transport supporting point**	**TMR %**
Co|ZnO|Co	metallic	Γ	Δ_1	~ 45
Fe|ZnO|Fe	metallic	Γ	Δ_1	~ 69.2
Co|GaN|Co	insulator	$\Gamma,\ \mathrm{K},\ \mathrm{M}$	$\Delta_1,\ \Delta_1,\ \Delta_1$	~ 30
Fe|GaN|Fe	insulator	$\Gamma,\ \mathrm{K},\ \mathrm{M}$	$\Delta_1,\ \Delta_1,\ \Delta_1$	~ 29
Co|AlN|Co	perfect-insulator	$\Gamma,\ \mathrm{K},\ \mathrm{M}$	$\Delta_1,\ \Delta_1,\ \Delta_1$	~ 47
Fe|AlN|Fe	perfect-insulator	$\Gamma,\ \mathrm{K},\ \mathrm{M}$	$\Delta_1,\ \Delta_1,\ \Delta_1$	~ 20.4

Table 6.6: A ZnO based magnetic tunnel junction is metallic. Transmission in ZnO is mostly Γ-point driven and the Δ_1 symmetry of Bloch state is filtered at the Γ-point. the TMR of a ZnO based magnetic tunnel-junction with *bcc*-Co and *bcc*-Fe as ferromagnetic electrodes is $\sim 45-62\%$. A GaN based magnetic tunnel junction is an insulator, however they are very close to becoming metallic. The common Fermi energy of junction is very close (0.84 eV) to the conduction band minimum of GaN. Transmission in GaN is mostly driven by Γ, K and M-points, and the Δ_1 symmetry of Bloch states is filtered at these points. The TMR of a GaN based magnetic tunnel-junction with *bcc*-Fe and *bcc*-Co as ferromagnetic electrodes is $\sim 29-30\%$. An AlN based magnetic tunnel junction is a perfect-insulator. The common Fermi energy of the junction is in the middle of the band-gap of AlN. Transmission in AlN is mostly driven by Γ, K and M-points, and the Δ_1 symmetry of Bloch states is filtered at these points. The TMR in an AlN based magnetic tunnel-junction with *bcc*-Fe and *bcc*-Co as ferromagnetic electrodes is $\sim 20-47\%$.

6.7 Conclusion

We have performed a TMR analysis of ZnO, AlN and GaN as insulating spacers in magnetic tunnel junctions (MTJ). We have shown that all these semiconductor materials are filtering the Δ_1 symmetry of the Bloch state at the Γ, K and M-point in the first 2D hexagonal Brillouin zone. Conventional ferromagnets like Fe and Co supply both majority and minority spin electrons at the Fermi level with Δ_1 symmetry in the transport direction [001]. Therefore, the TMR in these semiconductor (SC) materials has turned out to be low. We have also calculated the work function of *compressed bcc* iron and *bcc* cobalt. We have found that the *compressed bcc* iron work function does not vary significantly with respect to that of bulk *bcc* iron. However, *compressed bcc* cobalt becomes more reactive than the bulk *hcp* cobalt by $\sim$ 1.2eV (the work-function reduce by $\sim$ 1.2 eV). We have also calculated the band off-set for Co(Fe)|ZnO|Co(Fe), Co(Fe)|AlN|Co(Fe) and Co(Fe)|GaN|Co(Fe) junctions. Our band off-set calculation suggests that the Co(Fe)|ZnO|Co(Fe) junction is metallic, the Co(Fe)|GaN|Co(Fe) one is in close to be metallic, while Co(Fe)|AlN|Co(Fe) remains insulating. The low TMR in all the Fe(Co)|ZnO|Fe(Co), Fe(Co)|GaN|Fe(Co), Fe(Co)|AlN|Fe(Co) junctions have been explained using the symmetry filtering mechanism of the Bloch states. Since *bcc* iron and *bcc* cobalt supply both spins (spin-up and spin-down) with Δ_1 symmetry along the transport direction, spin filtering in these junctions is low. In order to achieve higher TMR in these semiconductors we need to find an alternative ferromagnet electrode, which can supply only one spin with Δ_1 symmetry along the [001] transport direction. This should also be grown epitaxially on the display SC materials. Since these SC materials are the backbone of the display and the optoelectronic industries it is imperative to search for an alternative ferromagnetic electrode to generate largely spin-polarised currents, which can be used in the display industries for the lighting purposes. Also a new device structure can be realised, where one layer of these display materials (ZnO, AlN, GaN) act as spacer to filter the spin-polarized current, whereas another layer of these semiconductors (ZnO, GaN, AlN) act as a light emitters for spin-polarised light that can be used in quantum computing and for manipulating quantum bits.

.

Chapter 7

Conclusion and future work

We have designed and investigated a number of MTJs as potential elements of future non-volatile memories. These include Fe|HfO_2|Fe, Co|SiO_2|Co, Fe(Co)|ZnO|Fe(Co), Fe(Co)|GaN|Fe(Co) and Fe(Co)|AlN|Fe(Co). In chapter one, we first discussed the giant magneto-resistance and its two types, current in-plane (CIP), and current perpendicular-to-plane (CPP) based GMR devices. We then discussed tunnelling magneto-resistance based MTJs and its working principle. We first discussed about the Julliere model and its applicability to the amorphous tunnel barrier when incoherent tunnelling current dominates the transport. We then discussed the symmetry filtering model, applicable to crystalline tunnel barriers when coherent tunnelling current plays a dominant role and the phase of the wave-function remains preserved during tunnelling. We then discussed the requirement for an alternative to Fe|MgO|Fe magnetic tunnel-junction for spin-transverse torque magnetic random access memory and for microwave applications. We then briefly discussed about imperfect junctions and the problem associated with design and simulation analysis.

In chapter two, we introduced density functional theory (DFT). We started with two fundamental theorems of DFT and introduced the Kohn-Sham equation for an effective single particle potential for the auxiliary system, which has the same ground state density and total energy as the real system. We then introduced the exchange and correlation functional for slow and high varying density regime of the system. We then introduced the Slater and Kohn-Sham exchange potential and showed that the Slater exchange is $\frac{3}{2}$ larger than the Kohn-Sham exchange. We discuss the atomic self-interaction correction scheme that has been used for correcting the band-gap of semiconductors and insulators. We then briefly discussed about the pseudo-potentials and sufficient conditions for generating good pseudo-potentials for materials.

We then move to chapter three, and discuss about the mathematical formalism of quantum transport. We started with the unperturbed system Green's function and developed a relation between perturbed and unperturbed Green's function under constant external potential V in time domains. We derived the Lippmann-Schwinger equation and using the self-energy we further derived Dyson's equation in the time domains. We then transform the Green's function from time domains into frequency domain and developed a useful relation between retard/advanced Green's function and self-energy. We then write the Green's function in spectral form and derived a relation between generalised and projected density of state. We then write the Green's function for the entire space (left-lead, device region and right lead). We treated the device part as a perturbation and assumed that the perturbation effect will die out in both sides of the device part within a few unit-cells in the leads. We then derived an effective Green's function in terms of the leads and leads-device coupling Green's functions (also called the self-energy of the leads). We then partitioned the full wave-function into left, device-region, and right leads. We then used these partitioned wave-functions and derived the current assuming that in the steady state the charge in the device region will be stationary. Our final current equation look similar to the Landuer-Buttiker coherent quantum transport equation.

We then move to chapter four, for designing and analysing a general magnetic tunnel junction. We discussed the tunnelling magneto-resistance model and theory for amorphous and crystalline barriers. We discussed the Julliere model for amorphous barriers, Landauer-Buttiker theory and a simple potential barrier tunnelling model for crystalline insulators. We discussed the transverse curvature effect of the wave-function in coherent tunnelling current. We then classified the symmetries of the Bloch states after projecting them on-to the $\mathrm{x-y}$ plane (assuming transport is along the z-axis). We then discussed the Bloch wave-function amplitude decay plot analysis in $2d(k_x, k_y)$ for transport supporting points in the first Brillouin zone. Then we discussed the complex-band analysis at the traverse supporting points for symmetries of the Bloch states that will be filtered at these points. After that, we discussed the selection of the ferromagnetic electrodes which can supply the required symmetries of the Bloch state along the transport direction. We then discussed about the design of the magnetic tunnel junctions and a proper commensurate interface with right atoms from both sides faces to each other using the Gibbs formation energy of the possible components that can form between the ferromagnet and insulating materials. We then discussed the band off-set calculation of the junction using macroscopic average energy rule to make sure that the junction is an insulator. Junction insulation is the necessary condition for a tunnelling based MTJ. We then discussed the relaxation of MTJ interfaces and what possible steps can be taken in order to reduce the relaxation time. Then we discussed about the Siesta-Smeagol set-up for quantum tunnelling transport.

We then move to chapter five, and discussed about the HfO_2, and SiO_2 wide band-gap insulators as potential candidates for future tunnel barriers in MTJs. We chose *bcc*-Fe, *cubic*-HfO_2, *hcp*-Co, and *α-quartz*-SiO_2 for the Fe|HfO_2|Fe and Co|SiO_2|Co based MTJs. For commensurate interfaces between Fe/HfO_2, we compressed the Fe lattice parameter by 2.4%, and extended HfO_2 lattice parameter by 11%. We then performed more Siesta calculations for the HfO_2 with different lattice parameters to confirm that HfO_2 still maintains its bulk electronic properties, namely, its band-gap. We found that the HfO_2 LDA band-gap is ~ 3.9 eV, which is very much same as the bulk unconstrained lattice parameter band-gap. We then ensured the commensurate interfaces by allowing oxygen atoms from HfO_2 to face the Fe atoms from the iron ferromagnet, because the Gibbs formation energy of iron-oxides (FeO/Fe_2O_3) are more negative than the binary compounds between Fe and Hf. In $Co|SiO_2|Co$ junction, we compressed the *hcp*-Co lattice parameter by 2.2%, and put no strain on the SiO_2, because we found that the SiO_2 is very sensitive to the strain and junction relaxation will take a much longer time than in the normal cases. At the interfaces between Co/SiO_2, we allow oxygen atoms from the SiO_2 to face the Co atoms from the ferromagnet, because the Gibbs formation energy of the Co-oxides are more negative than the binary compounds forms between Co and Si. We then performed $2d(k_x, k_y)$ Bloch wave-function amplitude decay plot for the transport supporting point in the first Brillouin zone. We then did complex-band analysis at the transport supporting points for the symmetries filtering of the Bloch state which are filtered at these points. In the case of HfO_2, we have found that the HfO_2 supports the Γ-point driven transport and filters the Δ_1 symmetry of the Bloch states in the [001] transport direction (see in table 7.2). *bcc*-Fe supplies spin-up Δ_1 and spin-up and spin-down Δ_5 symmetries of the Bloch states along the transport direction [001] (see in table 7.1). In a HfO_2 based MTJ, we have found a fairly good TMR within the LDA formalism, which can be further improved after correcting the band-gap.

In the case of SiO_2, we have found that SiO_2 also supports Γ-point driven transport and filters the $\Delta_2^{'}$ symmetry of the Bloch states in the [001] transport direction (see in table 7.2). Unfortunately *hcp* cobalt supplies both spin up and spin down $\Delta_2^{'}$ Bloch states in the transport direction (see in table 7.1). Therefore, the TMR turns out low in SiO_2-based MTJs.

We then move to chapter six, and discussed the possibilities of the display materials (ZnO, GaN, and AlN) as a tunnelling barriers for future MTJs. In the case of ZnO we have found that it changes its crystal structure from wurzite into a graphite-like planar form once incorporated into a junction. In this form ZnO supports the Γ-point driven transport and filters the Δ_1 symmetry of the Bloch states at the Γ-point, while the transport is along the [001] direction (see in table 7.2). We have performed band offset calculations between Fe(Co) and ZnO and found that the Fe(Co)|ZnO|Fe(Co) junction is metallic (see in table 7.2). This metallic character has also been confirmed by the high transmission. *bcc*-Fe and *bcc*-Co both supply spin-up and spin-down symmetries of the Bloch states at the Γ-point along the transport direction [111](see in table 7.1). Consequently the TMR for ZnO-based MTJs turns out to be low ($\sim 45-69\%$).

In the GaN case, the material filters the Δ_1 symmetry of the Bloch states at the Γ, K and M-points in the first Brillouin zone (see in table 7.2). We have performed a band offset calculation for the Fe(Co)|GaN|Fe(Co) junction and found that the junction common Fermi energy level is very close to the GaN conduction band. This feature has also been confirmed by the transmission analysis. *bcc*-Fe and *bcc*-Co both supply spin-up and spin-down symmetries of the Bloch states at the Γ-point along the transport direction (see in table 7.1). Whereas at the K-point *bcc*-Co supplies spin-down $\Delta_{2'}$, and *bcc*-Fe supplies both spin-up and spin-down $\Delta_{2'}$ symmetries of the Bloch states. At the M-point *bcc*-Co supplies both spin-up and spin-down Δ_1 symmetries of the Bloch states, whereas *bcc*-Fe supplies both spin-up and spin-down $\Delta_{2'}$ symmetries of the Bloch states. Due to either mismatch between symmetries (symmetry filtering by the insulator and symmetry supplying by the ferromagnet at the transport supporting points along the transport direction, e.g. K-point in GaN case) or due to the inability of the ferromagnet electrodes to supply the only one spin channel Bloch state with required symmetry (Δ_1 in GaN case) at the transport supporting points (e.g. Γ, and M-points) along the transport direction the TMR in a GaN based MTJs turns out to be low ($\sim 29-30\%$).

In the AlN case, the filtering concerns the Δ_1 symmetry of the Bloch states at the Γ, K and M-points in the first Brillouin zone (see in table 7.2). We have computed the band offset for the Fe(Co)|AlN|Fe(Co) junction and found that the junction behaves as a perfect insulator (see in table 7.2). *bcc*-Fe and *bcc*-Co both supply spin-up and spin-down symmetries of the Bloch states at the Γ-point along the transport direction (see in table 7.1). Whereas at the K-point *bcc*-Co supplies spin-down $\Delta_{2'}$, and *bcc*-Fe supplies both spin-up and spin-down $\Delta_{2'}$ symmetries of the Bloch states. At the M-point *bcc*-Co supplies both spin-up and spin-down Δ_1 symmetries of the Bloch states, whereas *bcc*-Fe supplies both spin-up and spin-down $\Delta_{2'}$ symmetries of the Bloch states. Due to either mismatch between symmetries (symmetry filtering by the insulator and symmetry supplying by the ferromagnet at the transport supporting points, e.g. K-point in AlN case)at or due to the inability of the ferromagnet electrodes to supply the only one spin channel Bloch state with required symmetry (Δ_1 in AlN case) at the transport supporting points (e.g. Γ, and M-points) along the transport direction the TMR in a AlN-based MTJs remains low ($\sim 20 - 47\%$).

Our findings suggests that the display materials, ZnO, GaN, and AlN may be promising candidates for spintronics, however proper ferromagnetic electrodes are required. These need to supply the required symmetries of the Bloch states in the transport direction in order to produce high TMR. The search for new ferromagnets, which can supply the required symmetry of the Bloch state in the display materials or others wide band-gap insulators in the transport direction may open a new gateway for spintronics in the near future.

Ferromagnet	**Transport direction**	**Symmetry of the Bloch states available along the transport direction**
bcc-Fe	$\Gamma - \mathrm{Z}$	$\Delta_{1\uparrow},\ \Delta_{5\uparrow},\ \Delta_{5\downarrow}$
hcp-Co	$\Gamma - \mathrm{Z}$	$\Delta_{2'\uparrow},\ \Delta_{2'\downarrow}$
bcc-Co	$\Gamma - \mathrm{P}$	$\Delta_{1\uparrow},\ \Delta_{1\downarrow}$
bcc-Fe	$\Gamma - \mathrm{P}$	$\Delta_{1\uparrow},\ \Delta_{1\downarrow}$
bcc-Co	$\mathrm{K} - \mathrm{H}$	$\Delta_{2'\downarrow}$
bcc-Fe	$\mathrm{K} - \mathrm{H}$	$\Delta_{2'\uparrow},\ \Delta_{2'\downarrow}$
bcc-Co	$\mathrm{M} - \mathrm{L}$	$\Delta_{1\uparrow},\ \Delta_{1\downarrow}$
bcc-Fe	$\mathrm{M} - \mathrm{L}$	$\Delta_{2'\uparrow},\ \Delta_{2'\downarrow}$

Table 7.1: *bcc*-Fe supplies both spin-up and spin-down Δ_5 and only spin-up Δ_1 symmetries of the Bloch states along the transport direction [001]. *hcp*-Co supplies both spin-up and spin-down $\Delta_{2'}$ symmetry of Bloch state along the transport direction [001]. *bcc*-Fe and *bcc*-Co both supply spin-up and spin-down Δ_1 symmetry of the Bloch state along $\Gamma - \mathrm{P}$ direction. *bcc*-Co supplies spin-down $\Delta_{2'}$ symmetry of the Bloch state along $\mathrm{K} - \mathrm{H}$ direction, whereas *bcc*-Fe supplies both spin-up and spin-down $\Delta_{2'}$ symmetry of the Bloch states. *bcc*-Co supplies both spin-up and spin-down Δ_1 symmetry of the Bloch state along $\mathrm{M} - \mathrm{L}$ direction, whereas *bcc*-Fe supplies both spin-up and spin-down $\Delta_{2'}$ symmetry of the Bloch state along the same direction.

Junction	**Junction-state**	**Transport supporting point**	**Symmetry filter of the Bloch state at the transport supporting point**	**TMR %**
Fe|HfO$_2$|Fe	perfect-insulator	Γ	Δ_1	~ 3500
Co|SiO$_2$|Co	perfect-insulator	Γ	$\Delta_{2'}$	~ 250
Co|ZnO|Co	metallic	Γ	Δ_1	~ 45
Fe|ZnO|Fe	metallic	Γ	Δ_1	~ 69.2
Co|GaN|Co	insulator	Γ, K, M	Δ_1, Δ_1, Δ_1	~ 30
Fe|GaN|Fe	insulator	Γ, K, M	Δ_1, Δ_1, Δ_1	~ 29
Co|AlN|Co	perfect-insulator	Γ, K, M	Δ_1, Δ_1, Δ_1	~ 47
Fe|AlN|Fe	perfect-insulator	Γ, K, M	Δ_1, Δ_1, Δ_1	~ 20.4

Table 7.2: Transmission in HfO$_2$ is mostly Γ-point driven of the first Brillouin zone, and filters the Δ_1 symmetry of the Bloch state at the Γ-point. The TMR in HfO$_2$ based magnetic tunnel-junction with *bcc*-Fe as a ferromagnetic electrode is $\sim 3500\%$. Transmission in SiO$_2$ is mostly Γ-point driven of the first Brillouin zone, and filters $\Delta_{2'}$ symmetry of the Bloch state at the Γ-point. The TMR in SiO$_2$ based magnetic tunnel-junction with *hcp*-Co as a ferromagnetic electrode is $\sim 250\%$. A ZnO based magnetic tunnel junction is metallic. Transmission in ZnO is mostly Γ-point driven and the Δ_1 symmetry of Bloch state get filters at the Γ-point. The TMR in ZnO based magnetic tunnel-junctions with *bcc*-Co and *bcc*-Fe as ferromagnetic electrode is $\sim 45 - 69\%$. A GaN based magnetic tunnel junction is insulator. The common Fermi energy of the junction is very close (0.84 eV) to the conduction band minimum of GaN. Transmission in GaN is mostly driven by Γ, K and M-points, and the Δ_1 symmetry of the Bloch states is filtered at these points. The TMR of a GaN based magnetic tunnel-junction with *bcc*-Fe and *bcc*-Co as ferromagnetic electrodes is $\sim 29 - 30\%$. An AlN based magnetic tunnel junction is perfect-insulator and the common Fermi energy of the junction is in the middle of the band-gap of AlN. Transmission in AlN is mostly driven by Γ, K and M-points, and it filters Δ_1 symmetry of Bloch states. The TMR in AlN based magnetic tunnel-junctions with *bcc*-Fe and *bcc*-Co as ferromagnetic electrodes is $\sim 20 - 47\%$.

Chapter 8

Publications

[1] Gokaran Shukla, T. Archer ,S. Sanvito “HfO_2 and SiO_2 as barriers in magnetic tunelling junctions” link.aps.org/pdf/10.1103/PhysRevB.95.184410.

[2] Gokaran Shukla, T. Archer, S. Sanvito “ZnO, AlN and GaN as a Tunnel Barriers in MTJs for Read Head Application in Hard Drive Industries” (in preparation).

Bibliography

[1] W. H. Butler and A. Gupta, "Magnetic memory: A signal boost is in order ," *Nat. Mater.*, vol. 3, no. 12, pp. 845–847, 2004.

[2] W. H. Butler, "Tunneling magnetoresistance from a symmetry filtering effect," *Science and Technology of Advanced Materials*, vol. 9, no. 1, p. 14106, 2008.

[3] W. H. Butler, X.-G. Zhang, T. C. Schulthess, and J. M. MacLaren, "Spin-dependent tunneling conductance of Fe/MgO/Fe sandwiches," *Physical Review B*, vol. 63, no. 5, p. 054416, 2001.

[4] S. Yuasa, T. Nagahama, A. Fukushima, Y. Suzuki, and K. Ando, "Giant room-temperature magnetoresistance in single-crystal Fe/MgO/Fe magnetic tunnel junctions," *Nature Materials*, vol. 3, no. 12, pp. 868–871, 2004.

[5] A. de Melo Souza, *Molecular Electronics: First Principles and Model Approaches.* PhD thesis, Trinity College Dublin Ireland, 2015.

[6] M. N. Baibich, J. M. Broto, A. Fert, F. N. Van Dau, F. Petroff, P. Eitenne, G. Creuzet, A. Friederich, and J. Chazelas, "Giant magnetoresistance of (001)Fe/(001)Cr magnetic superlattices," *Physical Review Letters*, vol. 61, no. 21, pp. 2472–2475, 1988.

[7] G. Binasch, P. Grünberg, F. Saurenbach, and W. Zinn, "Enhanced magnetoresistance in layered magnetic structures with antiferromagnetic interlayer exchange," *Physical Review B*, vol. 39, no. 7, pp. 4828–4830, 1989.

[8] N. F. Mott, “Electrons in transition metals,” *Advances in Physics*, vol. 13, no. 51, pp. 325–422, 1964.

[9] J. Bass and W. P. P. Jr, “Spin-diffusion lengths in metals and alloys , and spin-flipping at metal / metal interfaces : an experimentalist ’ s critical review ,” *J.Phys.Condens.Matter*, vol. 19, no. 18, p. 183201, 2007.

[10] G. Magnetoresistances, “Perpendicular Giant Magnetoresistances of Ag/Co Multilayers,” *Physical Review letters*, vol. 66, no. 23, pp. 3060–3063, 1991.

[11] M. Julliere, “Tunneling between ferromagnetic films,” *Physics Letters A*, vol. 54, no. 3, pp. 225–226, 1975.

[12] I. I. Mazin, “How to Define and Calculate the Degree of Spin Polarization in Ferromagnets,” *Physical Review Letters*, vol. 83, no. 7, pp. 1427–1430, 1999.

[13] J. S. Moodera, L. R. Kinder, T. M. Wong, and R. Meservey, “Large magnetoresistance at room temperature in ferromagnetic thin film tunnel junctions,” *Physical Review Letters*, vol. 74, no. 16, pp. 3273–3276, 1995.

[14] T. Miyazaki and N. Tezuka, “Giant magnetic tunneling effect in Fe/Al_2O_3/Fe junction,” *Journal of Magnetism and Magnetic Materials*, vol. 139, no. 3, pp. 94–97, 1995.

[15] J. Mathon and A. Umerski, “Theory of tunneling magnetoresistance of an epitaxial Fe/MgO/Fe(001) junction,” *Physical Review B*, vol. 63, no. 22, p. 220403, 2001.

[16] S. S. P. Parkin, C. Kaiser, A. Panchula, P. M. Rice, B. Hughes, M. Samant, and S.-H. Yang, “Giant tunnelling magnetoresistance at room temperature with MgO (100) tunnel barriers,” *Nature Materials*, vol. 3, no. 12, pp. 862–867, 2004.

[17] I. Z. Evgeny .Y. Tsymbal, *Handbook of Spin Transport and Magnetsim.* Chapman and hall/CRC, 2011.

[18] D. F. N. V. Claude Chappert, Albert Fert, “The emergence of spin electronics in data storage,” *Nature Materials*, vol. 6, no. 11, pp. 813–823, 2007.

[19] K. Gilmore and M. D. Stiles, “Anisotropic damping of the magnetization dynamics in Ni , Co , and Fe,” *Physical Review B*, vol. 81, no. 17, p. 174414, 2010.

[20] S. Miwa, “Highly sensitive nanoscale spin-torque diode,” *Nature Materials*, vol. 13, no. 1, pp. 50–56, 2014.

[21] A. M. Deac, A. Fukushima, H. Kubota, H. Maehara, Y. Suzuki, S. Yuasa, Y. Nagamine, K. Tsunekawa, D. D. Djayaprawira, and N. Watanabe, “Bias-driven high-power microwave emission from MgO-based tunnel magnetoresistance devices,” *Nature Physics*, vol. 4, no. 10, pp. 803–809, 2008.

[22] A. Janotti and C. G. Van de Walle, “Fundamentals of zinc oxide as a semiconductor,” *Rep Prog Phy*, vol. 72, no. 12, p. 126501, 2009.

[23] S. Strite and H. Morko, “GaN, AlN, and InN: A review,” *Journal of Vacuum Science & Technology B: Microelectronics and Nanometer Structures Processing, Measurement, and Phenomena*, vol. 10, no. 4, pp. 1237–1266, 1992.

[24] P. Hohenberg and W. Kohn, “Inhomogeneous Electron Gas,” *Phys. Rev.*, vol. 136, no. 3B, pp. B864—-B871, 1964.

[25] W. Kohn and L. J. Sham, “Self-consistent equations including exchange and correlation effects,” *Physical Review*, vol. 140, no. 4A, p. A1133, 1965.

[26] E.Fermi and E.Amaldi. *Accad. Ital.Rome*, vol. 6, p. 119, 1934.

[27] J. P. Perdew and A. Zunger, “Self-interaction correction to density-functional approximations for many-electron systems,” *Physical Review B*, vol. 23, no. 10, pp. 5048–5079, 1981.

[28] A. Zunger, “Spin-dependent correlated atomic pseudopotentials,” *Physical Review*, vol. 22, no. 2, p. 649, 1980.

[29] M.M.Rieger and P.Vogl, “Self-interaction corrections in semiconductors,” *Physical Review B*, vol. 52, no. 23, pp. 16567–16574, 1995.

[30] D. Vogel, P. Kruger, and J. Pollmann, “Self-interaction and relaxation-corrected pseudopotentials for II-VI semiconductors,” *Physical Review B*, vol. 54, no. 8, pp. 5495–5511, 1995.

[31] A. Filippetti and N. Spaldin, “A self-interaction corrected pseudopotential scheme for magnetic and strongly-correlated systems,” *Physical Review B*, vol. 67, no. 12, p. 18, 2003.

[32] C. D. Pemmaraju, T. Archer, D. Sánchez-Portal, and S. Sanvito, “Atomic-orbital-based approximate self-interaction correction scheme for molecules and solids,” *Physical Review B - Condensed Matter and Materials Physics*, vol. 75, no. 4, pp. 1–16, 2007.

[33] A. Filippetti, C. D. Pemmaraju, S. Sanvito, P. Delugas, D. Puggioni, and V. Fiorentini, “Variational pseudo-self-interaction-corrected density functional approach to the ab initio description of correlated solids and molecules,” *Physical Review B - Condensed Matter and Materials Physics*, vol. 84, no. 19, p. 195127, 2011.

[34] D. Hamann, M. Schlüter, and C. Chiang, “Norm-Conserving Pseudopotentials,” *Physical Review Letters*, vol. 43, no. 20, pp. 1494–1497, 1979.

[35] G. B. Bachelet, D. R. Hamann, and M. , “Pseudopotentials that work: From h to pu,” *Phys. Rev. B*, vol. 26, no. 8, pp. 4199–4228, 1982.

[36] D. Vanderbilt, “Soft self-consistent pseudopotentials in a generalized eigenvalue formalism,” *Physical Review B*, vol. 41, no. 11, pp. 7892–7895, 1990.

[37] D. G. Hopper, “Ab initio multiple root optimization MCSCF study of the $C_{\infty v}/C_s$ excitation spectra and potential energy surfaces of N_2O,” *The Journal of Chemical Physics*, vol. 80, no. 9, pp. 4290–4316, 1984.

[38] G. P. Kerker, “Non-singular atomic pseudopotentials for solid state applications,” *Journal of Physics C: Solid State Physics*, vol. 13, no. 9, pp. L189–L194, 1980.

[39] N. Troullier and J. L. Martins, “Efficient pseudopotentials for plane-wave calculations. II. Operators for fast iterative diagonalization,” *Physical Review B*, vol. 43, no. 11, pp. 8861–8869, 1991.

[40] R. Landauer, “Spatial variation of currents and fields due to localized scatterers in metallic conduction,” *IBM Journal of Research and Development*, vol. 1, no. 3, pp. 223–231, 1957.

[41] M. Buttiker, “Four-terminal phase-coherent conductance,” *Physical Review Letters*, vol. 57, no. 14, pp. 1761–1764, 1986.

[42] M. Buttiker, “Symmetry of electrical conduction,” *IBM Journal of Research and Development*, vol. 32, no. 3, pp. 317–334, 1988.

[43] E.N.Economou, *Green’s functions in quantum physics.* Springer, Crete, 3rd edition: Springer, Crete, 3rd edition, 2005.

[44] J. De Teresa, a. Barthélémy, a. Fert, J. Contour, R. Lyonnet, F. Montaigne, P. Seneor, and a. Vaurès, “Inverse Tunnel Magnetoresistance in $Co/SrTiO_3/La_{0.7}Sr_{0.3}Mn_{0.3}$: New Ideas on Spin-Polarized Tunneling,” *Physical Review Letters*, vol. 82, no. 21, pp. 4288–4291, 1999.

[45] N. M. Caffrey, T. Archer, I. Rungger, and S. Sanvito, “Coexistance of giant tunneling electroresistance and magnetoresistance in an all-oxide composite magnetic tunnel junction,” *Physical Review Letters*, vol. 109, no. 22, pp. 1–5, 2012.

[46] N. Jutong, I. Rungger, C. Schuster, U. Eckern, S. Sanvito, and U. Schwingenschlgl, “Electronic transport through EuO spin-filter tunnel junctions,” *Physical Review B - Condensed Matter and Materials Physics*, vol. 86, no. 20, pp. 1–10, 2012.

[47] S. V. Faleev, S. S. P. Parkin, and O. N. Mryasov, “Brillouin zone spin filtering mechanism of enhanced tunneling magnetoresistance and correlation effects in a Co(0001)/h-BN/Co(0001) magnetic tunnel junction Brilliouin zone spin filtering mechanism of ....Faleev, Parkin, and Mryasov,” *Physical Review B - Condensed Matter and Materials Physics*, vol. 92, no. 23, pp. 1–7, 2015.

[48] H. X. Liu, Y. Honda, T. Taira, K. I. Matsuda, M. Arita, T. Uemura, and M. Yamamoto, “Giant tunneling magnetoresistance in epitaxial $Co_2MnSi/MgO/Co_2MnSi$ magnetic tunnel junctions by half-metallicity of Co_2MnSi and coherent tunneling,” *Applied Physics Letters*, vol. 101, no. 13, p. 132418, 2012.

[49] S. M. Bhagat and P. Lubitz, “Temperature variation of ferromagnetic relaxation in the 3d transition metals,” *Physical Review B*, vol. 10, no. 1, pp. 179–185, 1974.

[50] J. M. Soler, E. Artacho, J. D. Gale, A. Garcia, J. Junquera, P. Ordejon, and D. Sanchez-Portal, “The SIESTA method for ab initio order-N materials simulation,” *Journal of physics. Condensed matter :*, vol. 14, no. 11, p. 2745, 2002.

[51] D. M. Ceperley and B. J. Alder, “Ground state of the electron gas by a stochastic model,” *Phys. Rev. Lett.*, vol. 45, no. 7, pp. 566–569, 1980.

[52] D. Bagayoko and J. Callaway, “Lattice-parameter dependence of ferromagnetism in bcc and fcc iron,” *Physical Review B*, vol. 28, no. 10, pp. 5419–5422, 1983.

[53] E. A. Owen and D. M. Jones, “Effect of Grain Size on the Crystal Structure of Cobalt,” *Proceedings of the Physical Society. Section B*, vol. 67, no. 6, pp. 456–466, 1954.

[54] C. Sevik and C. Bulutay, “Theoretical study of the insulating oxides and nitrides: SiO_2, GeO_2, Al_2O_3, Si_3N_4, and Ge_3N_4,” *Journal of Materials Science*, vol. 42, no. 16, pp. 6555–6565, 2007.

[55] G. H. Chen, Z. F. Hou, and X. G. Gong, “Structural and electronic properties of cubic HfO_2 surfaces,” *Computational Materials Science*, vol. 44, no. 1, pp. 46–52, 2008.

[56] A. R. Rocha, V. M. García-suárez, S. W. Bailey, C. J. Lambert, J. Ferrer, and S. Sanvito, “Towards molecular spintronics,” *Nature Materials*, vol. 4, no. 4, pp. 335–339, 2005.

[57] A. R. Rocha, V. M. García-Suárez, S. Bailey, C. Lambert, J. Ferrer, and S. Sanvito, “Spin and molecular electronics in atomically generated orbital landscapes,” *Physical Review B - Condensed Matter and Materials Physics*, vol. 73, no. 8, p. 085414, 2006.

[58] I. Rungger and S. Sanvito, “Algorithm for the construction of self-energies for electronic transport calculations based on singularity elimination and singular value decomposition,” *Physical Review B - Condensed Matter and Materials Physics*, vol. 78, no. 3, pp. 1–13, 2008.

[59] I. Yakovkin and P. Dowben, “The problem of the band gap in LDA calculations,” *Surface Review and Letters*, vol. 14, no. 03, pp. 481–487, 2007.

[60] H. Jiang, R. I. Gomez-Abal, P. Rinke, and M. Scheffler, “Electronic band structure of zirconia and hafnia polymorphs from the GW perspective,” *Physical Review B - Condensed Matter and Materials Physics*, vol. 81, no. 8, pp. 1–9, 2010.

[61] A. M. Souza, I. Rungger, U. Schwingenschlögl, and S. Sanvito, “The image charge effect and vibron-assisted processes in Coulomb blockade transport: a first principles approach,” *Nanoscale*, vol. 7, no. 45, pp. 19231–19240, 2015.

[62] F. Sacconi, J. M. Jancu, M. Povolotskyi, and A. Di Carlo, “Full-band tunneling in high-κ oxide MOS structures,” *IEEE Transactions on Electron Devices*, vol. 54, no. 12, pp. 3168–3176, 2007.

[63] J. Bandyopadhyay and K. Gupta, “Low temperature lattice parameter of nickel and some nickel-cobalt alloys and grneisen parameter of nickel,” *Cryogenics*, vol. 17, no. 6, pp. 345 – 347, 1977.

[64] A. Y. Liu and D. J. Singh, “Elastic instability of bcc cobalt,” *Physical Review B*, vol. 47, no. 14, pp. 8515–8519, 1993.

[65] C. W. Bunn and B. Y. C. W. Bunn, “The lattice-dimensions of zinc oxide,” *Proceedings of the Physical Society*, vol. 47, no. 5, pp. 835–842, 2002.

[66] V. Darakchieva, B. Monemar, and A. Usui, “On the lattice parameters of GaN,” *Applied Physics Letters*, vol. 91, no. 3, pp. 1–4, 2007.

[67] F. Litimein, B. Bouhafs, Z. Dridi, and P. Ruterana, “The electronic structure of wurtzite and zincblende AlN: An ab initio comparative study,” *New Journal of Physics*, vol. 4, no. 64, pp. 1–12, 2002.

[68] T. Hanada, “Basic Properties of ZnO, GaN, and Related Materials,” *Oxide and Nitride Semiconductors*, pp. 1–19, 2009.

[69] S. E. Yao T; Hong, *Oxide and Nitride Semiconductors Processing, Properties and Applications.* ISBN: 978-3-540-88846-8, 2009.

[70] X. D. Zhang, M. L. Guo, W. X. Li, and C. L. Liu, “First-principles study of electronic and optical properties in wurtzite $Zn_{1-x}Cd_xO$,” *Journal of Applied Physics*, vol. 103, no. 6, p. 63721, 2008.